MULTI-BEAM INTERFERENCE: THREE-DIMENSIONAL BICONTINUOUS PERIODIC STRUCTURES

A Dissertation
Presented to
The Academic Faculty

by

Shruthi Kumara Vadivel

In Partial Fulfillment
of the Requirements for the Degree
Master of Science in Electrical and Computer Engineering

Georgia Institute of Technology
May 2017

MULTI-BEAM INTERFERENCE: THREE-DIMENSIONAL BICONTINUOUS PERIODIC STRUCTURES

Approved by:

Dr. Thomas K. Gaylord, Advisor
School of Electrical and Computer Engineering
Georgia Institute of Technology

Dr. Shyh-Chiang Shen
School of Electrical and Computer Engineering
Georgia Institute of Technology

Dr. Gee-Kung Chang
School of Electrical and Computer Engineering
Georgia Institute of Technology

Date Approved: April 14, 2017

To my wonderful family and friends

ACKNOWLEDGEMENTS

First and foremost, I would like to thank my thesis advisor, Professor Thomas K. Gaylord for the countless opportunities to learn, and improve. I am honored to have worked under his able guidance. His constant encouragement and drive for perfection have always helped me move forward. He is a truly inspiring individual, both in his personal and professional life. I am certain that the knowledge I gained from him through this experience will help me for a lifetime.

I would also like to thank my thesis committee members, Professor Gee-Kung Chang, Professor Shyh-Chiang Shen and Dr. Justin L. Stay for their invaluable inputs and for taking the time out of their busy schedules to participate.

I am extremely grateful to my fellow Optics Laboratory members for their contributions and support. In particular, I would like to thank Dr. Matthieu Leibovici, for not just helping me get started, but even afterwards, through his excellent work. He is a wonderful mentor and an inspiration. I would also like to thank Yijun Bao, Congshan Wan and Nazli Goller, for helping me prepare for numerous presentations, reviewing manuscripts, the informative Friday lunches, and the Pi-mile races.

I would like to thank Hang Chen, Tran-Vinh D. Nguyen and Gary Spinner from the Institute for Electronics and Nanotechnology for their guidance with the experimental processes. I would also like to thank Eric Woods and Todd Walters from the Materials Characterization Facility for their help with the SEM imaging.

A big shout-out to all my friends, in the US and back home in India, for the endless laughs and support. Thank you for the right kind of encouragements at the right time, it

really helped me go on. You guys have always been a significant part of my life and I could not have done this on my own easily. I would also like to thank my Haiti group. I always learn something when I meet you guys, thank you for helping me see the world from different angles.

Finally, I would like to thank my family for being there through everything that has led to this point. Most importantly, thank you Amma, Appa and Devi-Chitthi, for being my unwavering pillars of strength. Thank you for supporting me and believing in me, and for never once asking me why. You give me the fortitude to be myself. To my family in the US, thank you for making me feel so loved and special, you are my home away from home. Thank you!

TABLE OF CONTENTS

LIST OF TABLES

LIST OF FIGURES

LIST OF SYMBOLS AND ABBREVIATIONS

1D	One-Dimensional
2D	Two-Dimensional
3D	Three-Dimensional
AFM	Atomic Force Microscopy
BARC	Bottom Anti-Reflective Coating
BCC	Body-Centered Cubic
BET	Brunauer, Emmett, Teller
BiC	Bicontinuous
BiM	Bimaterial
CL	Condenser Lens
COL	Compound Objective Lens
CVD	Chemical Vapor Deposition
DC	Diamond Cubic
EL	Expander Lens
FCC	Face-Centered Cubic
FDTD	Finite Difference Time Domain
GT	Georgia Institute of Technology
GUI	Graphical User Interface
HWP	Half-wave plate
MBI	Multi-Beam Interference
MBIL	Multi-Beam Interference Lithography
MOA	Multiple-Optical Axis
NA	Numerical Aperture

OL1	Objective Lens 1
OL2	Objective Lens 2
OPC	Optical Proximity Correction
OPD	Optical Path Difference
PBSC	Polarization Beam Splitter Cube
PhC	Photonic Crystal
PIIES	Pattern-Integrated Interference Exposure System
PIIL	Pattern-Integrated Interference Lithography
RMS	Root-Mean Square
SC	Simple Cubic
SEM	Scanning Electron Microscope
TEA	Triethylamine
TEM	Transmission Electron Microscope
e_{area}	Relative pillar-area error
e_{disp}	Relative pillar-displacement error
$\mathbf{E}_i^{ill}$	2×1 complex electric field vector of the ith beam illuminating the photomask (V/m)
$\mathbf{M}_F^{3\times5}$	Film function matrix
$\mathbf{M}_P^{5\times2}$	Electric field correction matrix
$\hat{\boldsymbol{e}}_{\boldsymbol{i}}$	Polarization vectors of ith interfering beam
$\Lambda_{xy}^{(3+1)}$	Periodicity in the xy-plane for (3+1)-beam configuration (μm)
$\Lambda_{xy}^{(4+1)}$	Periodicity in the xy-plane for (4+1)-beam configuration (μm)
$\Lambda_{z}^{(3+1)}$	Periodicity along the z-axis for (3+1)-beam configuration (μm)
$\Lambda_{z}^{(4+1)}$	Periodicity along the z-axis for (3+1)-beam configuration (μm)

ϕ_i	Initial phase of the beam (*rad*)
a, **b**, **c**	Lattice vector directions
a_c	Edge length of cubic unit cell
a_h, b_h, c_h	Edge lengths of unit cell in hexagonal axes
a_i	Coefficients of the ith fringe Zernike polynomial
A_nB_m	Materials A and B interconnected in n and m dimensions respectively
a_r	Edge length of rhombohedral unit cell
a_r	Edge length of rhombohedral unit cell
C	Energy conservation factor transfer function
c_0	Homogeneity factor (W/V^2)
d	Distance from the center of mass of the estimated pillar and its expected location in the lattice (μm)
d_{beam}	Lateral beam displacement from the optical axis (*mm*)
$\boldsymbol{E}_i$	3x1 complex electric field vector of ith interfering beam (*V/m*)
f_{EL}	Focal length of expander lens (*mm*)
f_{OL1}	Focal length of objective lens 1 (*mm*)
f_{OL2}	Focal length of objective lens 2 (*mm*)
I	Optical intensity distribution of a MBIL exposure (W/m^2)
I_{PIIL}	Optical intensity distribution of a PIIL exposure (W/m^2)
I_{th}	Normalized intensity threshold
$\mathbf{k}_i$	Wavevector of the ith interfering beam (nm^{-1})
M	Compound objective lens magnification
M1 to M8	Mirrors in the PIIL exposure system
nPR	Refractive index of the photoresist
O	Fourier transform of the photomask object (m^{-2})

P	Pupil function
$\boldsymbol{r}$	Position vector in Cartesian coordinates (m)
S	Off-axis beam propagation transfer function
SA	Normalized surface area
V_A, V_B	Volume fraction of materials A and B
W	Normalized wavefront phase error
z_0	Distance from the image focal plane to the photoresist film surface (μm)
Z_i	i^{th} fringe Zernike polynomial
α, β, γ	Angles between the bc, ca and ab axes
θ_{beam}	Angle between the central beam and side beams (deg)
λ_{des}	Lens design wavelength (nm)
λ_{exp}	Exposure wavelength (nm)
τ	Binary pixel values (0 or 1) of the reference pillar

SUMMARY

Bicontinuous microstructures are an important subset of three-dimensional periodic-lattice-based microstructures. Bicontinuity occurs when the constituent materials are interconnected in all three dimensions throughout the structure. Bicontinuous structures have been employed for tissue regrowth, high capacity electrodes, drug delivery, etc., Multi-Beam Interference Lithography (MBIL) has been shown to be a rapid and efficient way to fabricate these structures. However, the detailed characterization of the resulting structures in terms of their bicontinuity is still lacking. The research in this thesis aims at quantifying the bicontinuity range and the associated volumes and surface areas of certain MBIL-produced structures, thereby enabling the identification and fabrication of promising prototype structures.

CHAPTER 1. INTRODUCTION

Any naturally occurring or human-made material can be broadly classified into periodic or non-periodic structures. Of which, periodic structures have gained widespread attention due to their numerous applications.

1.1 Periodic Microstructures

Periodic microstructures are a repetitive arrangement of materials at the microscale. This arrangement can occur in one- (1D), two- (2D) or three-dimensions (3D). This framework enables the systematic design and characterization of periodic structures. These structures offer several advantages in being capable of controlling material properties as well as electromagnetic wave propagation in these materials. The applications of periodic structures are numerous and greatly depend on their lattice structure [1].

The ability of periodic microstructures to manipulate and control light has resulted in their extensive use as photonic devices. Photonic crystals (PhC) are periodic arrangements of dielectric materials that use the difference in refractive indices of the constituent materials to attain a photonic bandgap that alters the propagation of light through it. They have been implemented as lasers [2, 3], resonators [4-6], waveguides [7-11], waveguide couplers [12], multiplexers [13], switches [5, 14-16], antennas [17], sensors [18, 19], filters [20, 21], fibers [22, 23], fiber lasers [24, 25] etc. Quantum information processing devices also utilize PhCs to isolate and transmit qubits [26, 27]. Several microwave applications have also been put forward for PhCs [28, 29].

In bioengineering, significant importance is given to periodic microstructures in areas like particle sensing [30-32], cell culturing [33, 34] and drug delivery [35, 36] as a result of the improved sensitivity and adhesion capabilities. Fluorescence microscopy is enhanced by the use of PhCs for imaging live cells [37]. Microfluidic systems based on periodic structures provide mechanisms for cell analysis [38, 39] and fluid mixing [40]. It has been shown that the magnetic component of light can also be studied using periodic microstructures [41]. In addition to these, periodic structures also find applications in plasmonic, phononic and magnetic devices [1]. Some examples of applications described above are depicted in Figure 1.1.

1.2 Bicontinuous Structures

An important physical property that 3D-periodic structures, comprised of two materials, might possess is called bicontinuity. A structure can be termed as bicontinuous (BiC) if both the constituent materials are completely connected throughout the periodic structure [42]. The structure for example, can be a solid-void or solid-solid combination, provided every volume of the solid/void is linked with every other volume of the same solid/void. Ultimately, the interconnection forms two distinct regions or phases such that, it is possible to trace a route from a point on one material to every other point of the same material through its entire 3D space.

The property of bicontinuity offers several advantages to 3D-periodic structures by enhancing mechanical stability, electrical conductivity and mass transport. As a result, BiC materials find numerous applications in bioengineering, microfluidics, energy storage, etc., BiC structures can be used as nanoporous metals for regulating catalytic activity.

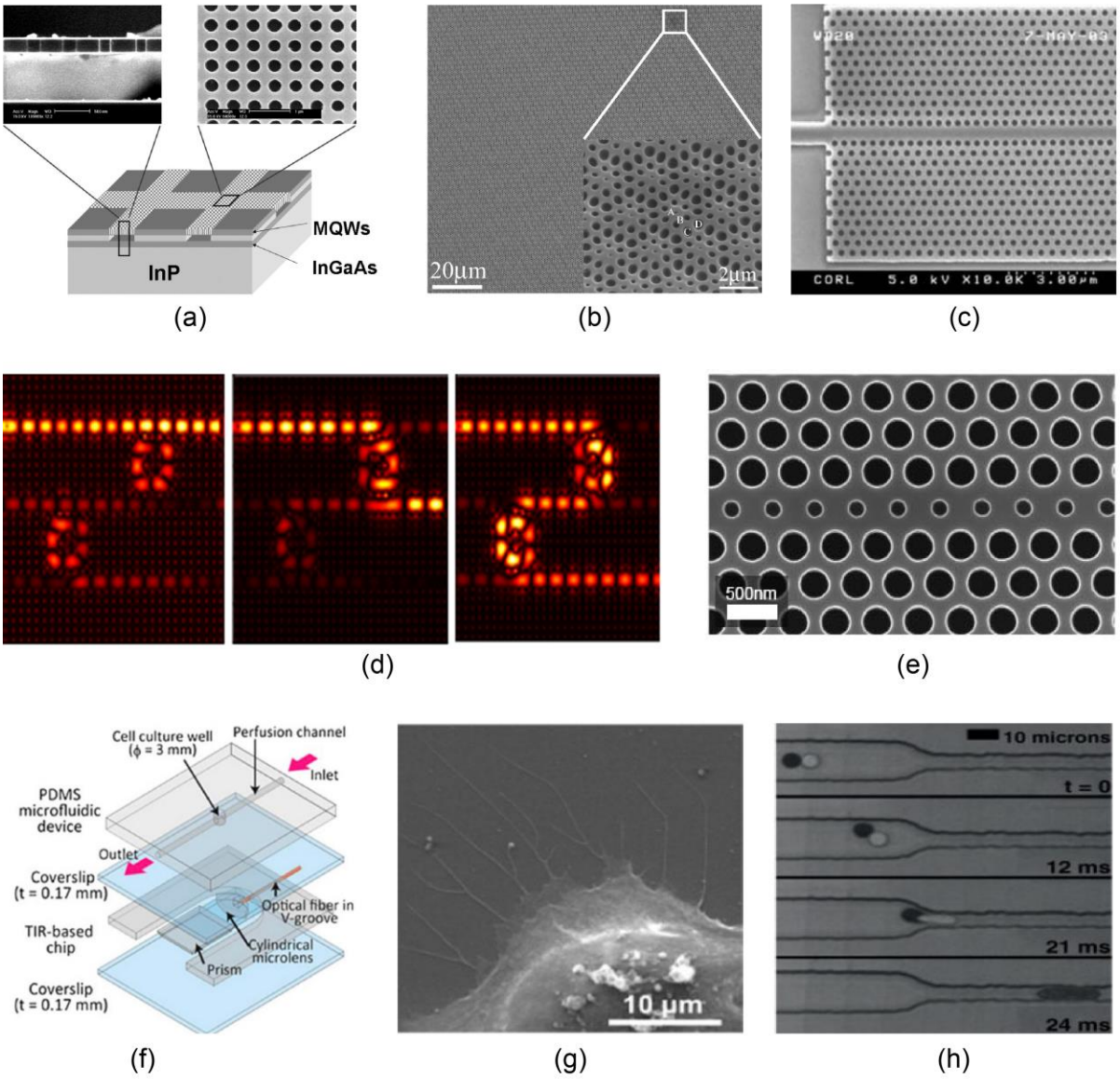

Figure 1.1 – Example applications of periodic microstructures. (a) A square-lattice PhC band edge laser [2]. (b) 2D resonator array showing differing types of air holes in the inset [4]. (c) Conventional straight waveguide integrated with a ridge waveguide [7]. (d) Electric field patterns on a three-output port channel-drop filter [20]. (e) Modified PhC waveguide sensor with increased sensitivity for the detection of proteins [30]. (f) Schematic of an on-chip microfluidic cell culture device [38]. (g) Proliferation of human stem cells on porous silicon scaffolds [33]. (h) Coalescence of two droplets in a microfluidic channel [40].

The nano-scale pores provide high surface area-to-volume ratio that enhances oxide reduction, whereas the BiC framework facilitates the transport of materials [43]. High

energy density lithium-ion cells employ the use of a BiC porous nickel scaffold as electrodes with silicon deposited on it. During lithiation, the silicon swells in the pores causing discontinuities in some parts of the scaffold and the BiC network is necessary to maintain the electrical conductivity [44]. BiC microemulsions are formulated for drug delivery [45, 46] and tissue regeneration [47]. They act as spatial cell scaffolds to grow muscle tissue. The cultured cells grow in multiple layers, dispersed throughout the structure, similar to that of human tissue. Selective isolation of proteins from a highly heterogeneous mixture is carried out through microfluidic devices with a BiC skeleton [48].

BiC structures also find applications as mechanical metamaterials. Owing to their structure, they exhibit unique properties that can be utilized for subwavelength imaging, development of superlenses, electromagnetic cloaking, etc. [1, 49]. They are used to produce high performance protective films as the 3D interlocking enhances load sharing and dissipates energy efficiently [50, 51]. One of the unique properties that metamaterials possess is an anisotropic Poisson's ratio, which is similar to the human bone tissue. Hence, they have been demonstrated as scaffolds for the study and regrowth of the same. Bone tissue regeneration requires a BiC framework for the cells to penetrate deep into the structure [52, 53]. Some of these applications are illustrated in Figure 1.2.

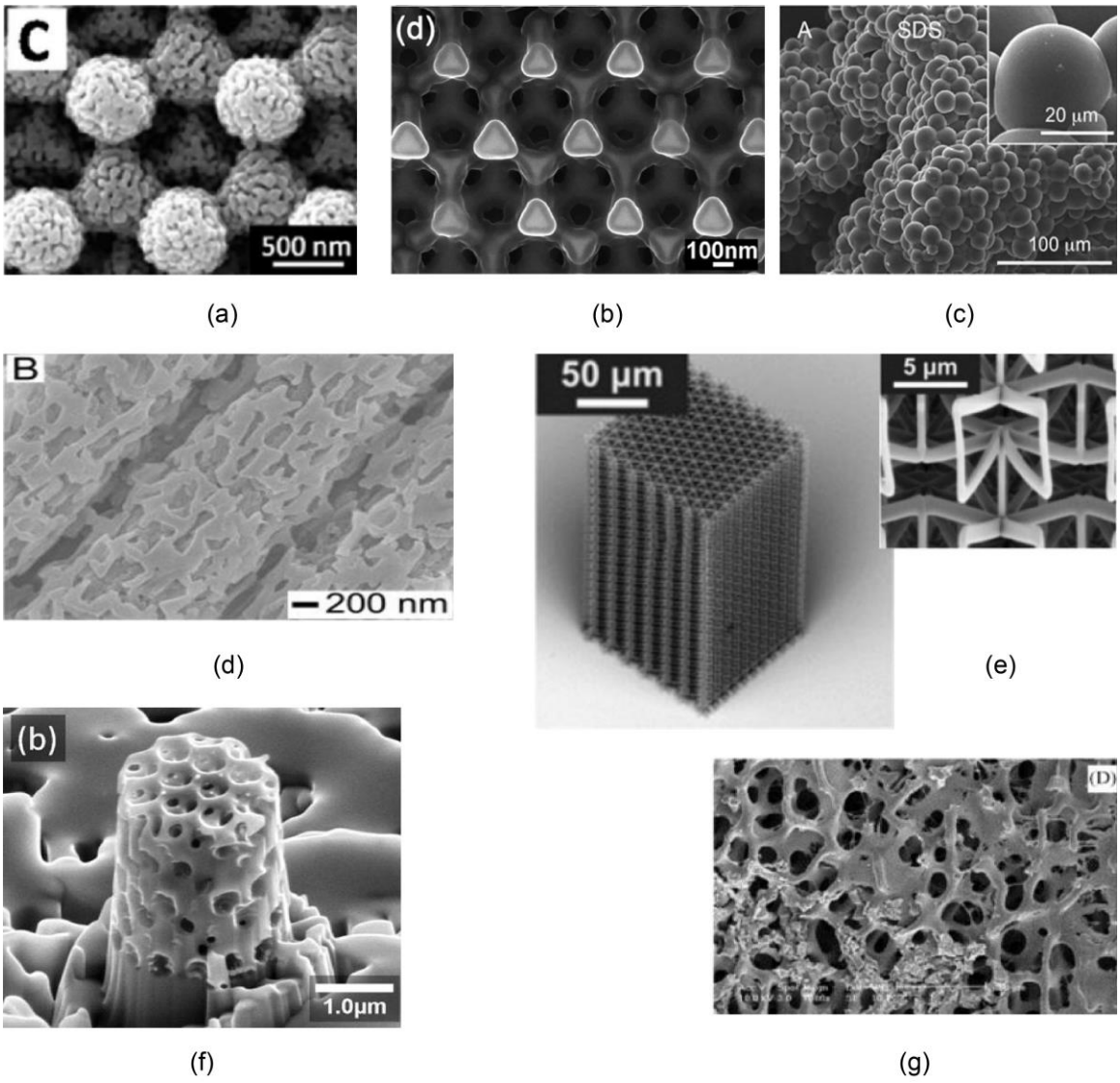

Figure 1.2 – Applications of BiC structures. (a) Porous gold on 3D porous carbon for enhanced catalytic activity [43]. (b) Silicon deposited nickel scaffold as electrodes for lithium-ion cells [44]. (c) 3D cell scaffolds for proliferation of muscle and skin cells [54]. (d) Microfluidic channels on fiber mats for isolation and purification of select proteins [48]. (e) Mechanical metamaterials with negative Poisson's ratio for the study of bone tissue [52]. (f) BiC composites with high specific energy absorption as protective films [50]. (g) Cell culturing of bone cells on a biocompatible BiC calcareous skeleton [55].

1.3 Fabrication of Bicontinuous Structures

Several individual processes exist to develop BiC structures. They can be broadly classified as 1) self-assembly techniques, 2) construction-based techniques, 3) multi-beam interference lithography, and 4) pattern-integrated interference lithography.

1.3.1 Self-Assembly Techniques

This is perhaps the most common method used to fabricate BiC structures. Self-assembly uses thermodynamic forces to combine the constituent materials into stable structures [56]. This method is advantageous in its ability to pattern large area structures and can also be an inexpensive approach depending on the application. Block co-polymer self-assembly can create BiC microstructures utilizing the phase separation between the polymer blocks [45, 51, 57]. Various techniques of phase-inversion, mainly thermally induced phase separation [58] and immersion precipitation [59] have been put forward for the fabrication of microporous membranes as filters. Colloidal self-assembly techniques are used extensively for the development of microemulsions [45, 46], photonic crystals [60] and electrodes [61]. These methods can be used to produce the final structures or can be used as templates on which the required material is deposited by means of nanocasting [62], Chemical Vapor Deposition (CVD) [63], electro-deposition [61], etc. The main drawbacks of self-assembly are associated with the lack of lattice customization and the unintentional defects in the resulting structures. There is very limited flexibility in the geometrical characteristics as colloidal systems usually form the same Face-Centered Cubic (FCC) crystal structure [51]. The complexity and time for the formation of structures

can vary widely depending on the application. Moreover, it requires precise control over the composition and type of materials involved.

1.3.2 Construction-Based Techniques

These techniques involve the writing of structures either layer-by-layer or point-by-point in a serial fashion. Direct-laser writing, which employs a pulsed laser to draw the structure directly on a photosensitive material, can produce even arbitrary structures in 3D [52]. Two-photon lithography is capable of generating high-resolution complex structures by the simultaneous absorption of two photons in a non-linear process [1]. Conventional photolithography can also be used to produce BiC structures, but again only layer-by-layer [64]. All the construction-based methods, although capable of producing customized structures with the required geometry, are extremely time-consuming [51]. This also makes them susceptible to alignment and overlay errors. Hence, they require complex mechanisms to ensure that the various layers are aligned accurately on top of each other. This further increases the manufacturing time, rendering it unsuitable for large-volume production.

1.3.3 Multi-Beam Interference Lithography

Interference Lithography refers to the fabrication of periodic structures by the superposition of non-coplanar electromagnetic waves. Multiple overlapping beams generate an interference pattern with a periodic intensity similar to the periodic function used to represent the structure. This method utilizes the principle that periodic structures can be mathematically described as a sum of Fourier components related to the incident interfering plane waves [1].

In Multi-Beam Interference Lithography (MBIL), the spatial distribution of energy from the overlapping beams is recorded on a substrate coated with a photo-sensitive material or photoresist. The points in the photoresist that are exposed to the beams are chemically altered, and depending on the type of photoresist they either become less soluble or more soluble as compared to the unexposed regions. The substrate is then developed in a solution, leaving the exposed regions intact and unexposed regions dissolved, in the case of a negative-tone photoresist or vice versa in the case of a positive-tone photoresist. This results in a periodic structure whose geometry depends on the beam parameters. The polarizations, amplitudes and wavevectors of the beams, shape the interference pattern and consequently the symmetry of the periodic structure. By controlling the beam configuration, it is possible to produce all 2D [65] and 3D [66] Bravais lattices through MBIL. Three beams interfere to produce 2D structures whereas four or more beams are needed to produce 3D structures as shown in Figure 1.3. "Complex 60-fold 2D quasi-periodic [67], 3D chiral-basis [68], icosahedral [69], spatially variant [70], and dual-lattice interference patterns [71] are furthermore feasible" [72]. Individual beam control can be done by means of phase masks, prisms or polarization beam splitter cubes and wave plates [1]. BiC structures can be formed through MBIL by controlling the dosage of the exposure. The dosage refers to the total amount of energy of the beams received per unit area per unit time by the photoresist. The structures tend to be BiC only for a specific range of exposure doses. Too much or too little exposure can cause the structures to be monocontinuous.

MBIL is a rapid technique that is capable of producing large format defect-free periodic structures. It is capable of manufacturing structures with sub-micron resolution

using exposure times on the order of a few seconds. Being a cost-effective technique, MBIL has found numerous applications in photonics, phononics, bioengineering, microfluidics, smart materials etc. [1]. It can be combined with several other lithographic techniques as a two-step process like electron-beam lithography [73], focused ion beam lithography [74], direct laser writing [75], projection lithography [76], or multi-photon polymerization [77] to produce customized devices with added functionalities. This multi-step procedure is prone to misalignment errors and thereby increases the time and complexity of the process. Alternately, several single-step processes using diffractive masks [78], phase masks [79] and spatial light modulators [70, 80, 81] have also been demonstrated. These techniques however, offer very little lattice-customization and are limited by the resolution of the additional components used.

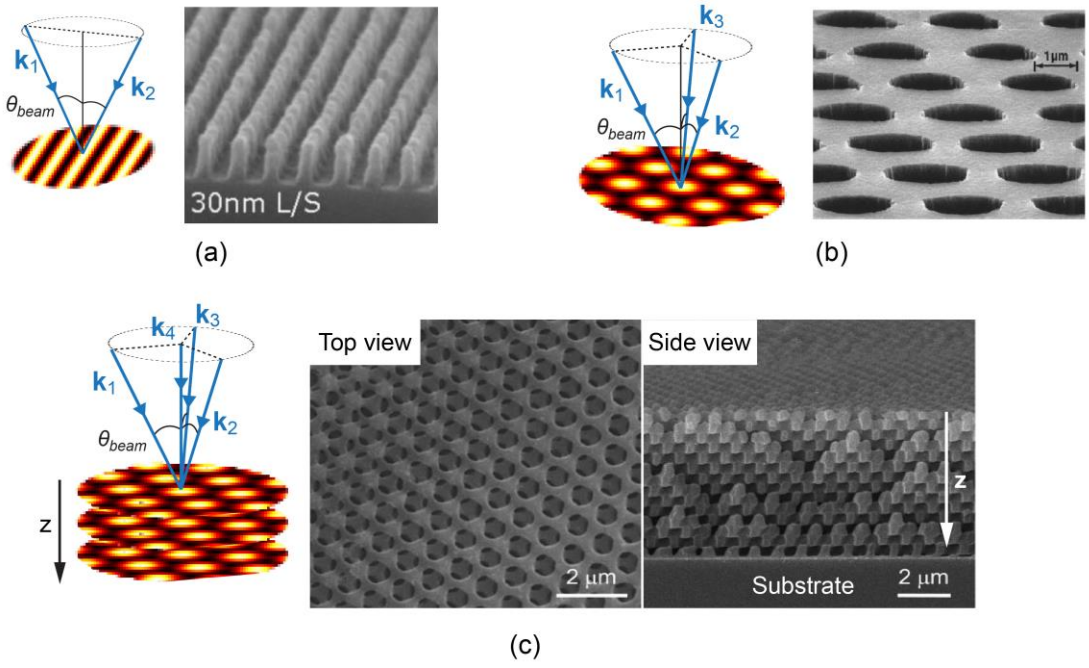

Figure 1.3 – Multi-beam configurations and their corresponding fabricated structures [72]. (a) 1D grating formed by the interference of two beams. (b) 2D pattern formed by the interference of three beams. (c) 3D structure formed by the interference of four beams.

1.3.4 Pattern-Integrated Interference Lithography

The need for a microfabrication technique that is rapid and flexible resulted in the development of Pattern-Integrated Interference Lithography (PIIL) as an extension of MBIL [82]. PIIL combines both interference and imaging in a rapid single-exposure step without the use of additional components [83]. It can produce both 2D and 3D periodic structures with functional elements embedded in them [8, 72, 83, 84]. 3D PIIL was highlighted in a "Spotlight in Optics" article by the Optical Society of America as "*the only method that can both create and pattern 3D periodic structures in a single step*" [85].

1.4 Characterization of Bicontinuous Structures

Various techniques have been used to study and model BiC structures. The characterization of such structures are typically carried out using a combination of simulation/analytical models and imaging. Techniques such as laser scanning confocal microscopy [86] and freeze fracture electron microscopy [87] have been used in conjunction with scattering data to determine if the structure is bicontinuous. Scattering data is collected by techniques like light, small-angle X-ray and small-angle neutron scattering. Analytical models like the Teubner-Strey model [88] and modified Berk theory [89] attempt to simulate the 3D morphology using the obtained scattering data. The specific surface area in [47] was determined using the single-point BET (Brunauer, Emmett, Teller) method, that correlates the surface area of a substance to the amount of physical adsorption of a gas at the surface. The porosity in phase-separated structures are determined by gravimetric analysis [58, 62]. X-ray tomography [57, 60], Scanning Electron Microscope (SEM) [43, 44, 47] imaging and 3D-Transmission Electron

Microscope (TEM) [46] tomography have also been employed to study BiC structures, while the characterization can be done using optical [60, 90, 91], mechanical [52, 92] or electrical [43, 44] means. In elastic mechanics, the stiffness of a structure can be characterized by the elastic wave velocities [49] or nanoindentation [93]. For Multi-Beam Interference (MBI) structures specifically, characterization is carried out using Atomic Force Microscopy (AFM) [94] or SEM imaging [95] along with optical characterization techniques like spectroscopy [96] or reflectivity [97].

1.5 Research Objectives

Although there exists several techniques to characterize the various properties of BiC structures, the exact structural characterization of typical MBI-produced BiC structures is still lacking. The physical attributes regarding the range of bicontinuity; and the volumes and surface areas of the constituent materials in the bicontinuity range have not been investigated. The objective of this thesis is to develop simple models to generate and analyze the bicontinuity of cubic structures through simulations and also to fabricate 3D periodic structures by PIIL.

1.6 Thesis Overview

An outline of the following chapters in this thesis is described below.

In Chapter 2, two representative models for BiC structures are introduced. The conditions for bicontinuity are derived and periodic structures are classified based on the interconnection.

In Chapter 3, the conditions stated in the previous chapter are used to analyze the bicontinuity in cubic structures for both models. The results are depicted for numerous cases.

In Chapter 4, an introduction to the concept of PIIL is given as a technique to fabricate customized 2D and 3D periodic structures. The system configuration and simulation model is reviewed.

In Chapter 5, an improved alignment procedure for the described PIIL system is described along with some experimental results.

In Chapter 6, a summary of the research is presented along with some future research objectives.

In Appendix A and B, MATLAB scripts for the generation of MBI structures and bicontinuity analysis respectively are given.

CHAPTER 2. BICONTINUOUS STRUCTURES

Three-dimensional (3D) periodic lattice-based-microstructures have generated a lot of interest in various fields. In this chapter, 3D periodic structures are classified based on their interconnectedness. Two models for representing periodic structures are described in detail for cubic structures along with the conditions for bicontinuity.

2.1 Types of Interconnectedness

Consider 3D periodic structures made of two materials A and B (a bimaterial structure). For simplification, consider that material B is embedded within material A. Since A and B are interchangeable, there is no loss of generality here and all possible cases are being treated. The 3D periodic structures have non-coplanar lattice vectors **a**, **b** and **c**. The lattice vectors define the planes ab, bc and ca where, ab is the plane of **a** and **b** and so forth. The volume of the parallelepiped is $\mathbf{a}\cdot\mathbf{b}\times\mathbf{c}$. The symbol A_nB_m is defined here to mean that A is interconnected in n dimensions and B is interconnected in m dimensions where n and m can be 0,1,2,3. Based on the nature of their interconnectedness, these bimaterial structures can be classified as described below.

2.1.1 3D-Monocontinuous 3D-Periodic Structures

A_3B_0. Material A is continuous throughout the structure in all three lattice vector directions, **a**, **b** and **c**. Material B occurs as isolated volumes. This case can be seen in Multi-Beam Interference (MBI) structures having a high intensity threshold or equivalently, low exposure dosage. The resulting structures are under exposed and the secondary material is only present in limited maximum intensity regions. This is depicted in Figure 2.1(a).

A_3B_1. Material A is continuous throughout the structure in all three directions. Material B is continuous only in a single lattice vector direction (designated as **a** in Figure 2.1(b)). An example of this type is the self-supporting solid-rod-like structures in air. The solid volumes are continuous in one dimension but are not connected to each other.

A_3B_2. Material A is continuous throughout the structure in all three dimensions. Material B is continuous in two dimensions (**a** and **b**). B is interconnected across the bc and ca planes of the structure shown in Figure 2.1(c). These structures can also be produced by MBI by tailoring the intensity threshold such that it lacks continuity in one dimension. They are typically observed in structures that have an intensity threshold just outside the beginning and end of the bicontinuity range. This will be explained further in the following sections.

2.1.2 3D-Bicontinuous 3D-Periodic Structures

A_3B_3. Both materials A and B are continuous in all three lattice vector directions throughout the structure. This is a bicontinuously interconnected network and all the volumes of both materials are interconnected within each other. This is depicted in Figure 2.1(d).

2.2 Conditions for Bicontinuity

Bicontinuous periodic structures are composed of unit cells repeated periodically in 3D space. Consequently, in order to identify structures as bicontinuous, it is sufficient to define the conditions of bicontinuity for the constituent unit cell. In the following, the unit cell maybe a primitive unit cell, a conventional unit cell or any other unit cell that satisfies 3D periodicity.

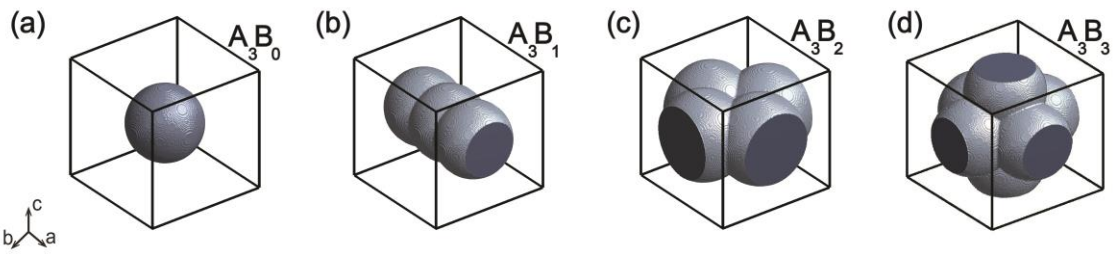

Figure 2.1 – 3D periodic structures based on the type of interconnectedness. 3D-Monocontinuous structures with material B (solid) continuous in 0-(a), 1-(b) and 2-(c) dimensions and Material A (void) continuous in all three dimensions. (d) 3D-Bicontinuous structures with both Materials A and B continuous in all three dimensions.

The primary condition required for bicontinuity is as follows: every volume of both materials A and B must be continuous throughout the unit cell and both materials intersect with the ab, bc and ca faces. The corollaries that result from this condition are as follows. There are both A and B volume paths from any one face of the unit cell to every other face. From symmetry requirements, there will be A and B areas parallel to each other on opposite faces of the unit cells. This establishes continuity between the unit cells which is necessary if the entire structure is bicontinuous. Also, any plane within the unit cell that intersects with four sides of the unit cell must contain both A and B areas. If a plane is found containing only material A or B, then the structure is not bicontinuous. These conditions are employed in the subsequent sections as convenient tests for bicontinuity of cubic unit cells.

2.3 Sphere-at-Each-Lattice-Site Model

To analyze individual unit cells of important rhombohedral and cubic structures, the sphere-at-each-lattice-site model is used. As the name suggests, this model uses ideal spheres of a specified radius at the lattice points of the unit cell. The lattice spheres can be

solid volumes or voids, as they can be used interchangeably. Here we denote the spheres as solid volumes (material B). The simple cubic structure has been shown as an example in Figure 2.2. The unit cell contains spheres at the eight corners of the cell. Each sphere shown here is 1/8th the volume of the entire sphere. The total solid volume occupied by the spheres is (4/3) πr^3.

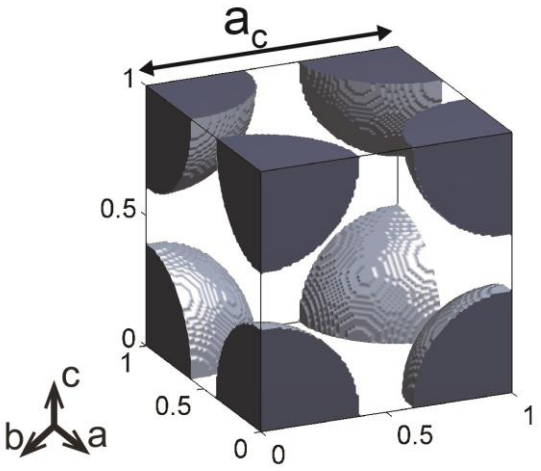

Figure 2.2 – Simple cubic unit cell as an example of a sphere-at-each-lattice-site model. The radius of the spheres shown here is 0.4a_c, where a_c is the length of the edge of the unit cell. The units shown in the figure are length/a_c.

To compare cubic structures to their MBI counterparts, the hexagonal representation of rhombohedral structures is adopted. The length of the edge of the unit cell is denoted as a_h and the height is denoted as c_h. The unit cell is highlighted in red in Figure 2.3. The unit cell is represented in the hexagonal axis as $a_h = b_h \neq c_h$; $\alpha_h = \beta_h = 90°$, $\gamma_h = 120°$. Three unit cells combined (triple cell) gives the entire hexagonal lattice structure. Here, the obverse setting is employed, where the conventional unit cell contains one-eighth of eight corner spheres, and two spheres at (2/3, 1/3, 1/3) and (1/3, 2/3, 2/3) on the body diagonal [98]. Therefore, the total number of spheres in the conventional unit cell is three. This

representative volume is considered for the bicontinuity analysis in the subsequent sections.

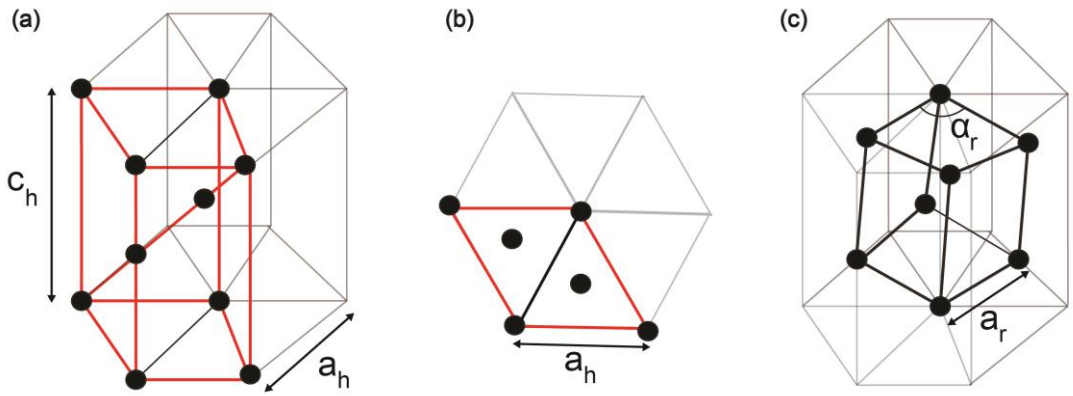

Figure 2.3 – (a) 3D view and (b) top view of the rhombohedral unit cell in the obverse setting, highlighted in red. The gray lines show the hexagonal structure that results from combining three such unit cells. (c) The primitive rhombohedral unit cell.

By varying the ratio of c_h to a_h of the conventional unit cell, it is possible to produce the simple cubic (SC), face-centred cubic (FCC) and body-centred cubic (BCC) structures in this representation. The two central-axis spheres (0, 0, 0) and (0, 0, c_h) together with the body spheres of the triple cell produce a primitive rhombohedral unit cell of side a_r. The rhombohedral unit cell highlighted in Figure 2.3(c) is represented as $a_r = b_r = c_r$; $\alpha_r = \beta_r = \gamma_r \neq 90°$. The rhombohedral angle α_r changes as the c_h to a_h ratio is varied to give the required SC, FCC or BCC limiting case structures as shown in Figure 2.4. The ratios, along with the corresponding rhombohedral angles are given in Table 2.1. The relationship between the hexagonal, rhombohedral and cubic lattice constants are also listed.

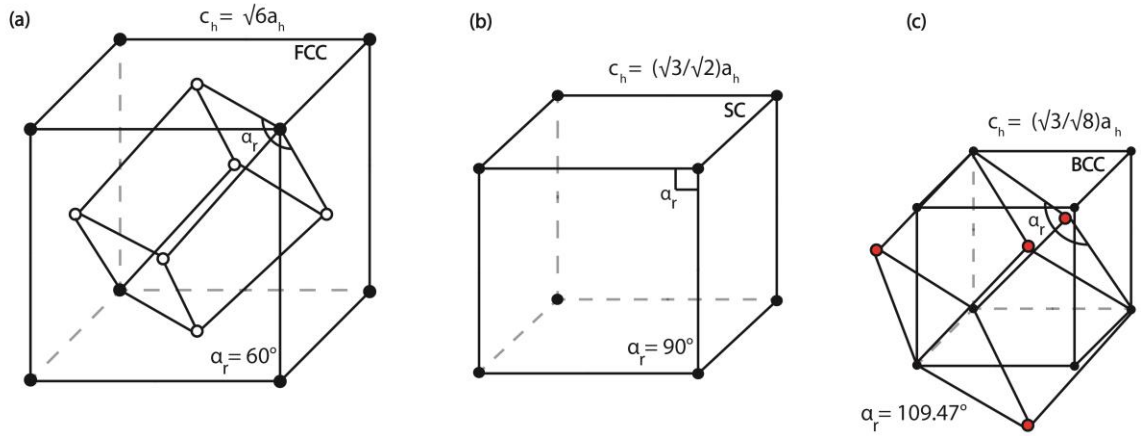

Figure 2.4 – (a) FCC, (b) SC and (b) BCC structures obtained by varying the c_h to a_h ratio. The solid black spheres, hollow discs and red-coloured spheres represent the edge, face-centred and body-centred atoms respectively.

Table 2.1 – The limiting case parameters for cubic structures in the rhombohedral lattice representation

Cubic Structure	c_h / a_h	α_r *(deg)*	Rhombohedral Lattice Constant, a_r	Cubic Lattice Constant, a_c
SC	$\sqrt{6}$	90	$a_h/\sqrt{2}$	$a_h/\sqrt{2}$
FCC	$\sqrt{3}/\sqrt{2}$	60	a_h	$\sqrt{2}\,a_h$
BCC	$\sqrt{3}/\sqrt{8}$	109.47	$\sqrt{3}a_h/\sqrt{8}$	$a_h/\sqrt{2}$

Diamond cubic (DC) lattice is also investigated to facilitate comparison with the woodpile structures formed by MBI. The DC unit cell resembles two FCC unit cells that are displaced from each other by (1/4, 1/4, 1/4) from the origin along the body diagonal. It contains eight spheres, four from each FCC unit cell. The DC unit cell with an edge length of a_c is shown in Figure 2.5. The unit cell is represented as $a_c = b_c = c_c$; $\alpha_c = \beta_c = \gamma_c = 90°$. The lattice constant in this case is the distance between the closest neighbouring points that

occur on the face diagonals of the unit cell as shown in Figure 2.5(b). Thus, the ratio of the height of the unit cell to the edge length is √2 for an ideal DC unit cell.

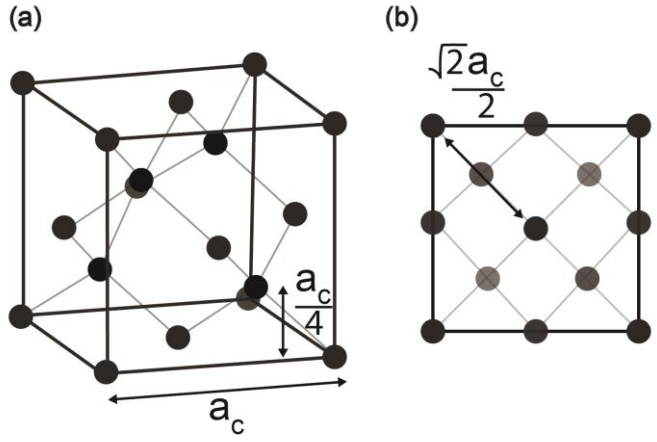

Figure 2.5 – (a) 3D view and (b) top view of DC unit cell of edge length a_c. The lattice constant of the unit cell is depicted in (b).

In order for the structures described in this section to be bicontinuous, the radius of the spheres should be at least large enough to come in contact with each other throughout the structure. Determining the bicontinuity conditions by analysing the unit cells using the sphere-at-each-lattice-site model is described in the next chapter.

2.4 MBI Model

The MBI model simply refers to the structures formed by the superposition of multiple non-coplanar beams. The interference between two beams produce a one-dimensional (1D) pattern whose orientation and period depend on the configuration of the beams. When more than two beams interfere, each beam pair produces a 1D fringe pattern which then are superposed to give the final two-dimensional (2D) or three-dimensional (3D) pattern depending on the number of beams and their associated configuration. The

time-averaged intensity distribution of the pattern formed by the interference of N monochromatic waves can be expressed as [83],

$$I(\boldsymbol{r}) = \sum_{i=1}^{N} \left(\frac{1}{2} \mathrm{Re}[\boldsymbol{E}_i(\boldsymbol{r}) \cdot \boldsymbol{E}_i^*(\boldsymbol{r})] + \sum_{j>i}^{N} \mathrm{Re}\left[\boldsymbol{E}_i(\boldsymbol{r}) \cdot \boldsymbol{E}_j^*(\boldsymbol{r})\right] \right), \tag{2.1}$$

where $\boldsymbol{E}_i(\boldsymbol{r})$ is the 3x1 complex electric field vector created by the i_{th} plane wave at the $\boldsymbol{r}(x, y, z)$ point at the sample plane and Re[] is the real part operator. The electric field can be expressed as,

$$\boldsymbol{E}_i(\boldsymbol{r}) = E_i \exp[-j(\boldsymbol{k}_i \cdot \boldsymbol{r} - \phi_i)] \hat{\boldsymbol{e}}_i \tag{2.2}$$

where $\boldsymbol{k}_i$ is the wavevector, ϕ_i is the initial phase and $\hat{\boldsymbol{e}}_i$ is the polarization vector of the i_{th} interfering beam. In MBI, the required symmetry elements are provided by the parameters of the beam. The space group is determined by the wavevector configuration and the polarization vectors of the non-coplanar beams. The *k*-vector configuration is necessary to obtain translational symmetry while the polarization vectors decide the motif within the unit cell or the rotational symmetry. Even though the periodicity depends on the lattice formed, which in turn is determined from multiple beam parameters, it is always inversely proportional to the side beam at an angle θ_{beam} from the optical axis.

The rhombohedral and woodpile (DC) lattice structures are generated by the (3+1)-beam and (4+1)-beam umbrella configurations. The central beam is circularly polarized while the side beams are linearly polarized and arranged symmetrically around the central beam forming an umbrella-like structure. Then, the angle between the central beam and the side beams, $\theta_{beam,}$ determines the specific point group symmetry formed. The

representative beam configurations and their corresponding unit cells are shown in Figure 2.6. The required polarization vectors of the beams described in Equation (2.2) for both the beam configurations are listed in Table 2.2.

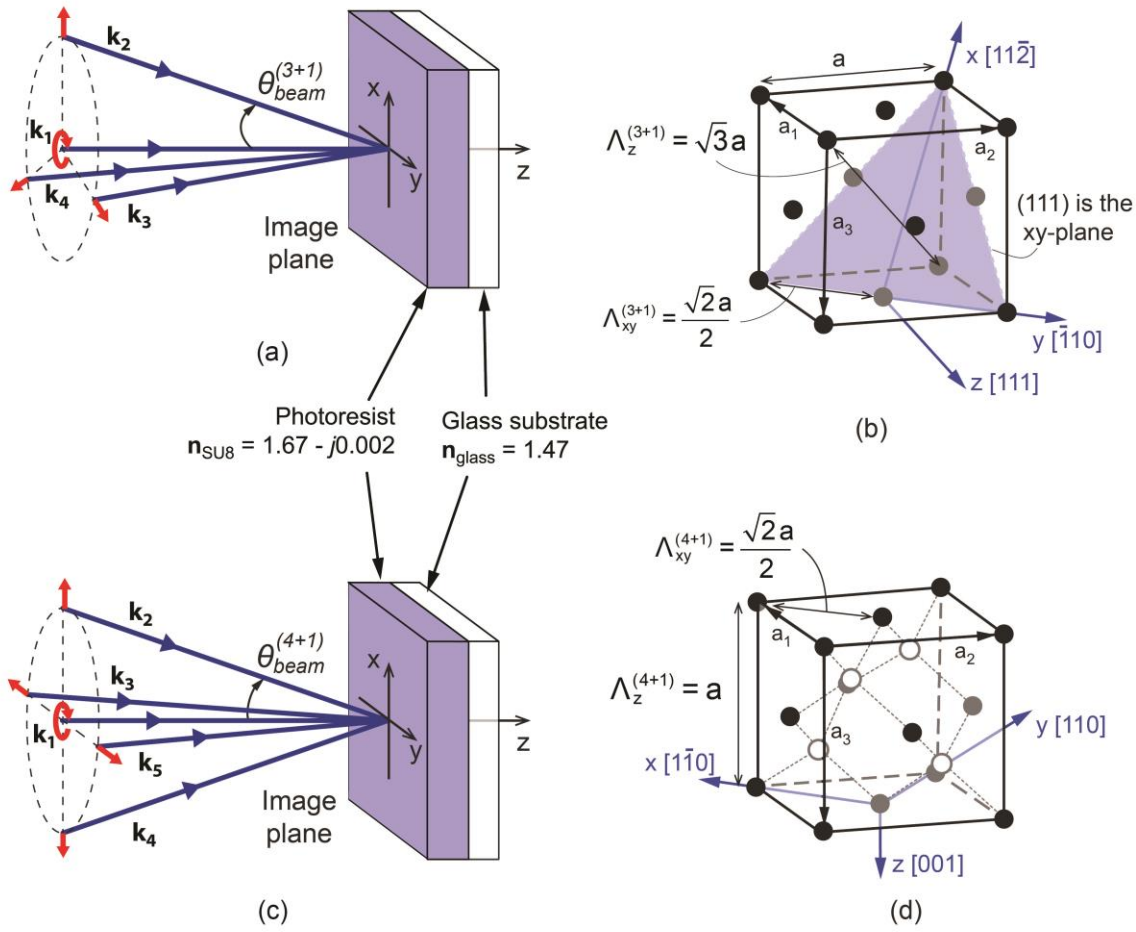

Figure 2.6 – The (a) (3+1)-beam configuration and the (b) corresponding rhombohedral lattice formed. The case depicted here is that of the FCC unit cell. The (4+1)-beam configuration and the (d) corresponding DC structure formed [72].

The specific case of the FCC unit cell is depicted in the (3+1)-beam configuration in Figure 2.6(a) and (b). The beam angle $\theta_{beam}^{(3+1)}$ can be altered to get the desired rhombohedral angle, α_r. The relationship between the two angles is given by [99],

$$\theta_{beam}^{3+1} = cos^{-1}\frac{(1+5\cos\alpha_r)}{3(1+cos\alpha_r)} \tag{2.3}$$

Table 2.2 – Polarization vectors of the beams in the umbrella configuration

	(3+1)-beam Rhombohedral lattice	(4+1)-beam Woodpile lattice
$\widehat{\boldsymbol{e}_1}$	[1/√2 *j*/√2]	[1 *j*]
$\widehat{\boldsymbol{e}_2}$	[0 1]	[1 0]
$\widehat{\boldsymbol{e}_3}$	[√3/2 1/2]	[0 -1]
$\widehat{\boldsymbol{e}_4}$	[√3/2 -1/2]	[-1 0]
$\widehat{\boldsymbol{e}_5}$	N/A	[0 1]

The required wavelength of the beams can be derived from the rhombohedral edge length, a_r and θ_{beam} as,

$$\lambda = a_r(3sin^2\theta_{beam}^{3+1})\sqrt{\frac{(1+\cos\theta_{beam}^{3+1})}{(5-3\cos\theta_{beam}^{3+1})}} \tag{2.4}$$

The rhombohedral edge length a_r, shown in Figure 2.3(c) can, in turn, be calculated from the hexagonal lattice constant parameters a_h and c_h using,

$$a_r = \frac{1}{3}\sqrt{3a_h^2 + c_h^2} \tag{2.5}$$

The rhombohedral angle can also be calculated from the hexagonal parameters by,

$$\alpha_r = 2\sin^{-1}\frac{\left({}^{3}/_{2}\right)}{\sqrt{3+\left({}^{c_h^2}/_{a_h^2}\right)}} \tag{2.6}$$

Alternatively, by knowing the beam parameters, it is possible to calculate the hexagonal lattice parameters directly using [72],

$$a_h = \Lambda_{xy}^{3+1} = \frac{2\lambda}{\sqrt{3}\sin\theta_{beam}^{3+1}} \tag{2.7}$$

and,

$$c_h = \Lambda_z^{3+1} = \frac{\lambda}{2sin^2(\frac{\theta_{beam}^{3+1}}{2})} \tag{2.8}$$

Equation (2.8) gives the period along the *z*-direction for structures formed in air. In photoresist, the periodicity depends on the refractive index of the medium due to the refraction that occurs at the air-photoresist interface. The periodicity remains the same on the *xy*-plane but the structures are elongated in the *z*-direction. The resulting periodicity in a photoresist with a refractive index n_{PR} is given by [72],

$$c_h = \Lambda_z^{3+1} = \frac{\lambda/n_{PR}}{2\sin^2\left(\sin^{-1}(\sin\theta_{beam}^{3+1}/n_{PR})/2\right)} \tag{2.9}$$

The relationship between the beam angle and the rhombohedral angle for structures in air and photoresist given by Equation (4.6) is represented in Figure 2.7. It can be seen that while considering structures formed in photoresist the desired rhombohedral angles cannot be attained. The photoresist modeled here is the negative-tone epoxy photoresist SU-8 with a refractive index $n_{PR} = 1.67$. SU-8 is a well-known i-line (*363.8nm*) photoresist

that is widely used for the fabrication of 3D structures due to its ability to produce high aspect ratio structures [100-104].

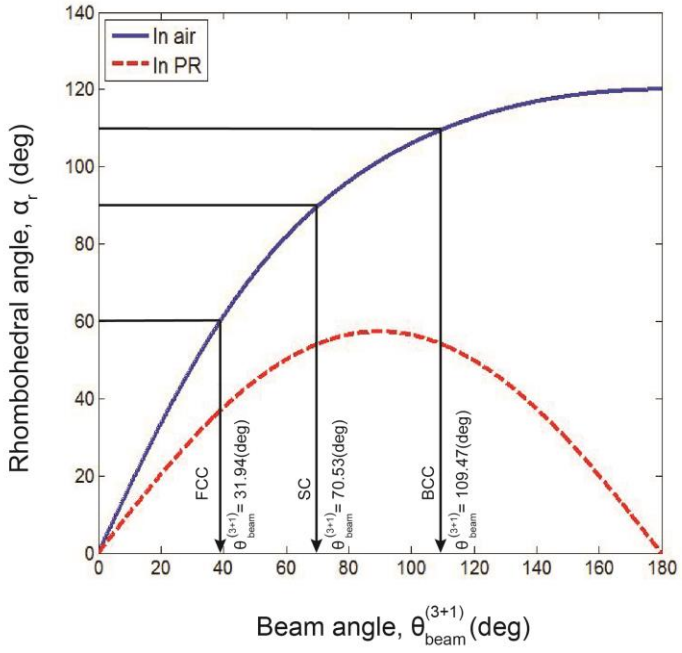

Figure 2.7 – Relationship between the beam angle and rhombohedral angle for structures in air and SU-8 photoresist. The limiting case structures are marked at their corresponding points in the graph.

The refraction changes the beam angle, θ_{beam} such that the ideal case structures cannot be generated without sufficient index-matching [90, 105]. Index-matching is a technique by which the refraction at the air-photoresist interface is averted by using a prism whose refractive index matches that of the photoresist. By employing this technique, the angle of the beam is sufficient to produce the limiting case structures, and the periodicity along the z-direction is once again given by Equation (2.8).

The woodpile lattice is generated using (4+1)-beam configuration, with the central beam circularly polarized and the side beams linearly polarized as shown in Figure 2.6(c).

The resulting DC lattice structure is shown in Figure 2.6(d). The periodicity in the *xy*-plane in this case can be expressed as [72],

$$\Lambda_{xy}^{4+1} = \frac{\lambda}{\sin\theta_{beam}^{4+1}} \tag{2.10}$$

and the periodicity in the *z*-direction is similar to that of the (3+1)-beam case and is given by,

$$\Lambda_{z}^{4+1} = \frac{\lambda}{2sin^2(\frac{\theta_{beam}^{4+1}}{2})} \tag{2.11}$$

in air. While considering structures in photoresist, the refractive index of the medium is once again factored into the equation to give,

$$\Lambda_{z}^{4+1} = \frac{\lambda/n_{PR}}{2\sin^2\left(\sin^{-1}(\sin\theta_{beam}^{4+1}/n_{PR})/2\right)} \tag{2.12}$$

As discussed in the previous section, the ideal case FCC and DC cases occur when the height to edge length ratios for the unit cells are √6 and √2 respectively. In MBI, for both beam configurations, the change in periodicity as a result of refraction alters the ratio between the periodicity in the *z*-direction and the periodicity in the *xy*-direction causing the structures to deviate from their ideal cubic cases. The ratio is plotted as a function of the beam angle, θ_{beam} for the index-matched and unmatched cases in Figure 2.8. The ideal ratio is achieved in the index-matched case when the beam angle equals 38.94° and 70.53°

for the FCC and DC cases respectively. This ratio cannot be achieved in the unmatched case.

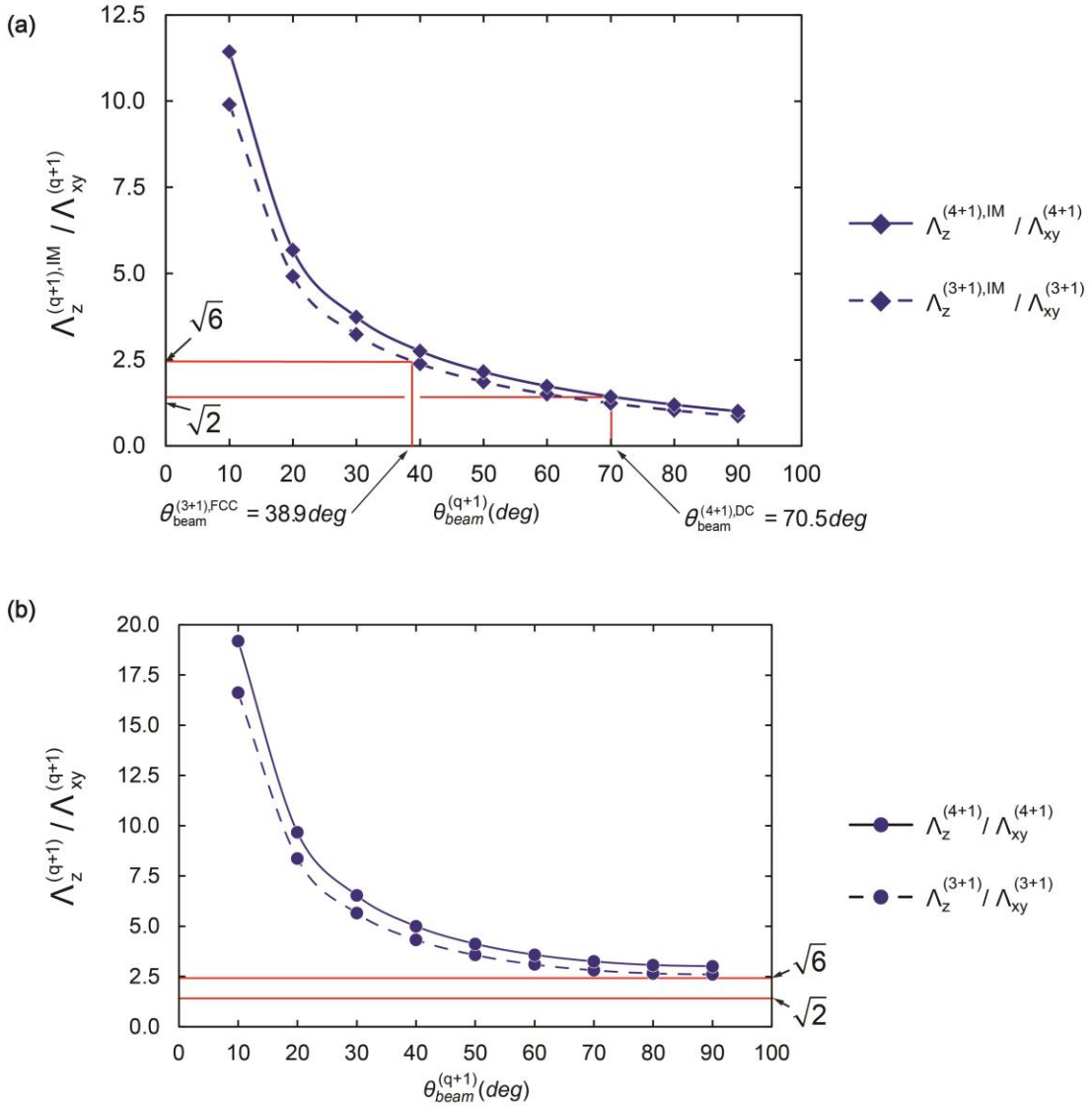

Figure 2.8 – The ratio between the periodicities in the z-direction and xy-direction as a function of the beam angle for the (a) index-matched and (b) unmatched cases for the (3+1)- and (4+1)-beam configurations [72].

The preceding cases discussed in this section assumed a uniform medium at the sample plane with light propagating only in the plane of incidence. This is however not

the case. The photoresist case typically represents an assembly of thin films consisting of a top layer, resist layer and a Bottom Anti-Reflective Coating (BARC) layer on a substrate. Due to high numerical aperture effects, the light passing through a lens is not confined to its plane of incidence. The beams continuously undergo refraction and reflection through the stack, the magnitude of which depends on the polarization of the beam at that point. Therefore, it is necessary to model the photoresist as a stack of thin layers in order to obtain a realistic intensity distribution within the photoresist. Using Flagello's formalism the interference pattern within the photoresist is computed by forming a film function matrix that is multiplied in the frequency domain with the input electric field. This film function matrix is a function of the complex refractive indices of the various layers in the photoresist film. It describes the standing wave effects that occur due to the reflection from the subsequent layer. The forward and backward travelling waves are summed up at each layer of the photoresist to account for the refraction, reflection and absorption effects, for each beam. The inverse Fourier transform of the product yields the final electric field distribution, from which the intensity information is computed [106]. Examples of structures produced by the (3+1)-beam and (4+1)-beam configurations using this model is depicted in Figure 2.9.

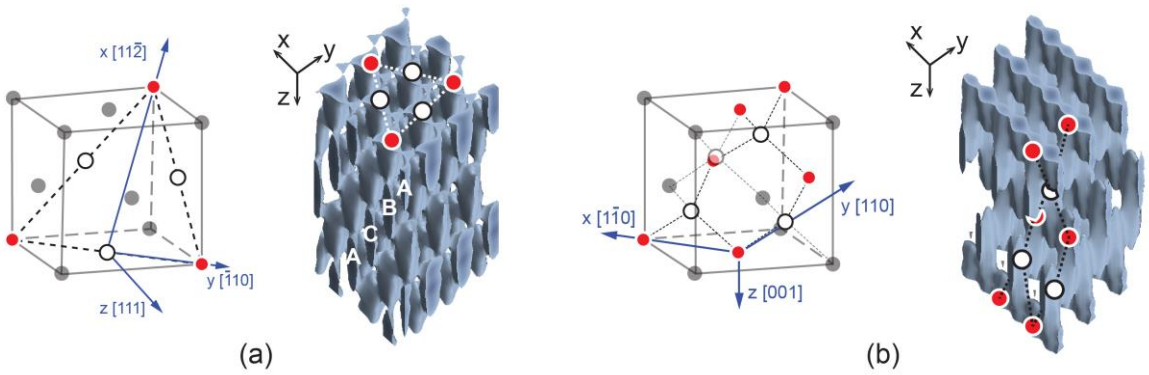

Figure 2.9 – (a) FCC unit cell and the corresponding (3+1)-beam structure. (b) DC unit cell and the corresponding (4+1)-beam structure. Both cases are modeled considering the photoresist as a non-uniform medium leading to standing-wave behavior within the photoresist layers [72].

2.5 Symmetry Elements in MBI structures

As discussed in the previous section, the symmetry elements in the MBI-produced structures are determined by the beam parameters, namely, the wavevector configuration, intensity, and polarization state. For practical applications, it is not sufficient to investigate only the translational symmetry, rather, it is important to determine the structure of the resist inside the unit cell. Thus, the overall symmetry is the maximal point symmetry that is common to both the lattice as well as the motif of the crystal structure [107].

The umbrella configuration typically generates the rhombohedral lattice system which contains 7 space groups that can be represented using hexagonal or rhombohedral axes. General rhombohedral structures possess a maximum of two symmetry elements. When the limiting cubic cases are considered, symmetry conditions are added to it. The $\bar{3}m$ point group corresponds to the rhombohedral lattice formed by the umbrella configuration. The symbol $\bar{3}$ represents a three-fold rotation-inversion axis, which defines the operation for a counter-clockwise rotation of 120° around the axis followed by an

inversion through the point on the axis, and *m* denotes the reflection through a plane containing the axis. The SC, FCC, BCC and DC structures are an extension of the $\bar{3}m$ point group and are represented as $Pm\bar{3}m, Fm\bar{3}m, Im\bar{3}m$ and $Fd\bar{3}m$ respectively in their short symbol notation. The symbols *P*, *F* and *I* stand for primitive, all face-centered and body-centered respectively. The $m\bar{3}m$ point group consists of two unique mirror planes parallel to one three-fold rotation-inversion axis, and can be formed by the (3+1)-beam umbrella configuration. The $d\bar{3}m$ point group signifies a diamond glide plane with a translational component of one-quarter along the diagonal of a face-centered cell in addition to the $\bar{3}m$ symmetry. This point group is generated by the (4+1)-beam umbrella configuration.

The symmetry elements can also be defined in their full symbol notations. The SC, FCC and BCC symmetry elements are $(P4/m\bar{3}2/m), (F4/m\bar{3}2/m)$ and $(I4/m\bar{3}2/m)$ signifying a four-fold rotation axis with a mirror plane perpendicular to it, a three-fold rotation-inversion axis and a two-fold rotation axis with a mirror plane perpendicular to it. The DC cell is represented as $(F4_1/d\bar{3}2/c)$ which signifies a 4-fold right-handed screw axis rotated about 90° with a one-quarter translational vector parallel to the axis and normal to the diamond glide plane, a three-fold rotation-inversion axis and a two-fold rotation axis with a one-half translation axial glide plane perpendicular to it [98].

These symmetry constraints are used as conditions to tailor the coefficients of the plane waves in order to produce the desired lattice geometry, as well as to optimize the contrast in MBI-produced structures [108]. The impact of the symmetry elements on the bicontinuity characteristics of periodic structures will be described in the next chapter.

2.6 Applicability of Bicontinuity Analysis

The analysis of MBI-produced structures as a function of the exposure intensity, put forth in this work can be applied to various lithography models and materials. In traditional photolithography, the regions exposed to a light source in a positive (negative) tone photoresist becomes more soluble (insoluble) compared to the original medium in a developing solvent. The high-contrast photoresists used in conventional photolithography, ideally exhibit a binary response wherein the exposed regions undergo chemical changes only when the intensity values of the pattern are above a certain threshold intensity level. This lithographic threshold of the photoresist depends on the photoresist sensitivity and the processing conditions like the baking temperatures and time, developing time and choice of developer [109]. Alternatively, grayscale photolithography uses photoresists that ideally exhibit low contrasts in order to produce an analog image transfer response to exposure. The partial exposure of a photoresist renders it soluble to a developer in proportion to the exposure dose. As a consequence, after development, the resist exhibits the morphology of a three-dimensional surface. Grayscale lithography can be realized using variable transmission masks, also known as gray-tone masks [110] in X-ray [111] as well as interference lithography [112] based techniques. Variable-dose direct writing technique employs a narrow beam of charged particles or photons through a software mask instead of a physical mask to achieve grayscale response [113]. Evidently, in threshold and continual response systems, or a combination of both [114], the volume fractions of the constituent materials in the final structure is primarily a function of the exposure intensity, and therefore can benefit from the study of the physical characteristics of the structures.

This analysis also applies to photosensitive materials other than conventional photoresists. Photopolymerizable liquid crystals segregate themselves from the polymer they are dispersed in under the influence of exposure giving rise to phase separated polymer-rich and liquid-crystal rich regions with different refractive indices. Orienting the crystals by applying an electric field to maximize the index contrast has resulted in their application as efficient display systems [115, 116]. Photochromic materials that are capable of modulating their absorbance in response to light of a specific wavelength can be used for heterogeneous micropatterning [117] or resolution enhancement [118, 119]. Photorefractive materials find many applications as updateable holographic displays [120], photonic crystals [121] and laser ultrasonic receivers [122]. The refractive index modulation in photorefractive materials occurs due to the periodic space-charge field that is formed as a result of exposure to an interference beam pattern. They also exhibit the phenomenon of optical solitons that can be utilized in photonic switching architectures [123, 124]. As a result, this analysis can be applied to any material that is capable of undergoing a photo-induced change of a physical property, such as the refractive index, absorption, electrical conductivity, density, porosity, cross-linking in polymers, line-breaking in polymers, magnetization, electric polarization, thermal conductivity etc.

For traditional photolithography, where the end result is a structure formed by the combination of hardened acid-resistant photoresist and air, the analysis is applicable only for structures occurring in the bicontinuous range. In the case of a negative-tone photoresist like SU-8, low-intensity threshold responses result in mostly filled, solid structures [91]. The low-intensity regions occur in isolated volumes within the structure but is not capable of being removed during development as there is no path for the solvent

to reach the area, giving rise to non-porous structures [125]. For high-intensity thresholds, the insoluble volume is significantly lesser than the soluble volume and a major portion of the structure is washed away, causing it to collapse during development [126]. Only in the bicontinuous range, the structures are physically realistic as they are completely porous structures within this range. There are possible approaches to producing isolated voids embedded within the volume of the structures. These may involve 3D exposure followed by the diffusion of unexposed materials in case of negative-tone photoresists, and exposed materials in case of positive-tone photoresists, out of the material, thus leaving behind voids. The diffusion in this case may be induced by chemical, thermal or any other means.

2.7 Summary

3D periodic structures can be classified based on their interconnectedness as monocontinuous or bicontinuous structures. In order to possess the property of bicontinuity, specific conditions need to be satisfied by the unit cell. There should exist a path for both materials from one unit cell to every other unit cell throughout the structure in a bicontinuously connected network. The sphere-at-each-lattice-site model and the MBI model were used to represent rhombohedral and diamond cubic structures. The conditions to achieve the limiting case SC, FCC, BCC and DC structures were described in both cases. The MBI model was modified to include the standing wave effects seen within the photoresist. The symmetry elements present in the cubic structures were also discussed as they are used as constraints to determine the beam parameters.

CHAPTER 3. BICONTINUITY ANALYSIS

The conditions derived to determine the existence of bicontinuity are applied to the rhombohedral and woodpile structures using the models described in the previous chapter. The range of bicontinuity is defined and determined for both models, and the parameters that influence this range are identified. The trends in the volumes and surface areas of the representative structures are presented and discussed for various incident polarizations.

3.1 Bicontinuity Characteristics of the Sphere-at-Each-Lattice-Site Model

In this model, spheres are present at each lattice point in the unit cells. These spheres are of an identical radius. As this radius increases, the nature of interconnectedness in the structure changes. Initially, we start with a radius of zero, and the entire structure comprises of material A, which in this case is the void volume. By increasing the radius of the spheres, material B, or the solid volume, begins to appear. Thus, the structure becomes bimaterial as the spheres start to form. With further increase in the radius, the spheres get large enough to come in contact with each other. Until this point, the spheres are distinct and the volume fraction of material B in the unit cell is the volume of the fraction of spheres inside the unit cell i.e., the volume of material B is proportional to the third power of the radius of the spheres. At this mark, the structure enters the bicontinuity range. This point in the radius of the spheres is denoted as the bicontinuous range start radius or simply, the BiC Start Radius. To determine the BiC Start Radius, it is sufficient to consider only a section of the unit cell that from symmetry is representative of the entire unit cell. The section under consideration depends on the geometry of the unit cell. For example in a simple cubic (SC) and face-centered cubic (FCC) unit cell, any one end face

can be analyzed to determine the BiC Start Radius as shown in Figure 3.1(a) and (b). The red outline shows the plane that contains the point of contact. For a body-centered cubic (BCC) and diamond cubic (DC) unit cell, the plane containing the opposite edges is analyzed. The planes and the point of contact are depicted in Figure 3.1(c) and (d) for BCC and DC respectively. It is important to note that, in these cases, the point of first contact between the spheres and the start of the bicontinuous range coincide due to symmetry. This might not be the case while considering structures with lesser symmetry than the ones considered here.

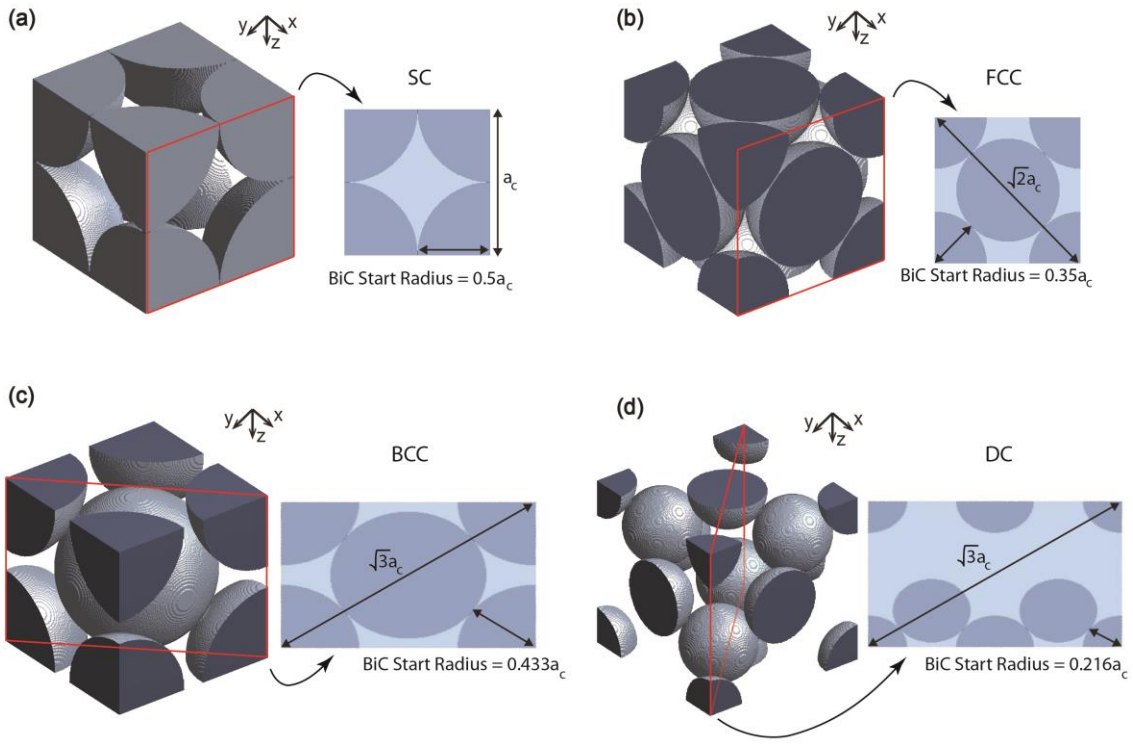

Figure 3.1 – Figures showing the BiC Start Radius for (a) SC, (b) FCC, (c) BCC and (d) DC unit cells. The corresponding insets show the plane depicted by the red outline which is used to compute the BiC Start Radius.

Once the structures enter the bicontinuity range, every solid volume and every void volume is connected to every other solid volume and void volume. The rate of increase in

the volume fraction of the solid material is less than the rate of increase before the start of the bicontinuity range. This decrease in the rate occurs because, after the spheres come into contact, the overlap between the spheres increases, and the increase in radius causes adjacent spheres to add to the same points in space. This state remains until the increase in radius causes a plane to be completely filled with just the solid material. The radius of the spheres at this point is denoted as the bicontinuity range end radius or simply, the BiC End Radius. Once again, these completely filled planes and the corresponding radii can be determined geometrically by analyzing the structure of each unit cell. Similar to determining the BiC Start Radius, the planes depend on the structure of the unit cell. The BiC End Radius for the structures along with examples of completely filled planes are shown in Figure 3.2.

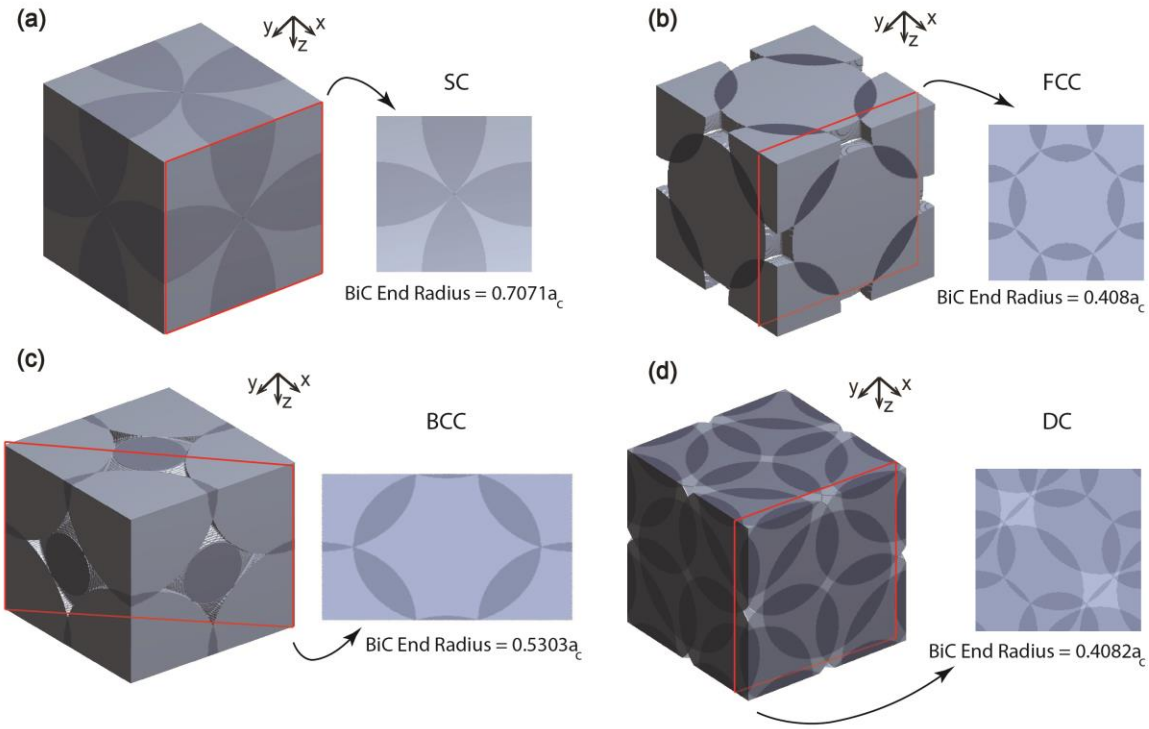

Figure 3.2 – Figures showing the BiC End radius for (a) SC, (b) FCC, (c) BCC and (d) DC unit cells. The corresponding insets show the plane depicted by the red outline which is completely filled with the solid material.

Beyond the BiC End Radius, the structure ceases to be bicontinuous as there is no path for one of the materials, in this case the void, from one face to every other face which is the defining condition for bicontinuity. With further increase in the radius, the structures get completely filled with just one material. The radius of the spheres are large enough to cover the entire structure with the solid volume, and this radius is denoted by the bimaterial end radius, or the BiM End Radius. At this point, the structure ceases to be bimaterial. The BiM End Radius for each cubic structure is depicted in Figure 3.3.

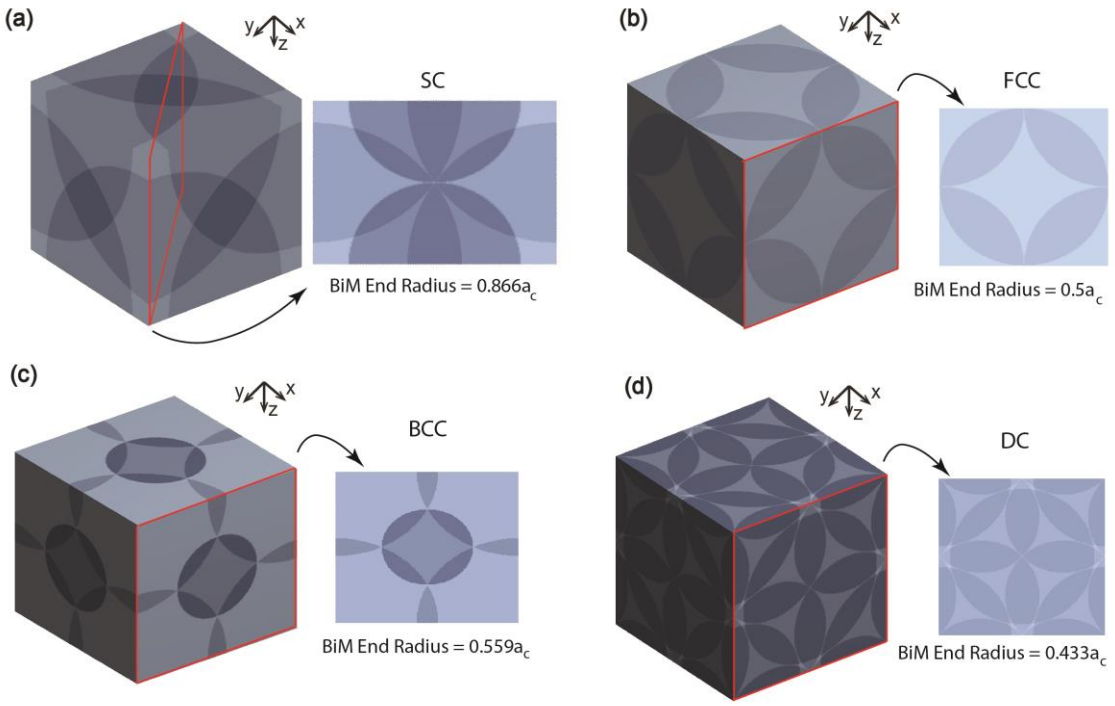

Figure 3.3 – Figures showing the BiM End radius for (a) SC, (b) FCC, (c) BCC and (d) DC unit cells. The corresponding insets show an example plane that is filled last, denoted by the red outline.

For the sphere-at-each-lattice site model, these three points of significance namely, the BiC Start Radius, the BiC End Radius and the BiM End Radius, are used to describe the bicontinuity characteristics. The results are summarized in Table 3.1. The points of interest here are denoted in terms of their corresponding cubic lattice constants a_c.

A similar analysis is carried out for the rhombohedral structures, after applying the limiting conditions to produce the cubic cases as described in the previous chapter. An example of the FCC limiting case is shown in Figure 3.4. The minimum representative volume that is being considered for the bicontinuity analysis is outlined as the rectangular prism in red in Figure 3.4(d). This representative rectangular prism has a volume that is identical to the rhombic prism denoted by the solid black lines in the same figure, which is

Table 3.1 – Bicontinuity parameters for cubic structures using the sphere-at-each-lattice site model

Structure	BiC Start Radius (a_c)	BiC End Radius (a_c)	BiM End Radius (a_c)
SC	1/2	$\sqrt{2}/2$	$\sqrt{3}/2$
FCC	$\sqrt{2}/4$	$\sqrt{6}/6$	1/2
BCC	$\sqrt{3}/4$	$3\sqrt{2}/8$	$\sqrt{5}/4$
DC	$\sqrt{3}/8$	$\sqrt{11}/8$	$\sqrt{3}/4$

the typical representation of the rhombohedral unit cell. Since each face of the rectangular prism is a mirror plane, the contents of the prism can be mirrored about its six faces to generate the entire structure. The rectangular prism is therefore representative of the total structure. The orthogonal edges of the rectangular prism make it a convenient choice for analyzing the component volumes, interface areas, and the bicontinuous properties of the entire structure.

The volume trend of material B as a function of the normalized sphere radius is shown in Figure 3.4(e) along with the equation that relates the cubic and rhombohedral structures for the FCC case. The regions of interest are highlighted. The graph shows the trends described earlier that were observed in the cubic cases. The range before the start of the bicontinuity range showing a cubic increase in the volume fraction, followed by the decrease in the rate of increase of the volume fraction in the bicontinuity range and finally the saturation of the curve to a completely filled structure (volume equals unity) after the end of the bimaterial range. The corresponding points of interest are depicted in the graph

along with figures showing the unit cell at these points. The insets in Figure 3.4(a)-(d) provide a clearer view of the planes outlined in red at the various stages of continuity.

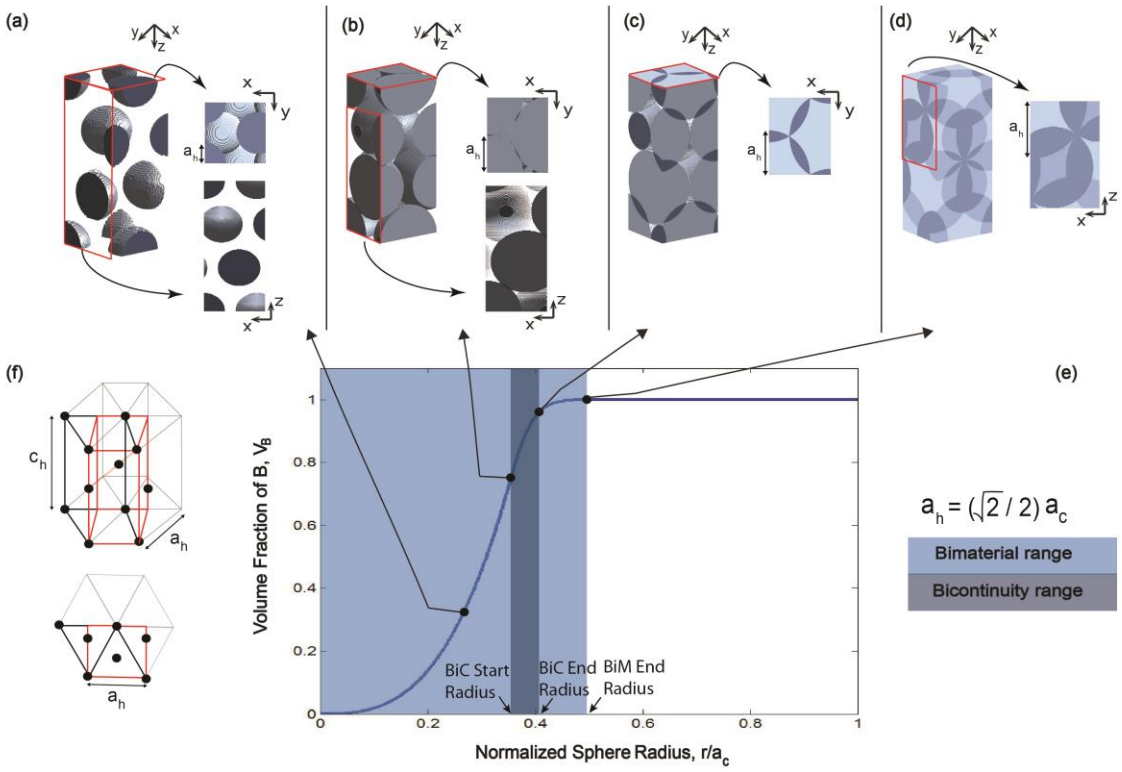

Figure 3.4 – Bicontinuity characteristics of a limiting case FCC rhombohedral structure. FCC unit cell (a) before the bicontinuous range, (b) at the start of the bicontinuous range, (c) at the end of the bicontinuous range and (d) at the end of the bimaterial range. The insets show the planes depicting the various stages of continuity, outlined in red. (e) Volume fraction of material B, the solid volume, as a function of the normalized sphere radius. (f) The rhombohedral unit cell under consideration shown by the red outline.

The bicontinuity characteristics were investigated both analytically and numerically to determine the above-described points of interest. The special case structures, produced by controlling the height-to-edge length ratio c_h/a_h, of the unit cells, at their various stages of bicontinuity are depicted in Figure 3.5. The bicontinuity interest points are listed in Table 3.2. Here, the parameters are given in terms of their hexagonal

lattice constants, a_h. These values can also be determined by applying the conversion equations given in Table 2.1 of the previous chapter with the parameter values given in Table 3.1.

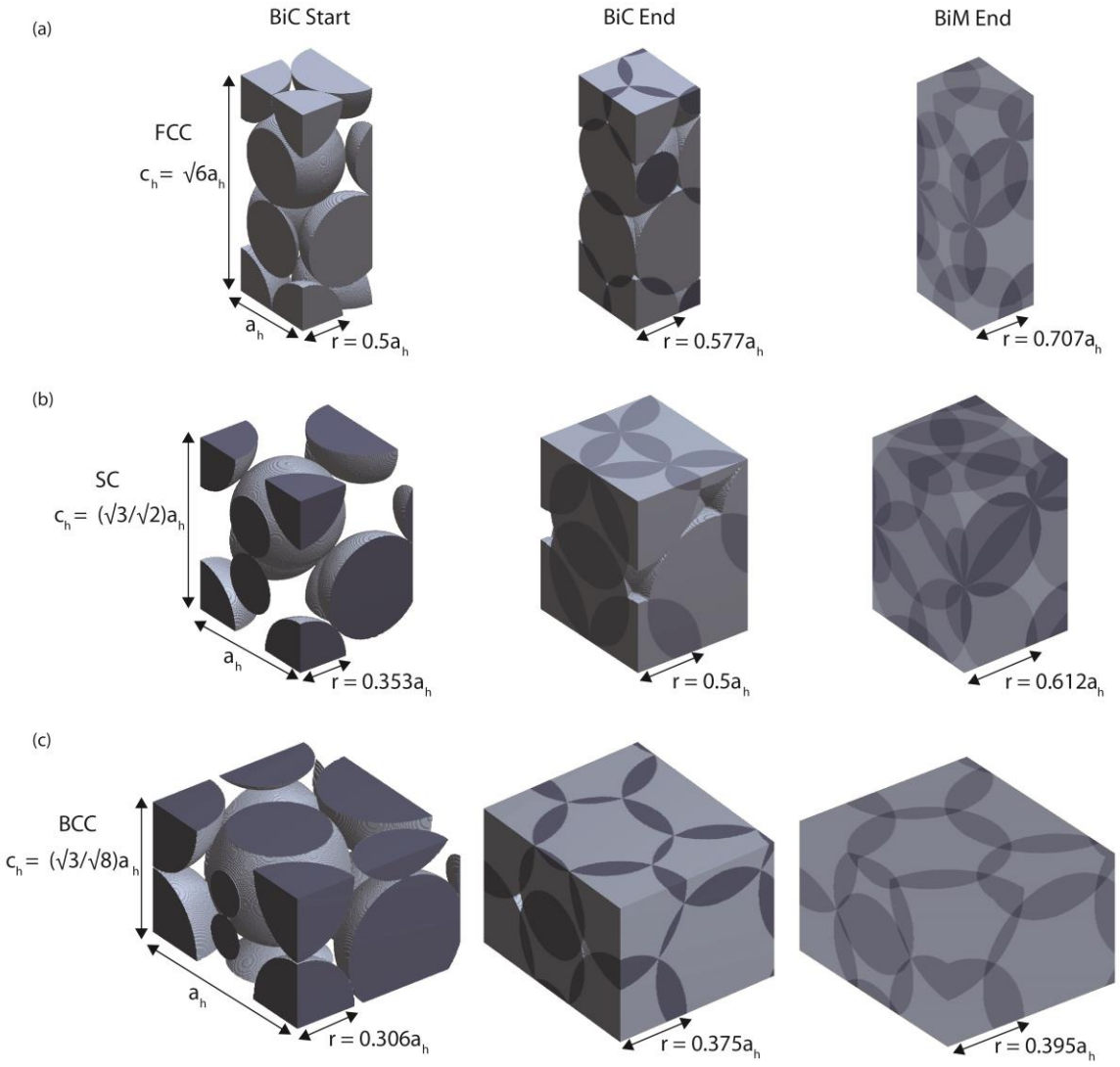

Figure 3.5 – Rhombohedral structures at various stages of bicontinuity. The (a) FCC, (b) SC and (c) BCC unit cells with the appropriate c_h/a_h ratio, at the start of the bicontinuous range, end of the bicontinuous range and end of the bimaterial range. The corresponding radius of the spheres are also depicted for each case.

Table 3.2 – Bicontinuity parameters for limiting case rhombohedral structures using the sphere-at-each-lattice site model

Structure	BiC Start Radius (a_h)	BiC End Radius (a_h)	BiM End Radius (a_h)
SC	$1/2\sqrt{2}$	1/2	$\sqrt{3}/2\sqrt{2}$
FCC	1/2	$1/\sqrt{3}$	$1/\sqrt{2}$
BCC	$\sqrt{3}/4\sqrt{2}$	3/8	$\sqrt{5}/4\sqrt{2}$

3.2 Bicontinuity Characteristics of the Multi Beam Interference (MBI) model

Using the (3+1)-beam and (4+1)-beam umbrella configurations, the rhombohedral and woodpile structures are generated respectively as described in the previous chapter. The limiting case structures are obtained by controlling the beam angle, θ_{beam}. The SC, FCC, BCC and DC structures thus obtained are depicted in Figure 3.6. The corresponding beam angles and periodicities obtained by Equations (2.7), (2.8) and (2.10) for periods in the *xy*- and *z*- directions are also labelled.

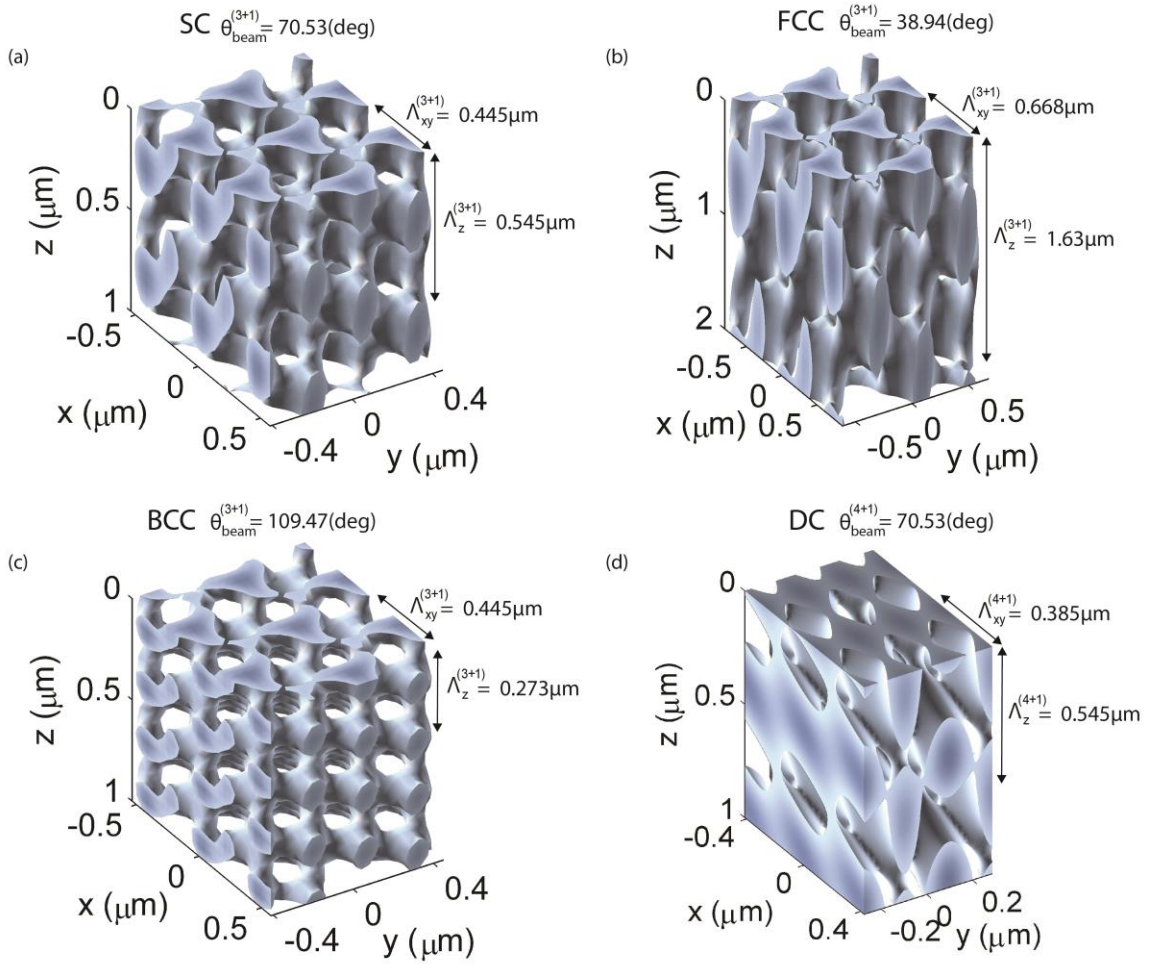

Figure 3.6 – Limiting case rhombohedral and woodpile structures formed by the (3+1)-beam and (4+1)-beam umbrella configuration respectively. (a) SC, (b) FCC, (c) BCC and (d) DC lattice structures and their corresponding periodicities and beam angles.

In a photo-sensitive medium such as a photoresist, the volume of the structures formed depends on the exposure dosage, development time, baking temperatures etc. The exposure dosage specifically, can be varied by controlling the exposure time and beam intensity. For a negative-tone photoresist like SU-8, the regions exposed to the UV light undergo crosslinking and are rendered insoluble. These regions are then retained after development while the unexposed regions are washed away. However, the photoresist possesses some inherent intensity threshold, only above which cross-linking occurs. The

interfering beams need to have a combined intensity value above this threshold intensity in order for the pattern to be recorded. Ideally, below this value the photoresist does not undergo any chemical changes and remains soluble for development. This binary nature of the photoresist can be modelled by specifying a normalized intensity threshold, I_{th} that determines the volume fractions of the resulting materials. Any intensity value in the interference pattern below this threshold leaves the photoresist unexposed and hence will be washed away and above it, will be retained. This intensity threshold is used as a variable to control the filling fraction of the constituent materials, thereby affecting the nature of interconnectedness in the resulting structures.

An example of the FCC limiting case rhombohedral lattice pattern is shown in Figure 3.7. The volume fraction of material B, which in this case is the void volume is represented as a function of the normalized intensity threshold in Figure 3.7(d). Similar to the sphere-at-each-lattice-site model analysis, the graph is divided into various regions of interest. As described in Section 2.6, the only region where the bicontinuity analysis is applicable for structures formed with photoresist as a medium, is the bicontinuous range. Outside this region, the structures are either completely solid, signifying a high exposure dose, or the structures collapse during development, signifying a very small exposure dose, in the case of a negative-tone photoresist. For other photosensitive materials like, photopolymerizable liquid crystals [115, 116], photorefractive [120] or photochromic materials [118, 119], the entire bimaterial range is physically realistic. These scenarios would be hypothetical for structures fabricated in photoresist. However, it indicates that stable structures are capable of being formed outside the bicontinuous range. In the graph, the bimaterial region ideally begins when material B starts to appear in the structure. This

does not happen for every non-zero intensity threshold value. There is a region up to about 0.05(I_{th}) where the intensity threshold is low enough for every point to be considered a solid volume i.e., there is no material B in the structure until that point. As the threshold increases, fewer number of points satisfy the intensity threshold condition and the material B volume increases. However, material B can only be seen to occur as isolated volumes or are disconnected from each other, whereas the solid A volumes are continuous throughout and thus, the structure is monocontinuous. This continues until the start of the bicontinuity range is encountered. Above this intensity threshold point, the structure is a bicontinuously-interconnected network where both materials A and B are continuous as shown in Figure 3.7(b). With further increase in the threshold intensity, the end of the bicontinuity region is reached. At this point, the threshold is high enough for the material B volumes to be continuous throughout the structure but the solid A volumes are not sufficiently interconnected and once again, the structure is monocontinuous. This state continues until the threshold is too high for material A to exist and the volume fraction of material B reaches unity. Near unity value of the normalized intensity threshold, the structure is no longer bimaterial. Figure 3.7 also shows the normalized surface area as a function of the intensity threshold on the right (red) axis. It can be seen that the surface area is highest in the bicontinuous range.

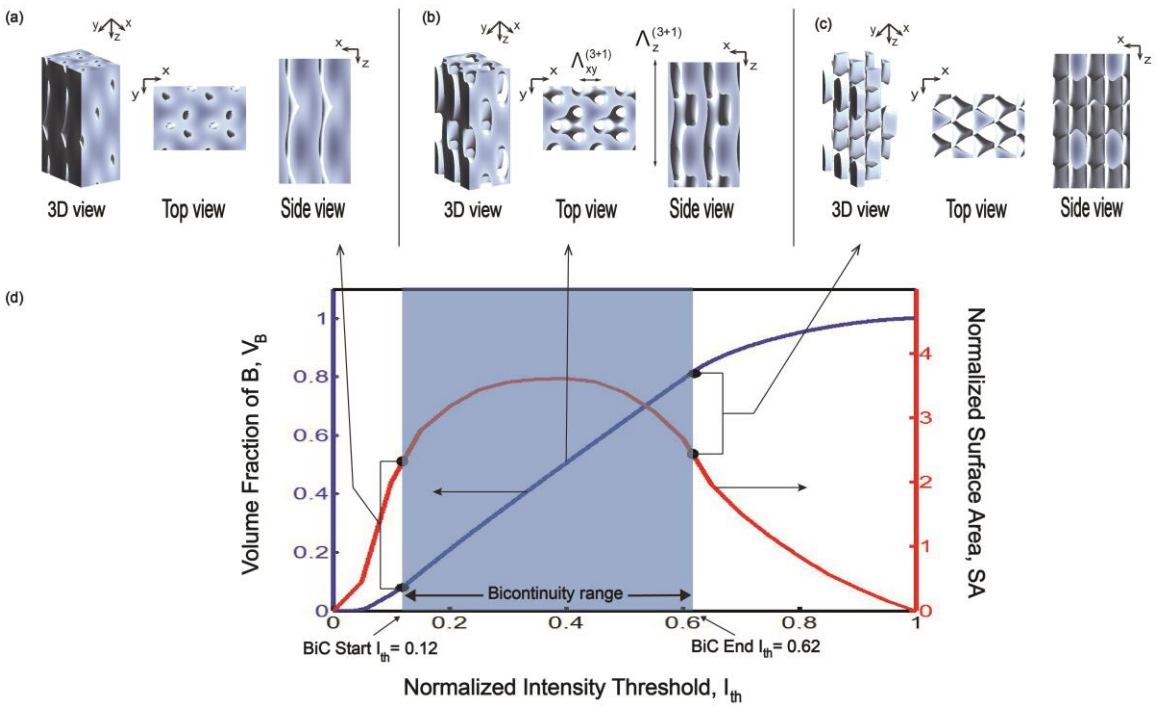

Figure 3.7 – Example of a FCC limiting case rhombohedral structure formed by setting θ_{beam} as 38.94°. (a), (b) and (c) show the 3D view, top view and side view of the structures at the start of the bicontinuous range, at the center of the bicontinuous range and at the end of the bicontinuous range respectively. (d) depicts the volume fraction (left) and normalized surface area (right) as a function of the normalized intensity threshold, I_{th}. The bicontinuity range occurs for I_{th}, ranging from 0.12 to 0.62.

For MBI structures the bicontinuous range is of significance as it describes certain unique properties of regular periodic structures. Only for a specific range of threshold intensities are both materials in the structure continuous. This bicontinuous range not only depends on the exposure dosage and processing conditions, together which determine the intensity threshold, but also on the symmetry of the structures that is determined by the polarization, amplitude and wavevectors of the beams. The range is described by the bicontinuity range start intensity threshold or BiC Start I_{th}, and the bicontinuity range end intensity threshold or BiC End I_{th}, which are each determined numerically by locating the intensity thresholds where either of the two materials cease to be continuous. Similar

analysis was carried out to determine the bicontinuity range for the SC, BCC and DC cases. The above example is shown for structures formed in air with the beams being azimuthally polarized. The bicontinuity characteristics were also studied for structures formed using radial incident polarization. The structures were investigated for their bicontinuity in photoresist as well, as described in the previous chapter. These results are detailed in the following section.

The surface area calculated above is larger than the actual surface area of the structures. This overestimation occurs since the surface areas of the cubical voxels, that are approximating the surface areas of the contours of constant intensity, will always be greater than the surface area of the contour itself. The surface formed by the voxels are irregular compared to the smooth surface of the contour. However, a correction factor can be derived to compensate for this effect. The surface area of the bends and undulations of the constant-intensity contours in relation to the surface area of the voxels representing the contours, can be approximated by the relationship of the known surface area of a sphere to the surface area of voxels representing the spherical surface. In the limit of smaller and smaller voxels, the surface area of the voxels is about 1.65 times larger than the surface area of the sphere. Thus, the above voxel-based calculated values are reduced by a factor of 1/1.65 in the following section. The estimation of this correction factor is included in Appendix B.

3.3 Bicontinuity Analysis Results

Figure 3.8(a) and (b) shows the results for azimuthally polarized beams producing rhombohedral structures in air. The graphs show the volume fraction of material B and the

normalized surface area as a function of the normalized intensity threshold. The graph is plotted through the entire bimaterial range and the bicontinuity ranges for the cubic limiting case structures are highlighted. The rhombohedral structures are bicontinuous for normalized intensity threshold values I_{th}, ranging from 0.12 to 0.62 with filling fractions corresponding to 8% and 81% respectively. A result of this analysis is that the bicontinuous range and the volume fractions remain unchanged for the various beam angles for the case of azimuthally polarized beams. The surface areas however show a decrease with increase in the beam angle as they depend on the space group of the structures formed. The bicontinuity range contains the maximum surface area region for the MBI structures. This is expected as the porosity is maximized at the center of the bicontinuous range where the filling fraction is around 50% for both materials. The SC and BCC cases display identical volume and surface area characteristics as the SC beam angle is essentially the same as that of the BCC beam angle (SC θ_{beam} = 180° - BCC θ_{beam}). The side beams travel in the opposite direction with respect to the central beam in the case of BCC symmetry.

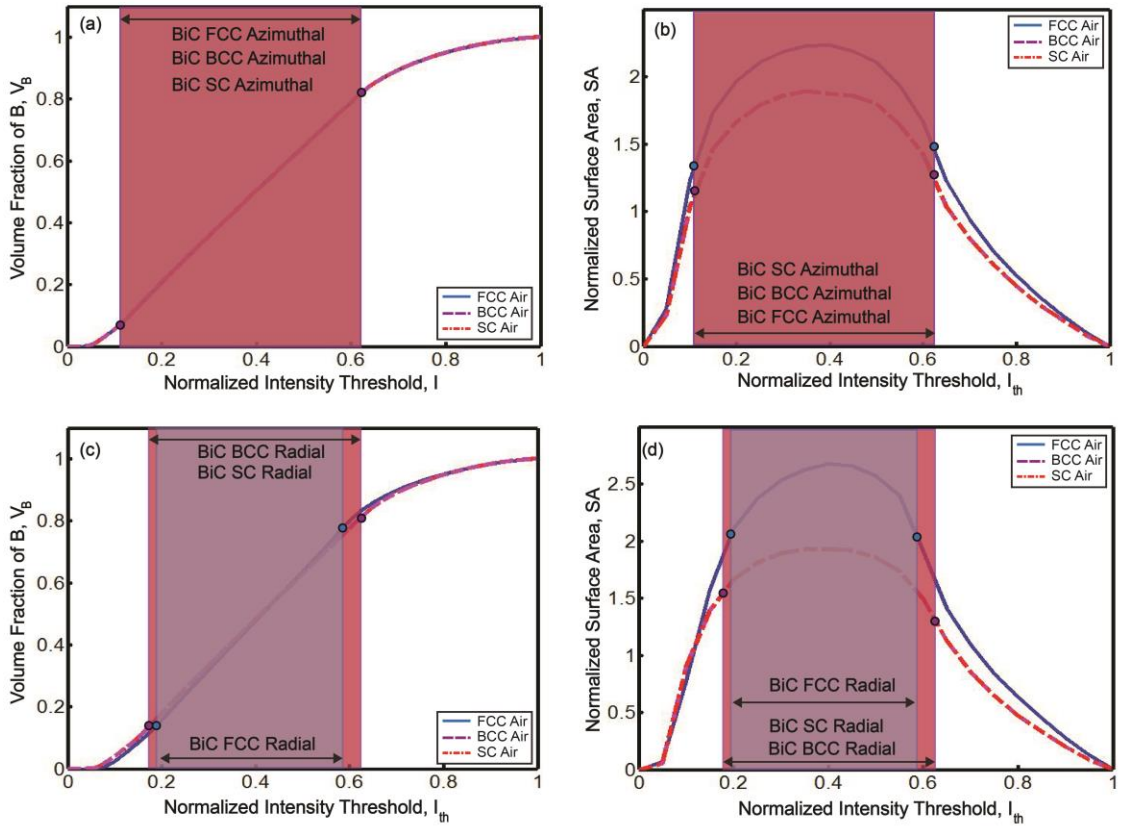

Figure 3.8 – For MBI structures generated with air as the medium and azimuthal incident polarization, (a) volume fraction of material B and (b) normalized surface area as a function of the normalized intensity threshold, for the FCC (θ_{beam} =38.94°), SC (θ_{beam} =70.53°) and BCC (θ_{beam} =109.47°) cases. The corresponding results for structures in air formed by radial incident polarization are shown in (c) and (d). The shaded regions denote the range wherein the structures are bicontinuous.

Furthermore, for structures in an idealized photoresist i.e., neglecting the absorption effects seen in the medium, the index-matched and unmatched cases show no change in the bicontinuity characteristics for azimuthal polarization, compared to the trends shown in Figure 3.8(a). Index-matching retains the required beam angle for the limiting case structures whereas in the unmatched case the beam angle changes, depending on the refractive index of the photoresist as described in the previous chapter. Thus it can be

concluded that the bicontinuous range and volumes are independent of the beam angle for the azimuthal polarization case.

For radially polarized beams, the change in beam angle causes a change in the bicontinuous range and their corresponding volumes. With an increase in the beam angle an increase in the bicontinuous range can be seen in Figure 3.8(c) and (d). This is because the level of interference between the beams in the interference pattern increases with increase in beam angle, given the symmetry of the beam configuration. This results in the interference pattern having a higher number of points with intensity values above the threshold. The maximum normalized surface area decreases with an increase in beam angle similar to that of the azimuthal case and shows dependence only on the beam angle. In photoresist, with index-matching, the bicontinuity characteristics remain unchanged as the beam angle remains the same. Without index-matching, the trends are in keeping with the results observed with structures in air, showing a strong dependence on the beam angle.

The structures are compared to their corresponding sphere-at-each-lattice-site model equivalents. The volume fraction of material B and the normalized surface area are plotted as a function of the normalized sphere radius as depicted in Figure 3.9. The limiting case rhombohedral structures are compared in Figure 3.9(a) and (b). Since the surface area depends on the space group symmetry, the FCC case with the highest number of spheres per unit cell, shows maximum surface area in all the representative models. The corresponding volume fraction and surface area of the DC structures are shown in Figure 3.9(c) and (d). For the sphere-at-each-lattice-site model, the maximum surface area occurs just before the spheres come in contact, i.e., right before the BiC Start radius. After the BiC Start radius is reached, the overlapping spheres result in a sharp decrease in the surface

area. Also, the surface areas of the sphere-model structures are larger than their MBI counterparts. This occurs because, the abrupt interface transitions from sphere-to-sphere as opposed to the smooth contours of constant intensity in MBI gives rise to larger interface areas for the sphere-at-each-lattice-site structures and larger volumes for the MBI-formed structures.

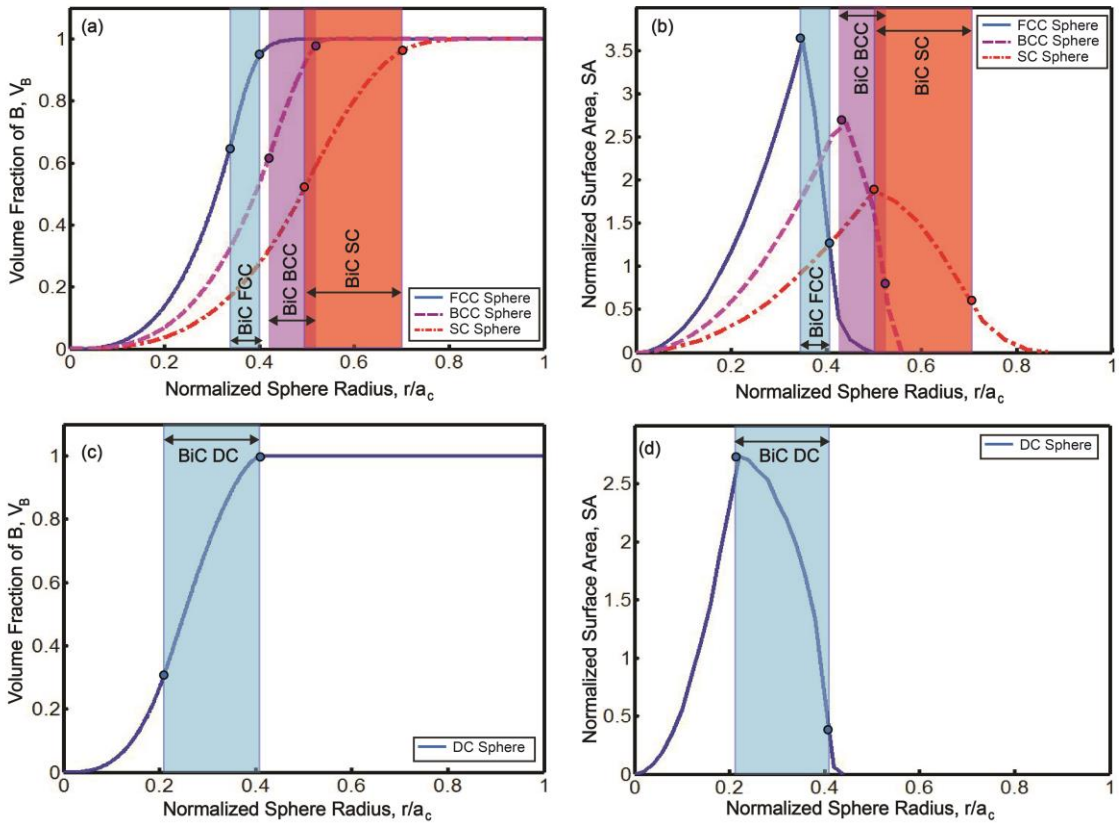

Figure 3.9 – For the sphere-at-each-lattice-site structures (a) volume fraction of material B and (b) normalized surface area as a function of the normalized sphere radius for the FCC, SC and BCC cases. The corresponding results for the DC structures are shown in (c) and (d). The shaded regions denote the range wherein the structures are bicontinuous.

Similar analyses were performed for the woodpile lattice structures. The patterns were studied in air as well as in photoresist, for both types of polarization. The results for

the azimuthally polarized beams in air are shown in Figure 3.10(a) and (b). This corresponds to the perfect DC structure where, the ratio between the periodicity in the *z*-direction, Λ_z and periodicity in the xy-direction, Λ_{xy} is $\sqrt{2}$. This case occurs when the beam angle equals 70.53° as described earlier. The bicontinuous range can be seen for normalized intensity thresholds ranging from 0.31 to 0.38 with a corresponding volume fraction from 40% to 55% respectively. When the beam angle is changed, no change is observed in the bicontinuous characteristics for azimuthally polarized beams as expected. As a result, the index-matched and unmatched structures demonstrate similar bicontinuous ranges.

For radially polarized beams, unlike the rhombohedral case, the bicontinuity range increases with decrease in beam angle. The results comparing the ideal DC (θ_{beam} =70.53°) and an arbitrary angle or non-ideal DC (θ_{beam} =34.37°) structures are shown in Figure 3.10(c) and (d). The decrease in bicontinuity range is accompanied with greater volumes for structures formed by larger beam angles. This can be attributed to the symmetry in the resulting interference pattern. By virtue of the symmetry, even as the number of interfering points above threshold decreases, the skewing of the pattern by a smaller beam angle causes a higher degree of interlinking between nearby columns in the square lattice symmetry structures, thereby increasing the bicontinuity range. A similar reasoning can be given to the decrease in the maximum surface area with a decrease in the beam angle. The reduction in the volume fraction and surface areas suggest that the volumes being added to the final structure, as a result of an increase in the intensity threshold, are not generating additional points for the final structure, rather they are only adding to existing points that already satisfy the intensity threshold condition.

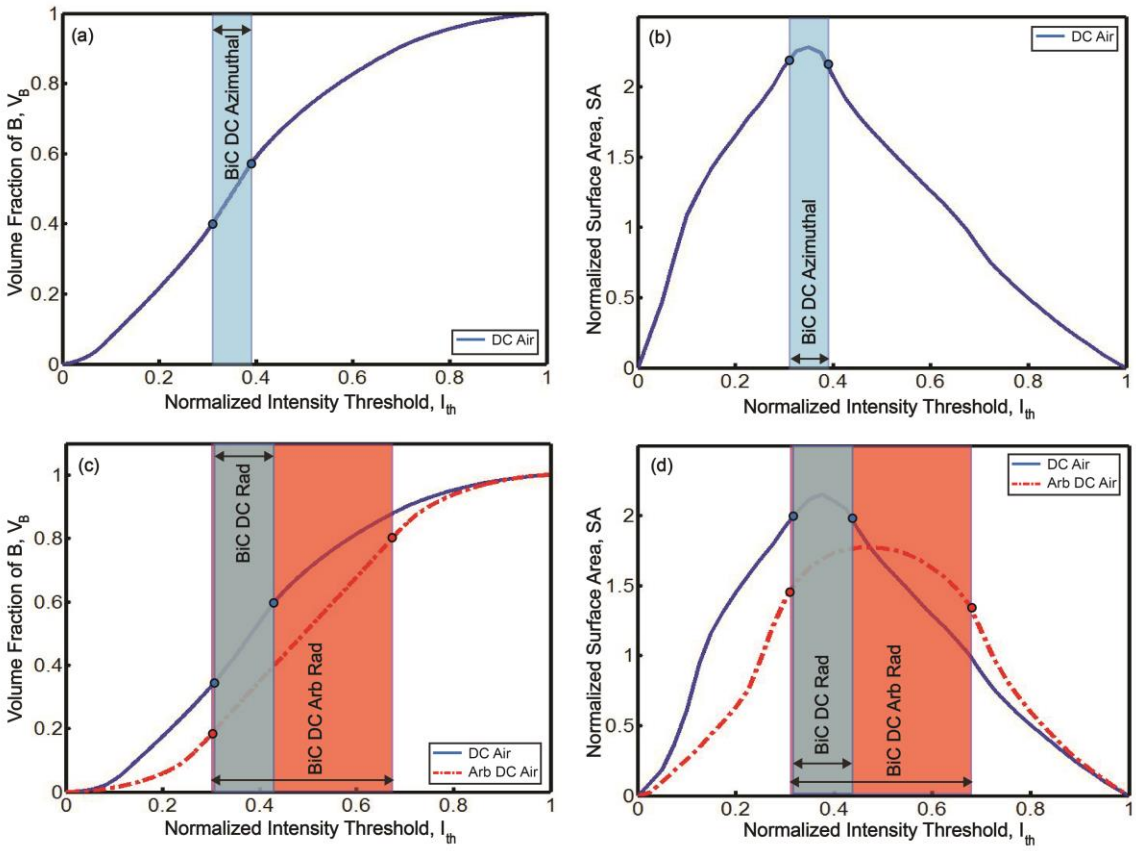

Figure 3.10 – For MBI structures generated with air as the medium and azimuthal incident polarization, (a) volume fraction of material B and (b) normalized surface area as a function of the normalized intensity threshold, for the ideal DC (θ_{beam} =70.53°) case. The corresponding results for structures in air formed by radial incident polarization are shown in (c) and (d) for the ideal DC (θ_{beam} =70.53°) and non-ideal DC (θ_{beam} =34.37°) cases. The shaded regions denote the range wherein the structures are bicontinuous.

When the absorption and standing wave effects are taken into consideration for the structures in photoresist, significant differences are observed in the bicontinuity characteristics. Contrary to the structures in uniform media, the rhombohedral structures show a decrease in the bicontinuity range with an increase in the beam angle. The volume fractions and surface areas for the FCC (θ_{beam} = 38.94°), SC (θ_{beam} = 70.53°) and an arbitrary angle of θ_{beam} = 80° are shown in Figure 3.11(a) and (b). There is also a shift in the bicontinuous range towards higher threshold intensities with a decrease in the

corresponding volumes. The results signify a decrease in the level of overlap with increasing beam angles. This can be attributed to the refraction effects arising between the various layers of the photoresist. Similarly, the bicontinuity characteristics observed for DC structures in photoresist are the converse of the effects observed for DC structures in air. The volumes and surface areas for the ideal and non-ideal DC structures are depicted in Figure 3.11(c) and (d). Here, the bicontinuity range decreases with a decrease in beam angle, but with an increase in the volume fraction. The refraction in the photoresist causes skewing of the patterns for larger beam angles that were observed for small angles in air. The surface areas for both the beam configurations show a dependence on the beam angle, similar to the structures in air. The common feature in each of these cases is the linear progression of the volumes in the bicontinuous range. It can be inferred that within the bicontinuous range, every change in the intensity produces a corresponding change in the volume fraction. This characteristic is independent of the incident polarization, beam angle, beam configuration and medium in which the structures are formed.

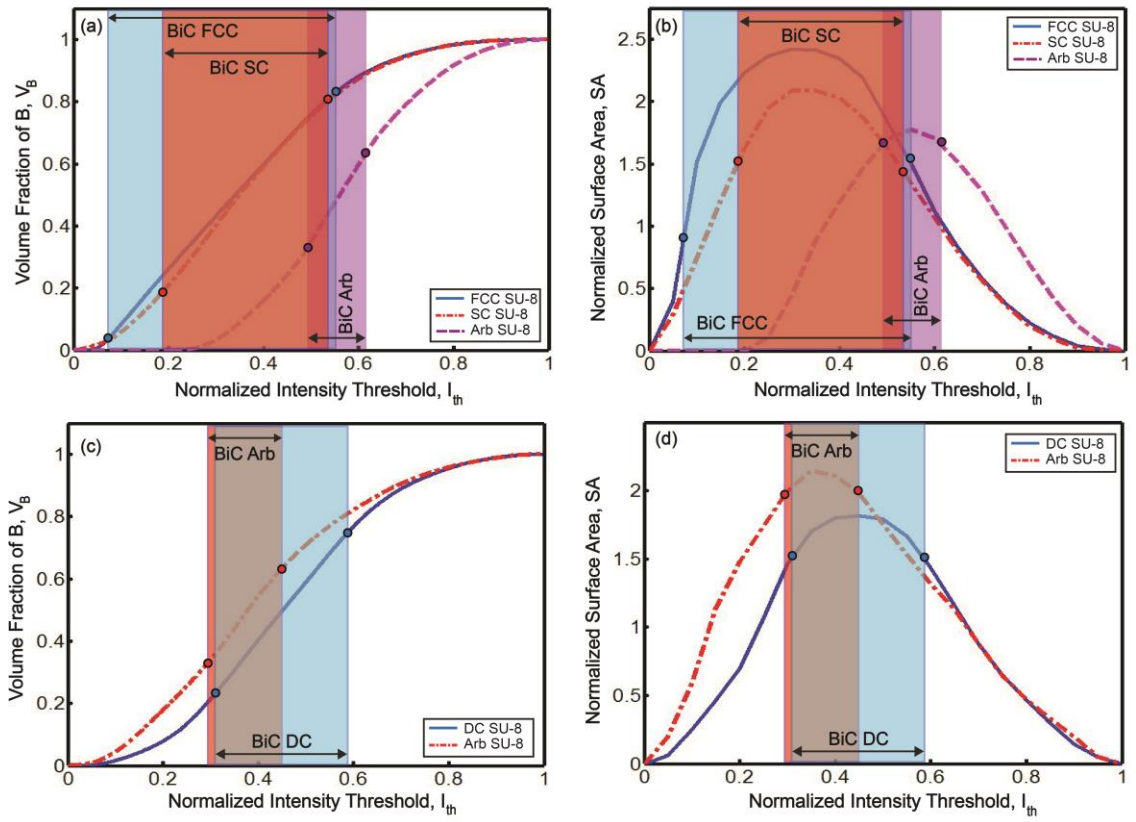

Figure 3.11 – For MBI structures generated with SU-8 as the medium and azimuthal incident polarization, (a) volume fraction of material B and (b) normalized surface area as a function of the normalized intensity threshold, for the FCC (θ_{beam} =38.94°), SC (θ_{beam} =70.53°) and arbitrary angle (θ_{beam} =80°) cases. The corresponding results for woodpile structures in SU-8 are shown in (c) and (d) for the ideal DC (θ_{beam} =70.53°) and non-ideal DC (θ_{beam} =34.37°) cases. The shaded regions denote the range wherein the structures are bicontinuous.

3.4 Summary

The bicontinuity parameters for the representative models were defined and determined as a function of the normalized sphere radius and normalized intensity threshold for the sphere-at-each-lattice-site model and the MBI model respectively. The intensity threshold can be used as a measure to model the effects of the exposure dosage on the interference pattern and is used to control the volumes of the constituent materials. The bicontinuity range and volumes of rhombohedral and woodpile structures in air and

photoresist as a uniform medium show a dependence on the beam angle for radially polarized beams but remain unchanged for azimuthally polarized beams. For more realistic lithographic conditions, the effects observed are contrary to those seen for structures formed in air. The surface areas show a dependence on the beam angle irrespective of the polarization and mediums considered. The symmetry of the structures, determined by the beam configuration, plays a significant role in the bicontinuity characteristics, which can be seen from the differences between the hexagonal and square lattice symmetry structures.

CHAPTER 4. PATTERN-INTEGRATED INTERFERENCE LITHOGRAPHY

Multi-Beam Interference Lithography (MBIL) lacks the ability to fabricate periodic-lattice-based-microstructures with functional devices, in a single, rapid step. This calls for a technique that can combine interference and imaging to produce customized interference patterns. Pattern-Integrated Interference Lithography (PIIL) is the only known method that is capable of producing such customized patterns with a single exposure and is described here in this chapter.

4.1 Pattern-Integrated Interference Lithography Concept

In traditional holography, interference between a reference wave and subject wave is used to produce an interference pattern that contains information about the object-dependent subject wave [127, 128]. Holographic techniques have been used extensively to produce periodic templates for the fabrication of photonic crystal devices [129-131]. As an extension of holography, PIIL can be described as the integration of superposed pattern imaging with interference [132]. It is comprised of multiple waves, each acting as both the subject and reference waves in a holographic configuration. When these waves are superposed, it results in a complex optical-intensity distribution composed of a periodic lattice, modified by an integrated mask pattern. The periodic lattice here is defined by the configuration of the beams and the mask patterns are non-periodic functional elements such as a resonator cavity, waveguide etc [133]. The advantage of PIIL is in its ability to produce such non-periodic functional elements within a 2D or 3D periodic lattice without an additional lithographic step.

The conceptual PIIL system is depicted in Figure 4.1(a). It consists of an 8*f* confocal lens configuration starting from the expanded lenses (ELs), the condenser lens (CL), and finally, the two objective lenses (OL1 and OL2). The multiple beams are each individually controlled in their amplitudes and polarizations by a series of half-wave plates and polarization beam-splitter cubes prior to entering the expander lenses and are not shown in the diagram for clarity. The beams are focused, collimated, focused and collimated as they pass through the system to produce ultimately the desired interference pattern. The lateral beam displacement d_{beam}, from the optical axis in the *z*-direction determines the common incidence angle θ_{beam}, of the beams at the back focal plane of OL2 [134]. The result is a uniform-periodic interference pattern with a lattice constant proportional to the source wavelength and inversely proportional to the sine of the incidence angle, similar to MBIL described earlier [133]. OL1 and OL2 form a compound objective lens (COL) system with an object and image plane at the front focal plane of OL1 and back focal plane of OL2 respectively. This COL system is arranged in a Fourier transform configuration. When the beams produce Fourier transforms of an object placed at the object plane, such as a photomask, OL2 performs an inverse Fourier transform to give the original mask image. This image however, is upside-down and left-right reversed and demagnified by a factor equivalent to the ratio between the focal lengths of the objective lenses, $M = f_{OL2} / f_{OL1.}$ Each beam produces its own image of the photomask object which then interferes to give a custom-modified interference pattern [72].

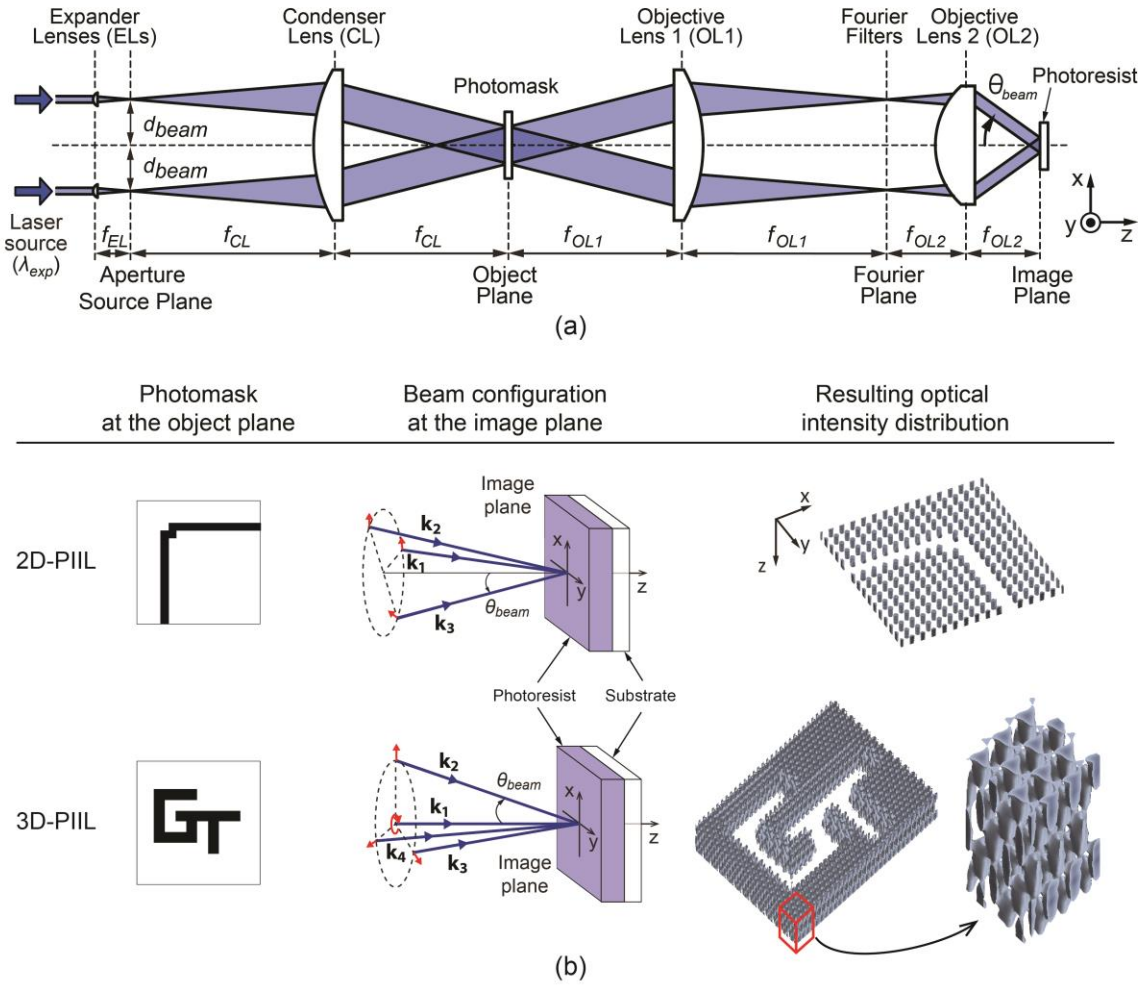

Figure 4.1 – (a) The conceptual 8*f* confocal PIIL system where multiple beams containing images of the photomask are superposed to give a custom-modified interference pattern. (b) Examples of mask patterns produced by 2D and 3D beam configurations and their resulting structures [72].

Examples of photomask objects and the resulting interference patterns produced by certain beam configurations are shown in Figure 4.1(b). The resulting pattern thus depends on the number of beams, the exposure wavelength, as well as individual beam parameters such as their amplitudes, polarizations and wavevectors. The source positions at the aperture source plane (front focal plane of ELs) influence the wavevector configuration and hence the plane group symmetry of the structures at the image plane. Partial coherence

can be introduced into the PIIL system by adjusting the position of the expander lenses, and yet maintaining collimation at the image plane, to eliminate ringing and speckle effects that are typically seen in highly coherent illumination systems [82]. This improves the interference/imaging capabilities of the exposure system. For microfabrication purposes, registering this pattern on a photosensitive material such as a photoresist, placed at the image plane is necessary.

4.2 Pattern-Integrated Interference Lithography Research Areas

The research in PIIL has been carried out in several areas including the development of a comprehensive simulation tool, photomask design, evaluating the exposure system, and producing proof-of-concept results through experiments. These results are summarized in the following sections.

4.2.1 PIIL Model

In order to facilitate the understanding of PIIL's capabilities and limitations, a comprehensive PIIL model had to be developed, that combined multi-beam imaging and interference. Commercial lithography simulation software lacked the necessary flexibility that was needed to simulate multiple-off-axis-imaging and interference simultaneously.

The primary requirement of such a model was to account for the effects observed in a high numerical aperture (NA) exposure system. A high-NA objective lens is desired in order to reduce the minimum feature size, and decrease the lattice constant achievable by increasing the beam angle θ_{beam}. High-NA is attained by placing the lens in immersion fluids thereby increasing the refractive index of the medium and consequently increasing the NA of the lens [135, 136]. As described in CHAPTER 2, the high-NA system causes

the electric field of the beams to develop components in directions not limited to the incident plane. This rotation of the electric fields affects the symmetry and contrast of the resulting interference pattern. Thus, a scalar model for representing the PIIL system was deemed inadequate and a new vector model was developed that accounted for the high-NA imaging effects. The PIIL model uses Flagello's formalism to calculate the vector electric fields in a stack of thin films on a substrate from high-NA systems. In Flagello's 3D vector model, the electric field of the ith interfering beam is given by [137],

$$\begin{aligned}\mathbf{E}_i(x,y,z) = \mathcal{F}^{-1}\big[&\mathbf{M}_F^{3\times5}(\alpha,\beta,z)\mathbf{M}_P^{5\times2}(\alpha,\beta)\mathbf{E}_i^{ill}O(\alpha,\beta)\\ &\times P(\alpha,\beta)\;\; S(\theta_{beam},\varphi_i)\;\exp(-j2\pi\gamma z_0)\\ &\times\exp(-j2\pi W(\alpha,\beta))\,C(\alpha,\beta)\big]\end{aligned} \tag{4.1}$$

where (x,y,z) are the Cartesian coordinates in the image space; $\mathcal{F}^{-1}$ is the inverse Fourier transform; α, β, and γ are the direction cosines in the Fourier space normalized with respect to the image-side NA; $\mathbf{M}_F^{3\times5}(\alpha,\beta,z)$ is a 3×5 film function matrix that accounts for the polarization dependent reflections, transmission, and absorption of the downward- and upward-traveling electric fields at the interfaces between the stacked thin films; $\mathbf{M}_P^{5\times2}(\alpha,\beta)$ is a 5×2 electric field correction matrix that accounts for high-NA-based polarization changes produced by OL2; $\mathbf{E}_i^{ill}$ is the input 2×1 vector electric field defined in the xy-plane of the ith beam illuminating the photomask; $O(\alpha,\beta)$ is the Fourier transform of the photomask object assuming a thin-mask approximation; $P(\alpha,\beta)$ is the pupil function ($P(\alpha,\beta)$ = 1 for $\sqrt{\alpha^2+\beta^2}\leq 1$, 0 otherwise); φ_i is the beam azimuthal angle at the image plane; $S(\theta_{beam}, \varphi_i)$ describes the off-axis propagation of the beam; z_0 is the distance between the image focal plane and the surface of the photoresist film and represents a defocus term;

$W(\alpha,\beta)$ is the optical path difference function due to lens aberrations; and $C(\alpha,\beta)$ is the obliquity factor included for energy conservation [72]. The $W(\alpha,\beta)$ function was calculated from the 37 fringe Zernike polynomials for a rotationally symmetric system and is expressed as

$$W(\alpha,\beta) = \sum_{i=1}^{37} \frac{a_i Z_i(\alpha,\beta)}{\lambda}, \tag{4.2}$$

where a_i is the fringe Zernike coefficient of the i^{th} Zernike polynomial. The coefficients were calculated for the PIIES objective lens using the ray-tracing software ZEMAX. The electric fields computed above for each beam are then combined using the time-averaged intensity expression for multiple interfering, monochromatic waves given by

$$I_{PIIL}(\mathbf{r}) = \frac{c_0}{2} \operatorname{Re}\left[\sum_{i=1}^{N} \mathbf{E}_i(\mathbf{r}) \cdot \sum_{i=1}^{N} \mathbf{E}_i^*(\mathbf{r}) \right]. \tag{4.3}$$

The final intensity distribution described above gives the photomask integrated intensity distribution in the periodic lattice. This intensity distribution varies through the volume of the photoresist due to defocus effects, absorption in the photoresist and off-axis propagation of the beams [72]. The refractive index mismatch between the photoresist and the substrate gives rise to standing waves that is accounted for in Equation (4.3). This extensive model was implemented in MATLAB and was also integrated into a software package with a graphical user interface (GUI) shown in Figure 4.2. The GUI allows the user to define the mask element and shape, lattice constant, resolution, defocus, magnification, NA, beam configuration, imaging medium and the plot parameters.

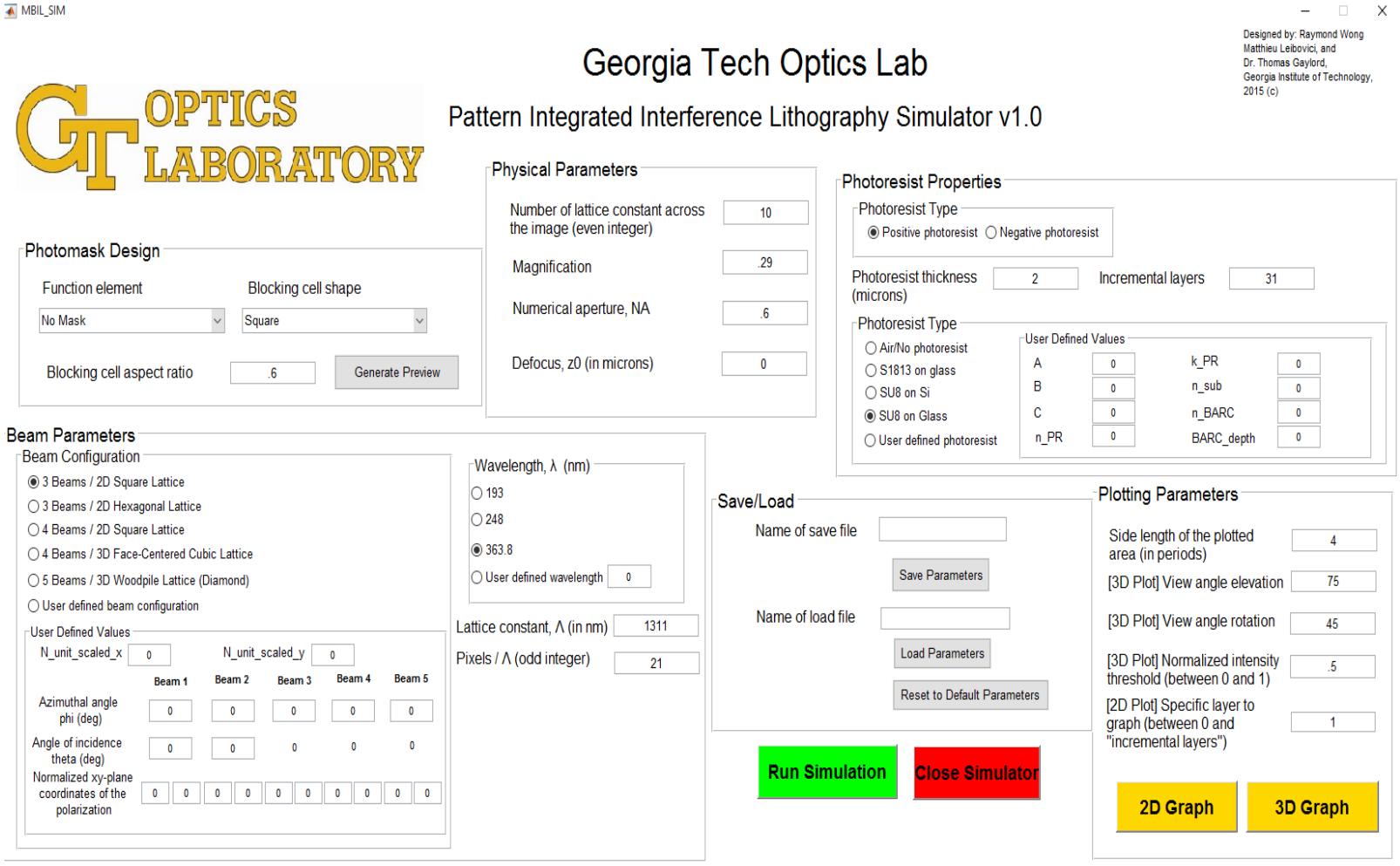

Figure 4.2 – Screen capture of the PIIL GUI

4.2.2 Photomask Optimization

The images of the photomask by the individual beams are not exactly reproduced when projected by the objective lenses at the sample plane. The interference patterns contain irregularities due to distortions that occur during propagation through the system. In lithography, to increase the resolution of the features and to reduce the nonconformities between the photomask image and latent image, optical proximity correction (OPC) techniques are employed [138]. For PIIL, OPC was done to reduce the undesired distortion by pre-compensating for the imperfections observed due to diffraction, defocus and off-axis imaging. For this purpose, a photonic crystal (PhC) 90*deg*-bend waveguide was generated comprising of a 2D square lattice of silicon pillars with periodicity

$$\Lambda_{sq} = \frac{\lambda_{exp}}{\sqrt{2}\,\sin\theta_{beam}}. \tag{4.4}$$

The distortion caused by a single motif-blocking element on the eight neighboring pillars was investigated. The objective was to determine the shape and size of the blocking pattern that caused the least amount of distortion. Five geometric shapes and nine widths ranging from 0.5 Λ_{sq} / *M* to 1.3 Λ_{sq} / *M;* where, *M* is the magnification of the compound objective lens, were considered. The distortions were quantified by a pillar displacement error given by

$$e_{disp} = \frac{d}{\Lambda_{sq}}, \tag{4.5}$$

and pillar area error given by

$$e_{area} = \frac{\sum_{m,n}|v(m,n) - \tau(m,n)|}{\sum_{m,n}\tau(m,n)}, \tag{4.6}$$

where, *(m,n)* are the pixel indices within the 101*px* x 101*px* area, $v(m,n)$ and $\tau(m,n)$ are the binary pixel values of the estimated and reference pillars respectively, and *d* is the distance between the center of their masses. These quantities, along with the geometries considered for distortion calculation are depicted in Figure 4.3. For each combination, the pillar area and displacement errors were computed for the closest neighboring pillars and averaged. The geometric mean of the averaged values were calculated as a figure of merit to determine the pattern that produced the least distortion. It was concluded that the 45*deg*-rotated square with a width of $0.9\Lambda_{sq}/M$ had the lowest imperfections. Therefore, it was used to create an improved photomask design.

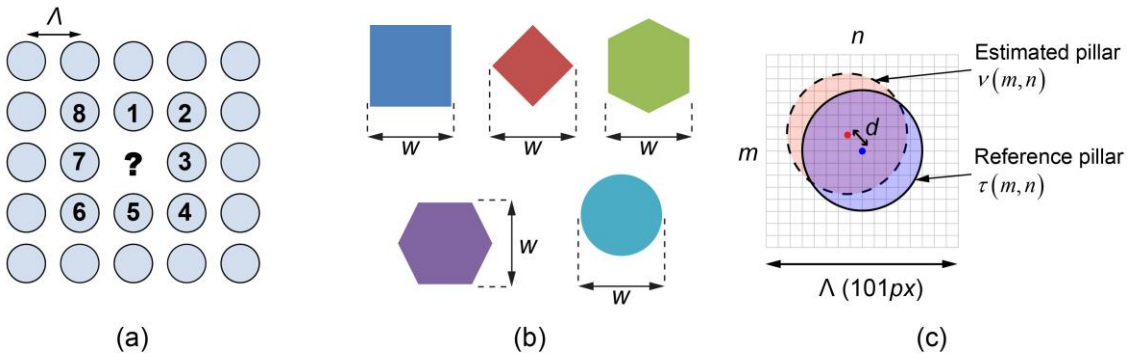

Figure 4.3 – (a) Schematic representation of the photomask design problem in PIIL. (b) Five possible geometric shapes for the single-motif-blocking photomask. (c) Illustration of the symbols used in Equations 4.5 and 4.6 [84].

The 90*deg*-bend waveguide was generated with this improved photomask design and compared to the elementary mask design with Λ_{sq}/M wide square patterns. The improved photomask design showed lesser distortions that progressively decreased in pillars located away from the waveguide. The PIIL-produced PhC waveguide was

simulated in COMSOL and the transmission spectrum was compared to that of an idealized device with no distortions. It followed that, the PIIL-produced device performed almost as good as the idealized device as depicted in **Figure 4.4** [84], even with a slight decrease in the effective waveguide width. Similar performance results were obtained when stop band and pass band filters generated by PIIL were compared to their idealized counterparts [139].

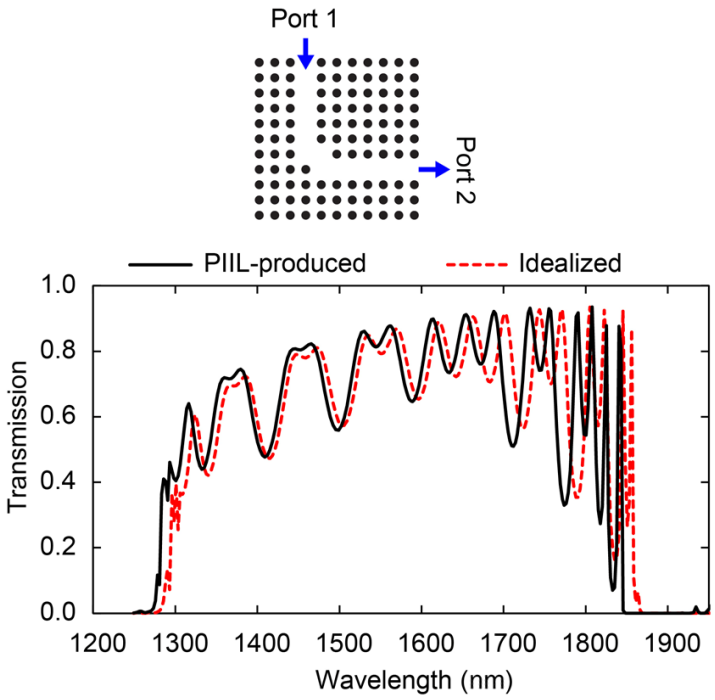

Figure 4.4 – Transmission spectra between Port 1 and Port 2 of the PIIL-produced (solid lines) and idealized (dashed lines) PhC 90*deg* bend waveguide [84].

4.2.3 PIIL Exposure System Analysis

The conceptual PIIL system depicted in Figure 4.1(a) is implemented using commercial and custom-made optics and mounts. A Spectra-Physics argon-ion UV laser, operating at a wavelength, $\lambda_{exp} = 363.8nm$ is used for the exposures. Three large-diameter commercially available, antireflection-coated aspheric lens were used for the condenser

and first objective lens and the second objective lens with a design wavelength λ_{des} = 780*nm*. The range of feasible angles at the image plane θ_{beam}, is determined using ZEMAX and is related to the lateral beam displacement from the *z*-axis, d_{beam}. Due to physical constraints of the opto-mechanical system, the incident angles at the image plane can only range from 5*deg* to 30*deg*. The positioning of the optical elements were optimized for various values of θ_{beam} using ZEMAX by setting the distances between the elements, shown in Figure 4.5, as variables. The results suggest that the CLs, mask mount and OL1 can remain relatively fixed for the different beam angles whereas the ELs, OL2 and sample mount need to be repositioned [140]. The relationship between θ_{beam} and the interference periods is used to derive the relationship between d_{beam} and the periods for typical 2D and 3D hexagonal and square lattice structures, which is a more practically useful relationship from an experimental perspective. The extreme case values for the periods are listed in Table 4.1 [72].

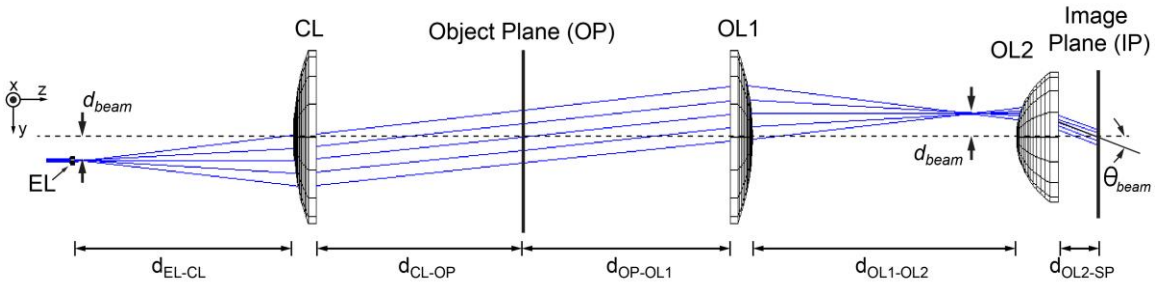

Figure 4.5 – ZEMAX-model of the PIIL exposure system showing the propagation of a single beam [72].

The interference pattern was also analyzed for its sensitivity to beam misalignment. A decentered beam is analyzed, that has a different d_{beam}, θ_{beam} and azimuthal angle compared to a centered beam. The 1D grating produced by this decentered beam along with a perfectly aligned beam was investigated for errors in periodicity and orientation angle. It was shown that for a maximum of $\pm 0.5mm$ displacement error on the xy-plane, the fringe period error ranges from -3.34% to 3.6% and the fringe orientation error ranges from -1.98*deg* to 1.99*deg* [72].

Table 4.1 – Range of feasible interference periods and d_{beam} of the PIIL exposure system [72]

	$d_{beam}\,(mm)$	$\Lambda_{sq}\,(\mu m)$	$\Lambda_{hex}\,(\mu m)$	$\Lambda_{xy}^{(3+1)}(\mu m)$	$\Lambda_{xy}^{(4+1)}(\mu m)$	$\Lambda_z\,(\mu m)$
$\theta_{beam} = 5deg$	4.95	2.95	2.78	4.82	3.99	160
$\theta_{beam} = 30deg$	27.19	0.51	0.49	0.84	0.70	1.1

The imaging capabilities of the COL system were analyzed for perfectly aligned and imperfectly aligned lenses using ZEMAX. The difference in the design and experimental wavelength limits the performance of the PIIL system, even when it is perfectly aligned. The root mean square optical path difference (RMS OPD) was computed using the 37 fringe Zernike polynomials to study the effect of the wavelength difference. The spherical aberrations that result from using an exposure wavelength that is different from the design wavelength caused the system to produce almost twice as much RMS OPD (0.46*waves*) as the acceptable limit for a diffraction-limited system (0.25*waves*). Without

this difference the RMS OPD value for the COL system is almost negligible (0.003*waves*). For analyzing the effects of leans tilting and decentering on imaging, OL1 and OL2 were imperfectly aligned separately. It was shown that OL1 is more sensitive to decentering whereas OL2 is more sensitive to tilting. It was concluded that the maximum acceptable tilt error for OL2 and displacement error for OL1 at the experimental wavelength are $5\times10^{-3} deg$ and $25\mu m$ respectively. Furthermore, the ZEMAX distortion grid analysis tool was used to analyze the image distortions across the field of exposure at the image plane. The coordinates of the imaged grid points were compared to the reference coordinates of the undistorted image. From these grid point coordinates, a distortion error was calculated as a difference in the radial distance between the points. The maximum RMS distortion error in a $2.5mm$ x $2.5mm$ area was determined to be around $26.6\mu m$. Also, the field of exposure with RMS distortion error < $0.5\mu m$ was smaller than $0.2mm^2$ around the optical axis. These values showed no significant improvement for the case of the exposure wavelength being equal to the design wavelength [72].

4.3 Summary

The drawbacks of MBIL have been addressed by PIIL, a novel technique that combines interference and imaging in a single exposure step. Extensive research has been conducted to quantify the capabilities of this rapid technique. The conceptual PIIL system has been implemented using commercial lenses and mounts. A comprehensive high-NA PIIL model was developed that allows for a realistic simulation of the structures formed. This model was also integrated into a PIIL simulator software package with a GUI. The photomask design was optimized by means of employing techniques similar to OPC in conventional photolithography. The PIIL exposure system was analyzed using ZEMAX

to study the sensitivity to beam tilting and decentering and also, lens tilting and decentering. The limits of the system in terms of the maximum tilt and displacement were defined and the maximum distortion across the field of exposure, determined. The experimental demonstrations of PIIL will be discussed in the following chapter.

CHAPTER 5. THREE-DIMENSIONAL PATTERN-INTEGRATED INTERFERENCE LITHOGRAPHY EXPERIMENTAL DEMONSTRATION

The prototype Pattern-Integrated Interference Lithography (PIIL) system described in the previous chapter is implemented to provide proof-of-concept results through experiments. The system components, followed by an improved alignment procedure for the PIIL system is described. The processing steps for fabricating 3D lattice-based microstructures are also given, and experimental results presented.

5.1 PIIL Implementation

The top-view schematic of the PIIL system is depicted in Figure 5.1. An argon-ion UV laser operating at an exposure wavelength of 363.8*nm* is used as the laser source. A single laser beam from the source is divided into the desired number of beams by employing a series of half-wave plates (HWPs) and polarization beam splitter cubes (PBSCs). By rotating a HWP placed before a PBSC, it is possible to control the ratios of the intensities of the output beams exiting the PBSC. A HWP placed after a PBSC is used to control the polarization of the beam exiting the HWP. Using these techniques, each beam is individually controlled in amplitude and polarization to give the desired exposure configuration. The entire configuration is placed on a vibration isolation optical table. Multiple mirrors are used to redirect the beams in the required directions. The optical axis is defined along the *z*-axis in this configuration.

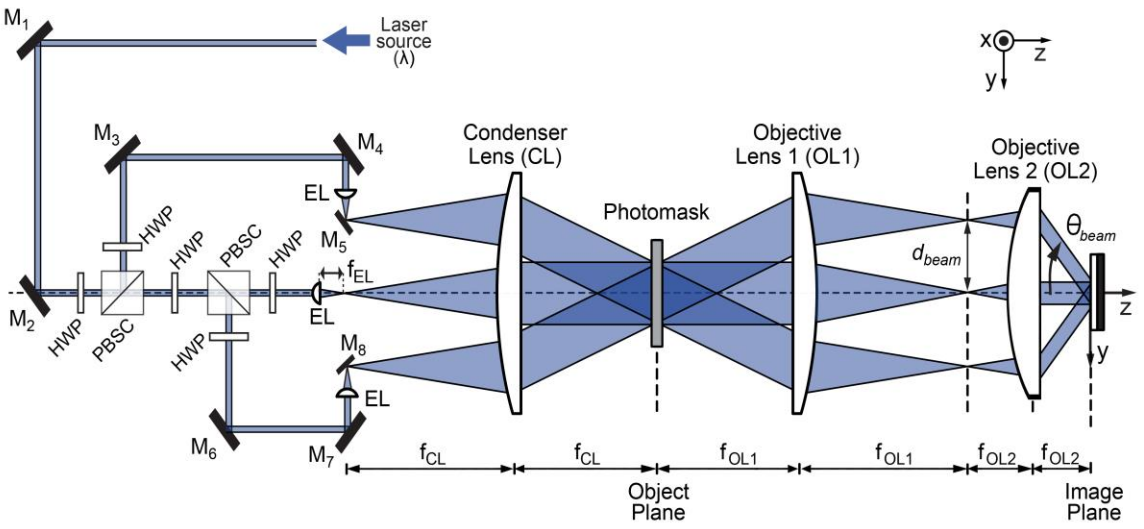

Figure 5.1 – Top-view schematic of the PIIL exposure system.

A high-NA objective lens with a NA of 0.62 at a design wavelength, λ_{des} of 780*nm* is chosen as objective lens 2 (OL2) and has a focal length f_{OL2} = 60*mm*. The condenser lens (CL) and objective lens 1 (OL1) are implemented using another aspheric lens with a NA of 0.23 and a focal length f_{OL1} = 200*mm*. The magnification of the system given by the ratio of the focal lengths of OL2 and OL1 is therefore 0.3. The lenses are mounted on a two-rotation-axis gimbal lens mount. OL1 and CL mounts are placed on two linear stages crossed at 90*deg* to providing positioning flexibility in the yz-plane. The mounted OL2 is placed on a three-axis linear stage to facilitate alignment in all three directions. The expander lenses (ELs) are 0.5*in*-diameter mounted aspheric lenses with a focal length of 11*mm*. The mirrors M5 and M8 are also 0.5*in* in diameter and are placed along with the corresponding expander lens on a 1.5*in*-wide three-axis linear stage. The mounts for mirrors M1-M4, M6 and M7 contain positioning knobs to align the beams precisely in the xy-plane.

Custom-made mounts were designed to position the photomask and sample. The photomask mount is placed on a two-axis linear stage for alignment in the yz-plane, a platform with a pitch (rotation around the y-axis) and yaw (rotation around the z-axis) correction and a lab jack for translation along the x-direction. Similarly, the sample mount is placed on two linear stages stacked at 90*deg* to facilitate alignment in the yz-plane, a tilt/yaw correction platform and a lab jack for the x-translation. The actuator of the linear stage along the z-axis is a high-precision differential micrometer capable of submicron range adjustments, which are needed to position the sample at the focal plane precisely [72].

Not shown in Figure 5.1, is an initial HWP followed by an iris placed after M2 to control the overall intensity and the amount of light entering the system. Reduced intensity is necessary during alignment, for precision and safety. Additionally, the top beam is generated by splitting the central beam by means of a PBSC placed in between the final HWP and the expander lens mount. This PBSC directs the top beam upward which is then redirected along the z-direction by employing a mirror angled at 45*deg.* The final HWP can then be used to control the ratio of intensities between the central and top beam as described earlier. For clarity, the top beam is not represented in the following figures as well.

5.2 PIIL Alignment Procedure

The initial alignment procedure for PIIL [140] was improved upon, to establish a repeatable and precise alignment strategy for experimental demonstrations. The reported

alignment techniques can be applied to any multiple-off-axis beam imaging and/or interference systems [141].

The central beam in the PIIL exposure system represents the optical axis in the z-direction. The alignment of the same is crucial in the procedure as it is employed to align the subsequent components. Targets are printed out for the required beam configuration, attached to mounts, and are used at every step of the alignment by placing the mount flushed against reference blocks or screws to ensure alignment along the *y*-axis. First, mirrors M1 and M2 are positioned such that the central beam is redirected along the z-direction as depicted in Figure 5.2.

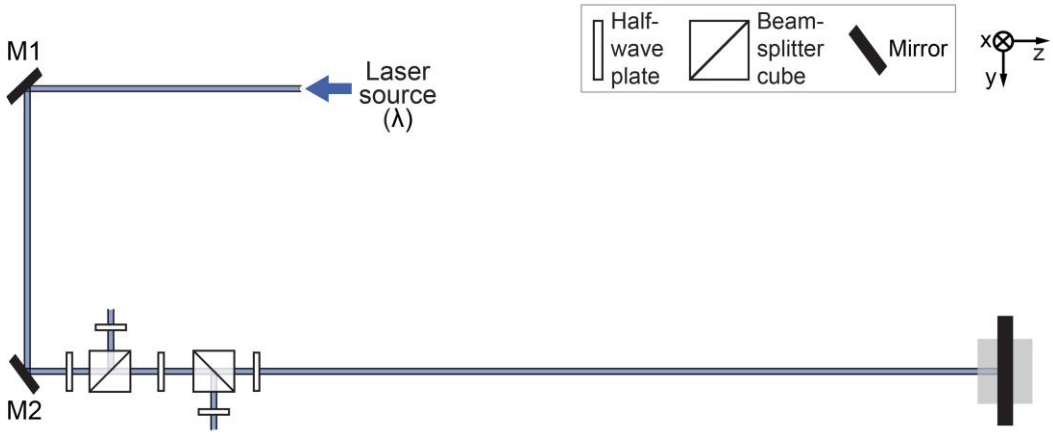

Figure 5.2 – Alignment of the HWPs and PBSCs using the central on-axis beam.

Keeping the target close to M2 and far away at the end of the optical table, the knobs in the mirror mounts are used to align precisely the central beam using the overcorrection technique depicted in Figure 5.3. Following this, the series of HWPs and PBSCs are placed in succession, by aligning the reflections produced by the elements with

the incident beams. If the beam exiting these elements is decentered, the overcorrection technique is once again employed to correct it.

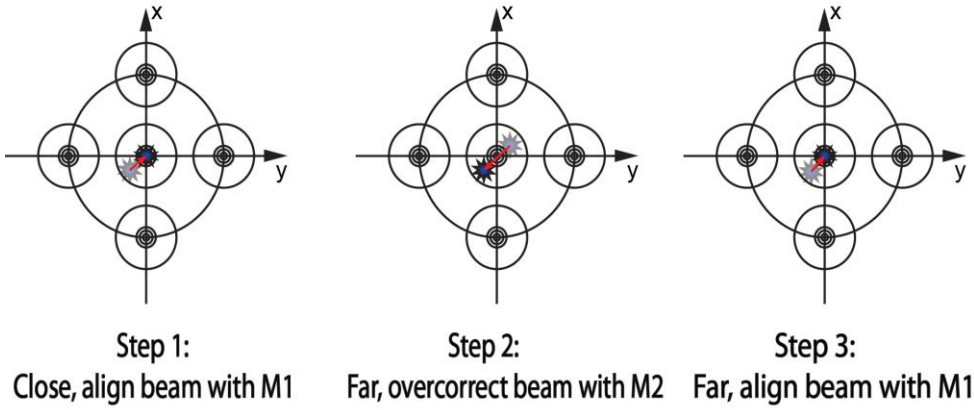

Figure 5.3 – Steps depicting beam alignment using the overcorrection technique.

The next steps involve directing the left and right side beam along the y-direction using mirrors M3, M4 and M6, M7 respectively. The beams are then redirected along the z-axis using mirrors M5 and M8 as shown in Figure 5.4. The beams are corrected for their alignment in the xz-plane and the xy-plane along the length of the table using the overcorrection technique in Figure 5.3. The expander lenses are fixed to their mounts and the expanded beams are aligned by adjusting the mounts along the x- and z-directions. The chief rays of the expanded beams, obtained by closing the iris, are used to align the beams correctly. This procedure is repeated until both the expanded and unexpanded beams are perfectly aligned.

The CL is aligned next by positioning the lens along the z-direction where, the expanded beams are collimated. The central beam alone is expanded for the purposes of alignment. Once positioned, the distance between the ELs and CL is $f_{EL} + f_{CL}$. OL1 is placed at a distance of $f_{OL1} + f_{CL}$ by ensuring that the unexpanded beams propagate parallel

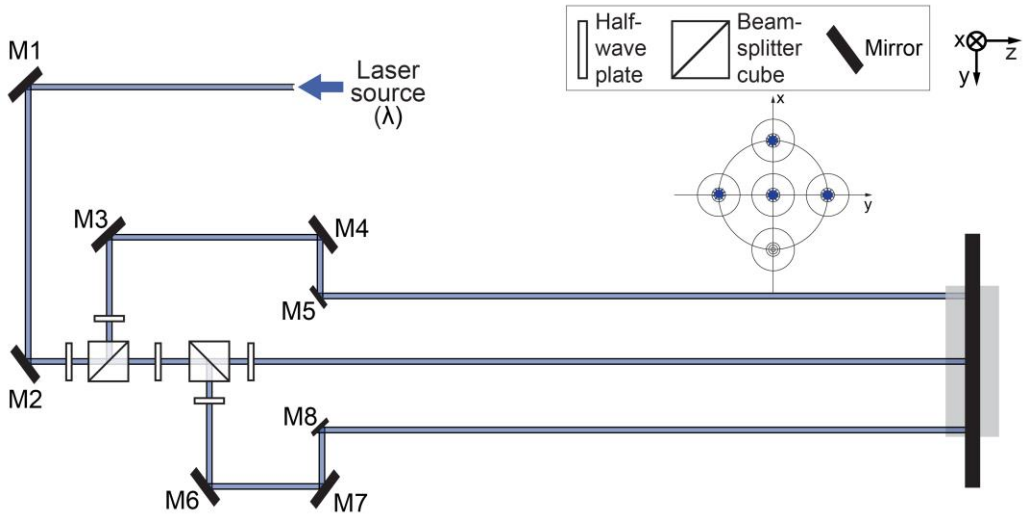

Figure 5.4 – Alignment of mirrors M3 to M8 to redirect the side beams along the z-direction. The inset show the beams on the target at this step.

to the z-axis. Similar to CL, OL1 is positioned along the z-axis such that the expanded beams are collimated after passing through it. At this point, the distance between OL1 and OL2 is $f_{OL1} + f_{OL2}$. The schematics of the lens positioning at various stages is depicted in Figure 5.5. The pitch, yaw and lateral displacement of the lenses along the y-axis are adjusted by aligning the incident beam with its reflections from the front and back faces of the lens as described in Figure 5.6Figure 5.6.

Following the alignment of OL1, the polarizations and intensities of the parallel beams are adjusted according to the beam configuration by using detectors, a Glan-Thompson polarizer and power meters. As described before, the HWPs before (after) the PBSCs are rotated to control the intensities (polarizations) of the beams.

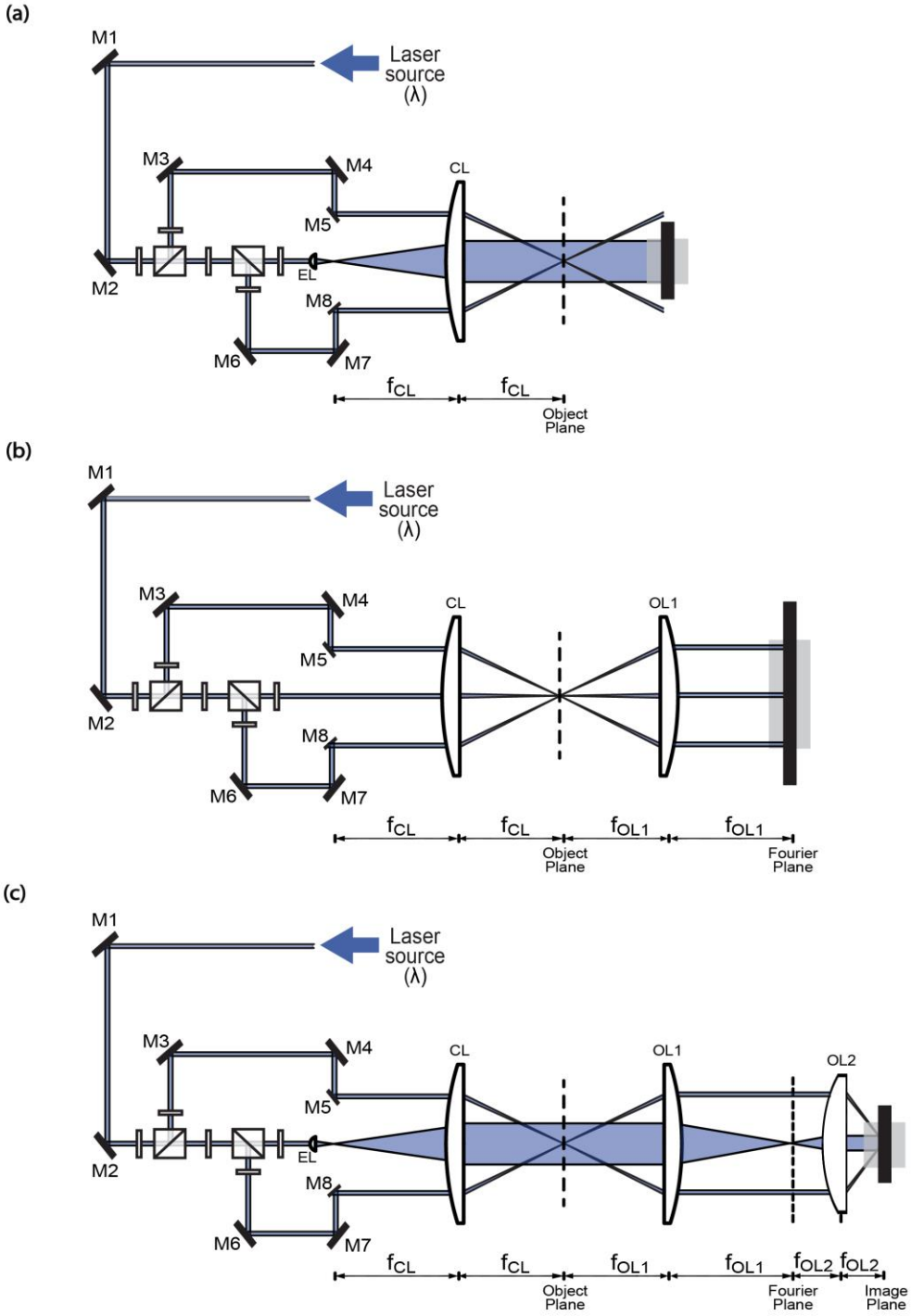

Figure 5.5 – Alignment of (a) CL, (b) OL1 and (c) OL2.

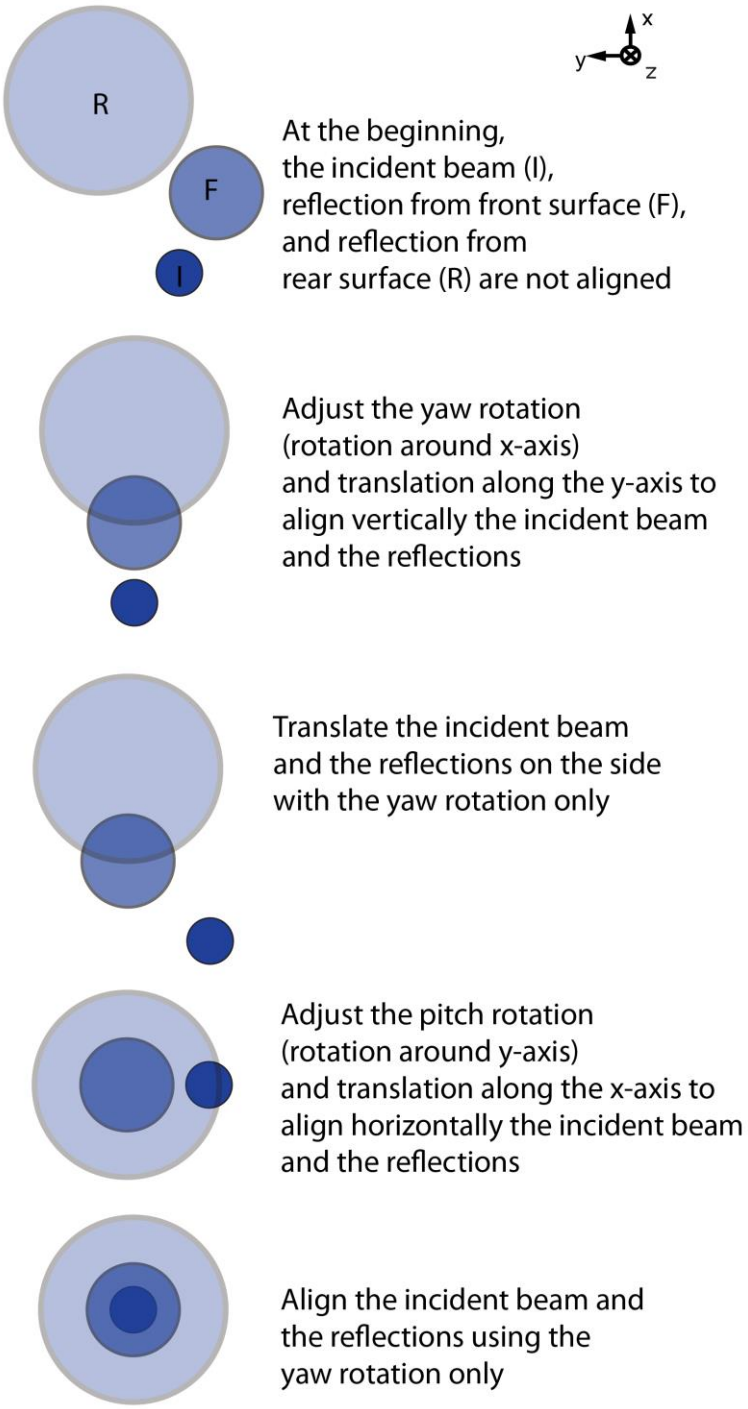

Figure 5.6 – Fine alignment of lenses using the reflections from the front and rear end faces.

Both the photomask and sample mount are added to the PIIL system using a similar technique. A piece of the photomask is used as a test sample for alignment of the sample mount. The pitch and yaw of the photomask (sample) mount are adjusted such that the beams and their reflections are evenly distributed around the optical axis upstream of the CL (OL2). The mounts are positioned along the z-axis such that the patterns are diffracted by all the beams simultaneously. This is done by observing the beams being diffracted by the same light-blocking element while translating the mount in the y-direction. This signifies that the photomask (sample) is at the object (image) plane.

5.3 Photomask Design

The photomask is a $4in$, chrome-on-glass photomask containing various elements depicted in Figure 5.7. It contains seven elements representing photonic crystal (PhC) elements and the Georgia Institute of Technology (GT) logo. The seven elements include a two waveguide couplers, a ring resonator, a $90deg$-bend waveguide, a straight waveguide, a PhC circuit and a passband filter. Except for the PhC circuit and the GT logo, every other element is represented by two designs, a single-period-blocking design with $3.35\mu m$ features and a double-period-blocking design with $6.7\mu m$ features [72].

A frame contains a pair of a single-period-blocking feature and a double-period-blocking element repeated 100 times in a 10×10 array. For each element, nine frames corresponding to nine different sizes ranging from 98% to 102% are included. Additionally, identification codes for the patterns (P1 through P8) and sizes (S1 through S9) are included for viewing under the microscope, and larger identification characters for

the unaided eye (1 through 8) are also incorporated into the photomask [72]. The details of the photomask are depicted in Figure 5.8.

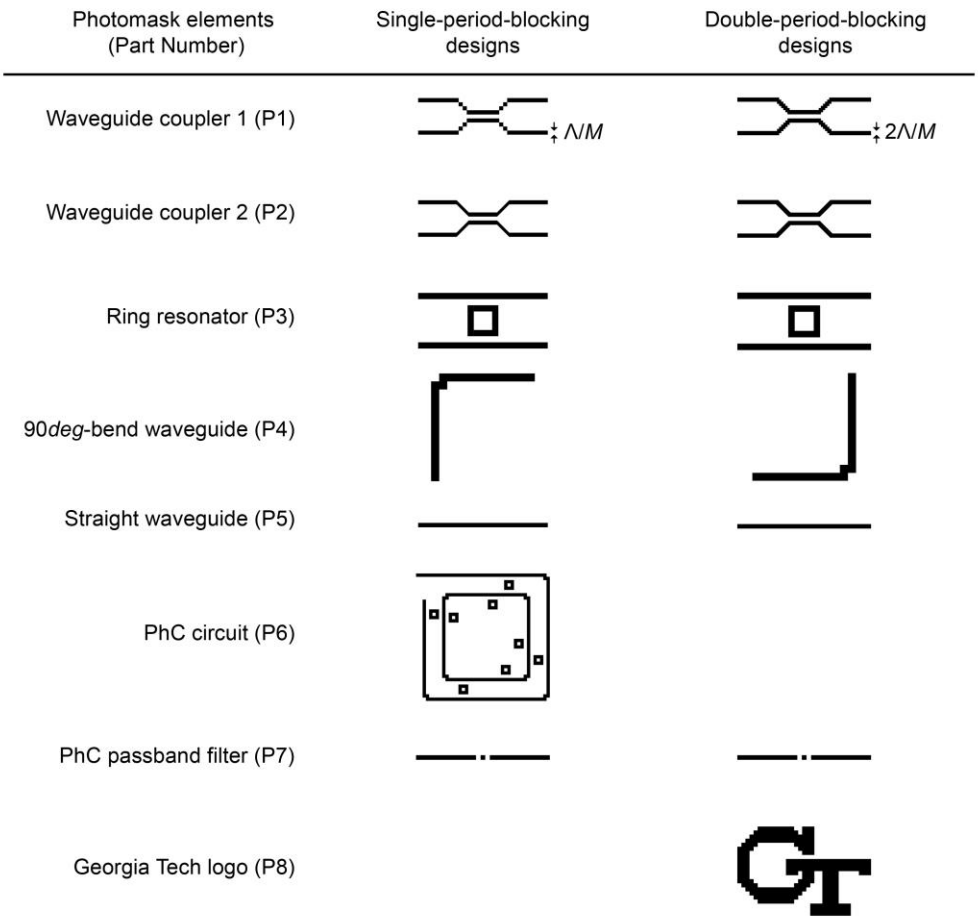

Figure 5.7 – Representations of the single- and double-period-blocking features in the photomask [72].

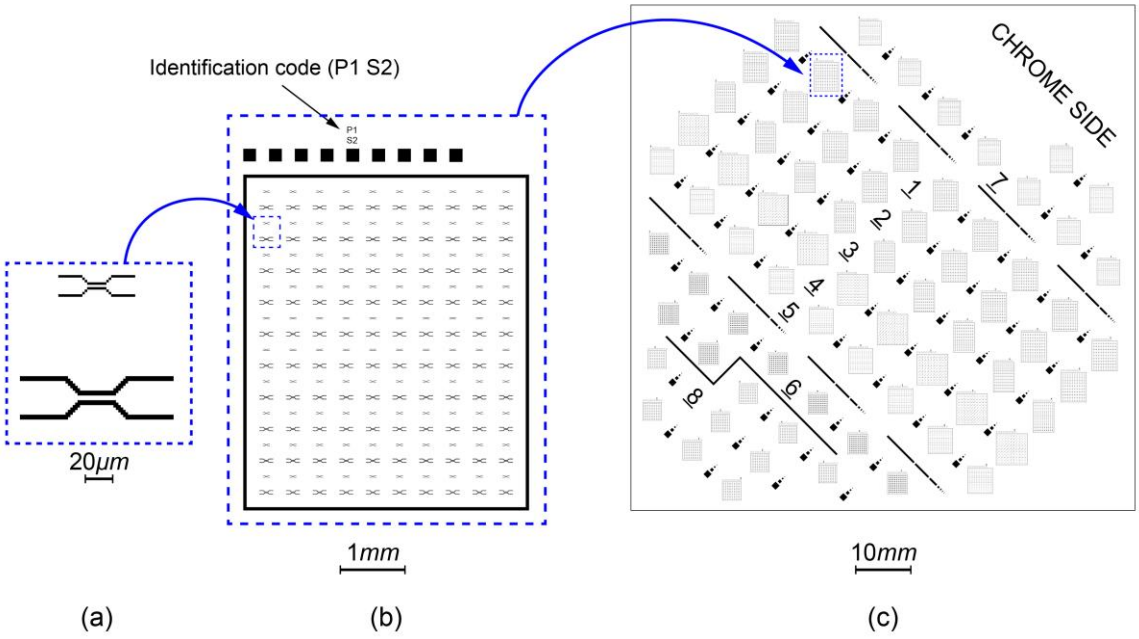

Figure 5.8 – (a) Single- and double-period-blocking photomask elements grouped as a pair. (b) Frame containing a 10 × 10 array of element pairs (c) Complete photomask containing 72 frames corresponding to the eight different photomask elements and their nine size scales [72].

5.4 3D PIIL Process

The samples to be exposed are prepared in the GT IEN Pettit cleanroom. The sample substrates are 1.25*inch*-square optical-grade fused quartz slides. Prior to every experiment, the slides are cleaned using an ultrasonic bath of acetone for 5*min*; rinsed with methanol, isopropanol, and deionized (DI) water; and finally dried for one hour on a hotplate at 200ºC to completely decompose the O-H bonds. This is necessary to promote adhesion between the photoresist and the glass substrate, as even trace amounts of water can lead to delamination of the photoresist during development. Once dry, the slides are spin coated with Microchem's SU-8 2015 negative-tone photoresist using a SCS G3P8 spin coater at 3000rpm for 30*sec*. The desired photoresist film thickness is 15μm before

exposure. The samples are then soft baked on a hotplate for 5*min*-10*min* at 65°C and 5*min*-10*min* at 95°C to remove the solvent in the photoresist.

Covered in aluminum foil to avoid exposure from ambient light, the samples are brought to the Optics Laboratory, where the prototype PIIES is installed. The output laser power is about 150*mW*. Various exposure times ranging from 0.3*sec* to 3.5*sec* were tried to determine the optimum exposure dose without the photomask. Once exposed, the photoresist is brought back to the cleanroom and hard baked for 1*min* at 65°C and 1*min* at 95°C. The hard bake catalyzes the crosslinking that occurs in the exposed regions of the photoresist. The two step baking process with an intermediate cooling step, where the sample is allowed to cool down naturally, is carried out in order to promote uniform heating and alleviate stress. The exposure spots can be seen to appear on the sample upon cooling. The sample is then developed in an agitation bath of Microchem's SU-8 developer for 2*min*-3*min*, rinsed with isopropanol, and dried with nitrogen. The developed sample is then evaluated using an optical microscope. For Scanning Electron Microscope (SEM) imaging, the sample is further coated with ~15*nm* of gold/palladium using a Hummer 6 gold sputterer.

5.5 Experimental Results

The (3+1)-beam umbrella configuration shown in Figure 5.9(a) was used to produce rhombohedral structures with an expected lattice period of $\Lambda_{xy} = 1.3\mu m$ in the xy-plane. The required lateral beam displacement, $d_{beam,}$ to achieve this periodicity is 17.78*mm*. According to the relationship described in Section 4.2.3, the beam angle θ_{beam}, is 18.829*deg*. The intensities of the three side beams labeled $\mathbf{k}_{2,}$ $\mathbf{k}_3$ and $\mathbf{k}_4$, are adjusted to

be one-third of that of the central beam labeled $\mathbf{k}_1$. SEM images of the PIIL-produced microstructures with an exposure time of 0.8*sec* and 0.9*sec* are shown in Figure 5.9 and Figure 5.10 respectively.

These experimental results demonstrate that a 3D pattern can be fabricated through PIIL in a single exposure step. The various rhombohedral layers along the thickness direction of the photoresist film are clearly visible in the results. However, as discussed in Chapter 4, significant optical aberrations and orientation errors were expected due to the use of non-optimized optics and manual alignment of the system. The lattice constant on the xy-plane differs when measured along various directions due to the non-uniform surface of the photoresist. The lack of uniformity can be attributed to the reflections that occur at the front and back faces of the numerous lenses. This causes certain regions to receive a higher exposure dose than the neighboring regions. The relative period error measured along different directions ranges from 0.1% to 9%. The angle measured between various lattice directions differ by a maximum of 6*deg*. The interference pattern in the fabricated structures are rotated by an angle of 30*deg* in the xy-plane in comparison to the simulated structures due to the refraction of the polarization vectors [142].

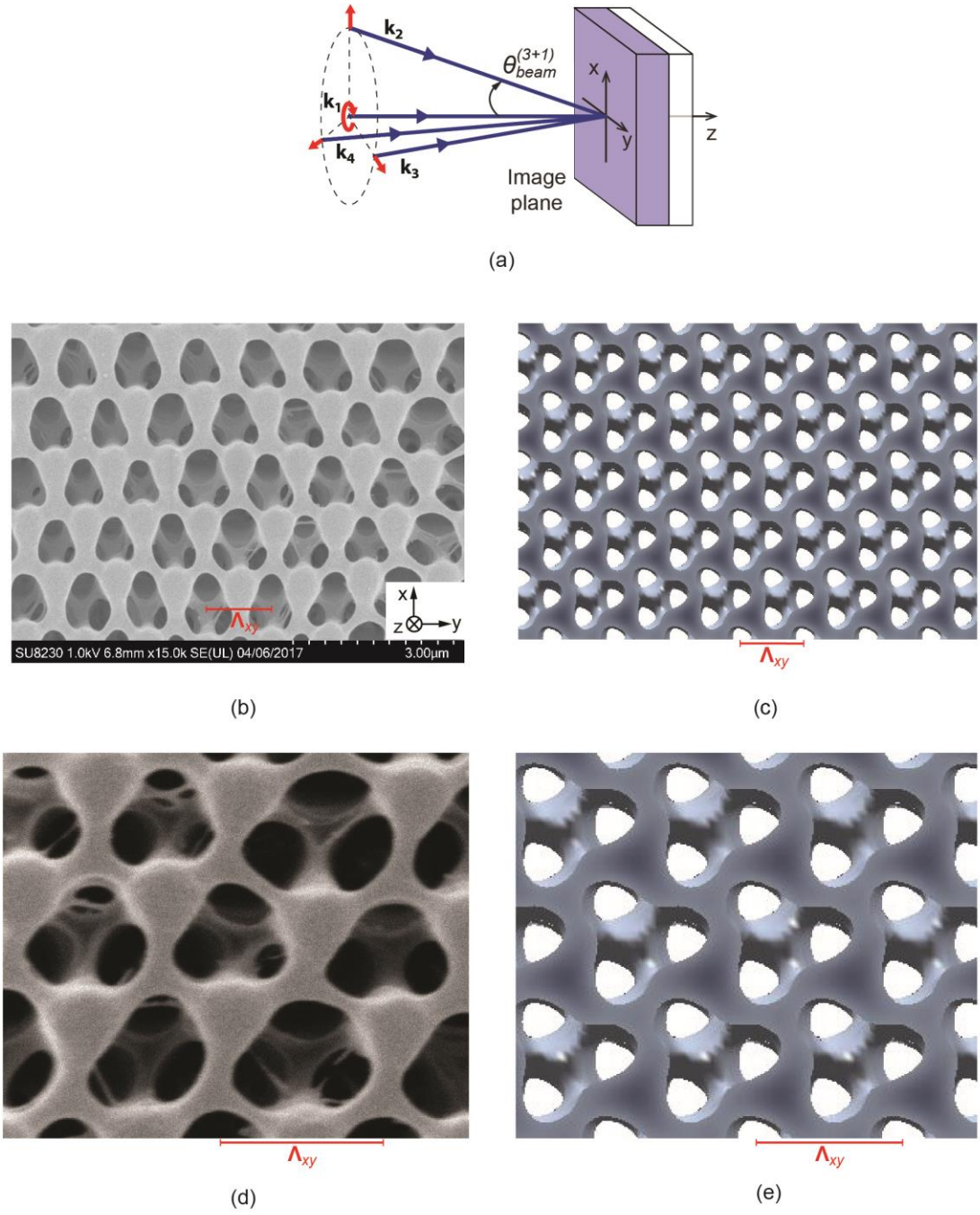

Figure 5.9 – (a) Beam configuration at the PIIES image plane for 3D rhombohedral lattice structures. (b), (d) Top-view SEM images of experimentally obtained results, along with their (c), (e) corresponding simulated structures obtained using the PIIL model.

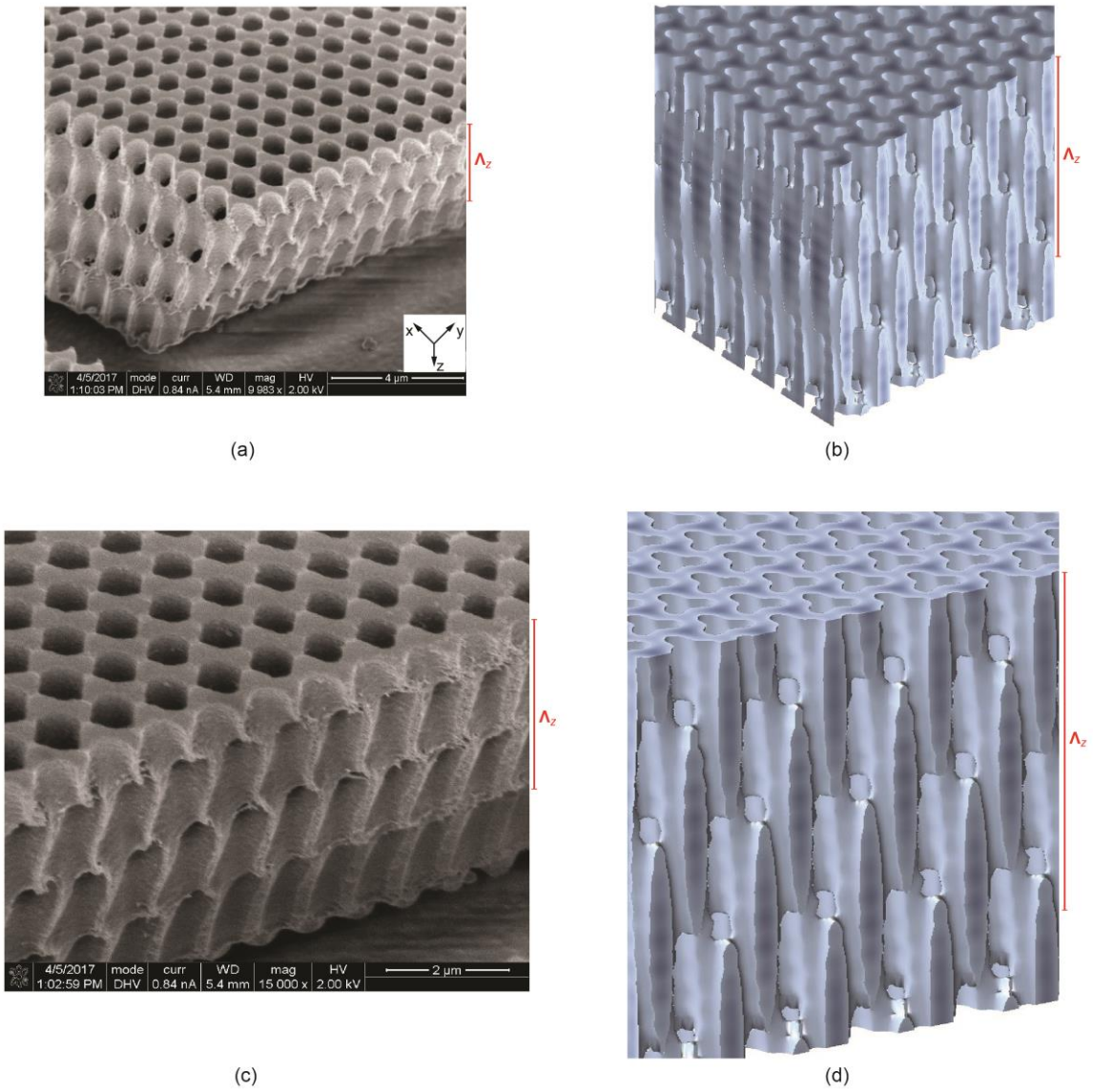

Figure 5.10 – (a), (c) 3D-view SEM images of experimentally obtained results for rhombohedral structures, along with their (b), (d) corresponding simulated structures obtained using the PIIL model.

The periodicity along the z-direction was measured to be about 8.5μm. This is lesser than the targeted/simulated periodicity of 11.5μm. The decrease in the periodicity is expected because the SU-8 film undergoes shrinkage during the post-exposure processes.

The total thickness of the film is reduced to $12\mu m$ from the $15\mu m$-thick film obtained by spin-coating, and as a result, the periodicity also shows a corresponding decrease. This 25% shrinkage is commonly observed in negative-toned photoresists leading to stress-associated lattice distortions along the lateral direction [142-144]. In spite of these distortions, the subsequent layers of the rhombohedral lattice are formed sufficiently with the expected periodicity throughout the thickness of the film. Also, the shrinkage almost compensates for the elongation of the structures along the z-direction inside the photoresist, caused by the refraction of the wavevectors. The corresponding periodicity of the structures in air is about $6.78\mu m$.

The above figures depict a bicontinuous lattice structure where the photoresist and void volumes are continuous within themselves throughout the structure. The filling fraction shown in these cases ranges from 30% to 50%. The exposure time to fabricate such bicontinuous structures are in the order of 0.7s to 0.9s. At higher exposure times, the uniformity of the photoresist film increases but the increased exposure dosage causes the pores to be completely filled. The filling fraction rises above 79% for the cases depicted in Figure 5.11. Also, it can be seen within the white outline in Figure 5.11(c) and (d) that the structure is not completely porous, as the air holes are not connected to each other. Circular motifs in the experimental results can be attributed to the fact that the holes on the surface try to minimize the amount of surface energy by expanding [142]. Thus, the patterns seem more rounded in these regions. At the bottom layers however, since the film is confined by the substrate, the patterns will be triangular in shape as shown in the simulations.

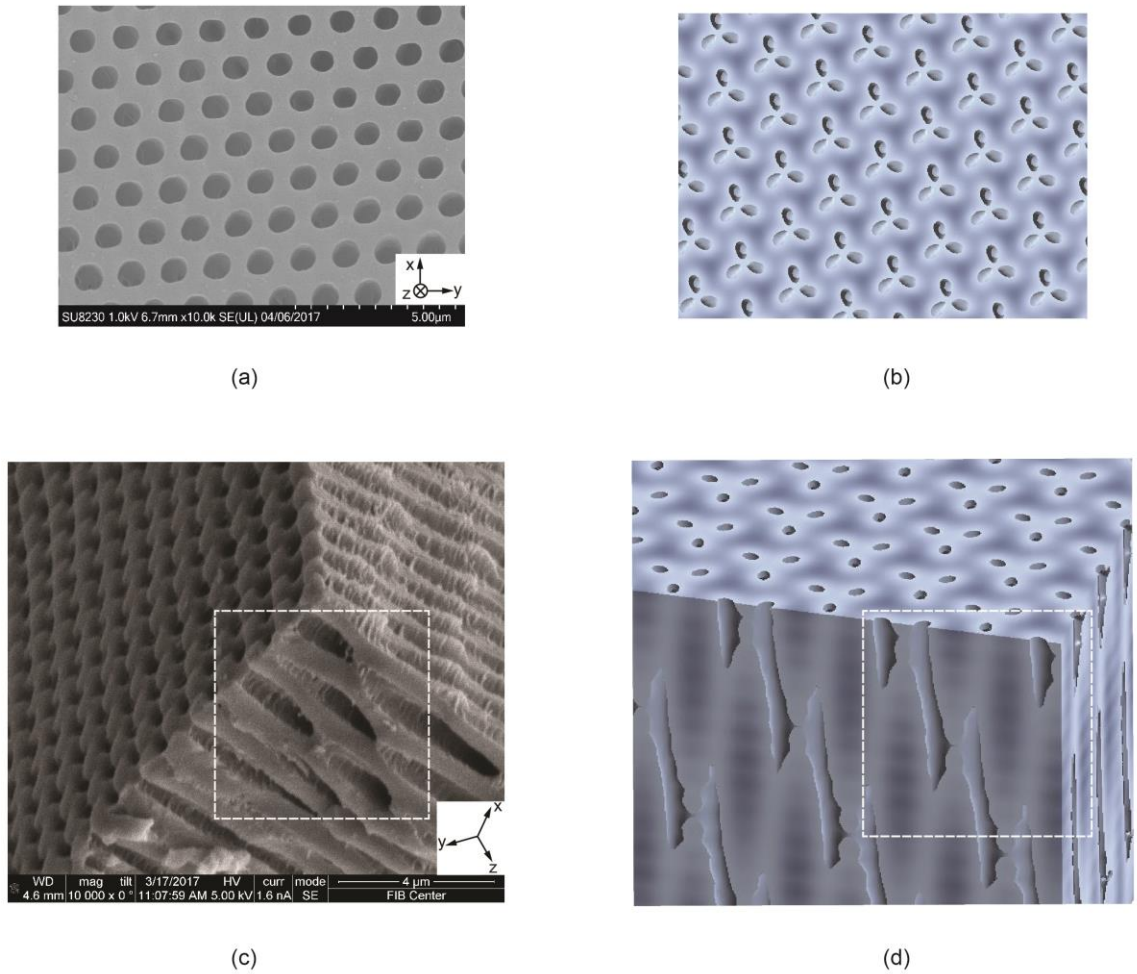

Figure 5.11 – (a) Top-View SEM image of over-exposed structures displaying closed pores and (b) its corresponding simulated structure. (c) 3D-view depicting pores that are not connected to each other and (d) its corresponding simulation equivalent structure.

5.6 Summary

The PIIL concept for 3D microstructures was demonstrated using the (3+1)-beam configuration. The 3D periodicity is clearly visible in the structures and is consistent with the simulation results. Errors in periodicity and orientation occur due to non-ideal exposure conditions as explained in Chapter 4. In spite of the alignment errors and spherical aberrations however, the subsequent layers form satisfactorily beneath the surface thereby

forming a 3D interconnected network. The dependence of the volume fraction on the exposure dosage, specifically the exposure time, is evident from the experimental results. Increase in the exposure time leads to non-porous structures that are not bicontinuous. Finally, these results demonstrate the validity of the PIIL concept for fabricating structures with 3D periodicity, as well as the completeness of the PIIL vector model as a tool to simulate PIIL exposures.

CHAPTER 6. CONCLUSIONS AND FUTURE WORK

In this chapter, the research on bicontinuous structures and Pattern-Integrated Interference Lithography (PIIL) is summarized, and future research objectives are described and discussed.

6.1 Conclusions

6.1.1 Multi-Beam Interference Bicontinuous Structures

The innumerable applications of periodic structures with a bicontinuously interconnected network calls for the fabrication and characterization of such bicontinuous structures. Multi-Beam Interference Lithography (MBIL) has been shown to possess the required flexibility and rapidity to construct even complex structures with varying degrees of bicontinuity. The ability of MBIL to control the interconnectedness in the structures precisely by means of varying the exposure dosage affords several advantages over self-assembly and construction-based approaches. Moreover, by configuring the beam parameters, it is possible to generate structures containing various symmetry elements. The characterization of Multi-Beam Interference (MBI) structures is typically carried out through imaging techniques that do not provide the required information in terms of the physical attributes of the structures such as the volumes and surface areas. In addition, it is important to ascertain the range of exposure doses that result in the structures being bicontinuous, in order to produce stable, self-supporting periodic networks.

In this work, the various types of interconnectedness that arise in periodic structures were identified and classified for periodic structures. The conditions for any unit cell to be bicontinuous were put forth and were used as suitable tests to check for bicontinuity in the

analyzed structures. The rhombohedral and woodpile lattice structures were investigated for their bicontinuity due to their ability to produce cubic structures as limiting cases. The Simple Cubic (SC), Face-Centered Cubic (FCC), Body-Centered Cubic (BCC) and Diamond Cubic (DC) structures were generated by controlling the angle between the central and side beams in an umbrella configuration. Each of the cases was compared to its sphere-at-each-lattice-site model equivalent structure, whose state of bicontinuity depends on the radius of the spheres. The bicontinuity ranges, volumes and surface areas for each of the limiting case MBI-structures were determined and represented as a function of the normalized intensity threshold. The structures were investigated for various incident polarizations in air as well as in photoresist. The effects of index-matching were also included and tested for the structures in photoresist. It was observed that the bicontinuity ranges and volumes are independent of the beam parameters for both the rhombohedral and woodpile lattices for the interference between azimuthally polarized beams. In the case of radial polarization, a change in the beam angle, alters the amount of interference that occurs between the beams, and hence affects the resulting volume fractions and the bicontinuous ranges. The normalized surface area always depends on the beam angle, irrespective of the nature of polarization of the beams or the medium in which the structures are formed. Realistic lithographic conditions were modeled to study the consequences of refraction and absorption effects that occur within the volume of the photoresist, and the resultant structures displayed effects that were dissimilar to the structures that were generated in air. The range of lithographic models and materials that could apply to this method of bicontinuity analysis were identified and enumerated.

6.1.2 Three-Dimensional Pattern-Integrated Interference Lithography

Addressing the limitations of MBIL, Pattern-Integrated Interference Lithography (PIIL) has been put forth as an efficient technique to pattern two-dimensional (2D) and three-dimensional (3D) lattice-based microstructures with functional elements embedded within them [82, 83, 133]. Extensive research to understand and quantify the capabilities and limitations of the PIIL system has resulted in a comprehensive PIIL simulation model [72, 82, 83], an improved photomask design [84] and a detailed analysis of the exposure system using ZEMAX [72]. An 8*f* confocal system was devised to implement PIIL and demonstrate PIIL experimentally [140]. 2D photonic crystal waveguide structures produced by PIIL were modeled and compared to their idealized equivalent structures [8, 139].

Initial experimental work on 3D microstructures by PIIL was carried out and rhombohedral structures were fabricated with various exposure doses. In spite of the manual alignment and non-optimized optics of the PIIL system, 3D structures with the desired periodicity were fabricated and compared to the simulation results obtained using the PIIL vector model. The experimental results showed good qualitative agreement with the simulation model that accounted for the optical aberrations. Small errors in periodicity result from the non-uniformities in the photoresist film, as a result of the non-ideal exposure conditions. However, this can be corrected by using custom-made lenses that are suitable for the experimental wavelength.

6.2 Future Work

6.2.1 Experimental Validity of Bicontinuity Analysis

The bicontinuity results obtained through simulations for the rhombohedral and woodpile structures produced by MBI in SU-8 photoresist need to be validated through

experimental techniques. As outlined in Section 1.4, techniques such as laser scanning confocal microscopy [86] and freeze fracture electron microscopy [87] have been used to determine if the structures are bicontinuous. The porosity in the structures has been determined using gravimetric analysis [58, 62] or through adsorption techniques [47]. The filling fraction of the constituent materials in the MBI structures can be verified through optical characterization techniques. The transmission or reflective spectra of the structures can be analyzed experimentally, and compared to simulation results obtained through analytical or Finite Difference Time Domain (FDTD) modeling [60, 91, 95]. Since the optical characteristics depend on the refractive index of the constituent materials, the effective refractive index can be computed for each layer, which depends on the filling fraction, which can then be used to compute the transmission spectra [60, 145]. This will present a more definitive assessment of the uniformity inside the photoresist. In addition, suitable materials can be deposited onto the photoresist templates, and with imaging, a correlation can be devised between the amounts of material deposited to the filling fraction of the polymer. Future research can also explore the choice of responsive materials, and loading them with sensing particles to determine the volumes and surface areas of the structures [56]. The response can be to a photo-induced change in absorption, refractive index, pH, temperature, electrical conductivity, etc.

The intensity threshold of a photoresist depends upon the resist's sensitivity, but also on the processing conditions like the baking temperatures, baking times, development times and the developer solvent. A future research objective can be to derive a correlation between the experimental exposure dosage and the normalized intensity threshold in the

simulation model for the MBIL and PIIL structures. This would enable a more direct method of fabricating periodic structures with the desired level of bicontinuity.

6.2.2 3D PIIL Photoresist Improvement

The shrinkage and adhesion issues that are typically seen during the use of a negative-tone photoresist can be avoided by using a positive photoresist. Also, negative photoresists suffer from distortions that arise from the swelling of the photoresist during development [60]. Chemically amplified positive-tone photoresists demonstrate lower absorption and increased sensitivity thereby, decreasing the exposure time that is required [146]. Alternatively, negative photoresists with a lesser absorption coefficient can also be used instead.

The contrast observed in the 3D PIIL structures can be improved by adding a base, Triethylamine (TEA) to cancel the background intensities that contribute to the final interference pattern. These background intensities occur due to the interference between unwanted polarizations in the beams. This gives rise to a non-zero minimum intensity that reduces the contrast in the resulting structures [147-151]. Also, the contrast can also be improved by altering the processing conditions including optimization of the pre-bake times and temperatures, post-bake times and temperatures, exposure times, development times, development solvents, etc. The adhesion issues between the polymer and substrate can be addressed by the use of adhesion promoters [152-155]. The disintegration of the structures during the development process that involves, developing the structure, rinsing and drying, can be improved by employing techniques like super critical drying [156, 157] or rinsing with a solvent that has lower capillary force than isopropanol [158, 159].

6.2.3 Improved PIIL Implementation

The PIIL system is prone to errors due to manual alignment. As described in Chapter 4, the maximum acceptable decentering error is $25\mu m$, and tilting error is $5mdeg$. Beyond these tight specifications, the imaging performance capability of the exposure system deteriorates significantly. Even with improved alignment practices [141], there exists a ±2% error on the interference period and $\pm 1deg$ error on the fringe orientation due to the manual nature of the alignment process. To minimize this, a new system with automated alignment can be devised that employs the use of piezo-electric micropositioners, and charge-coupled devices to provide feedback to the system to precisely align the multiple beams. Additionally, custom-made high-numerical aperture lenses can be designed for the experimental wavelength of $363.8nm$ to optimize the exposure system and minimize the optical aberrations. Another future research objective would be to engineer a photomask that corrects for the distortions observed in the lattice. 3D volume photomasks also offer the possibilities of integrating functional elements at different image planes within the photoresist, thereby increasing the versatility of PIIL.

6.2.4 Multiple-Optical-Axis Pattern-Integrated Interference Exposure System

A Multiple-Optical-Axis (MOA) Pattern-Integrated Interference Exposure System (PIIES) offers the possibility of larger angles of incidence resulting in smaller lattice constants. In such a MOA system, the objective lenses and photomasks need to be titled in order to focus the mask elements at the image plane without keystone distortions. The MOA PIIES can be implemented using a single objective lens or double objective lens configuration, similar to the single-optical-axis PIIL. In addition, each set of optical elements can be the same or different for each axis, thereby increasing the possibilities of

custom-modified patterns. A variation of MOA system without using mirrors has also been conceptualized and is depicted in Figure 6.1. The modeling of this system has been done using a combination of ray tracing and Fourier analysis [160, 161]. However, further research in the system design in terms of prototyping, and experimental demonstration are still needed.

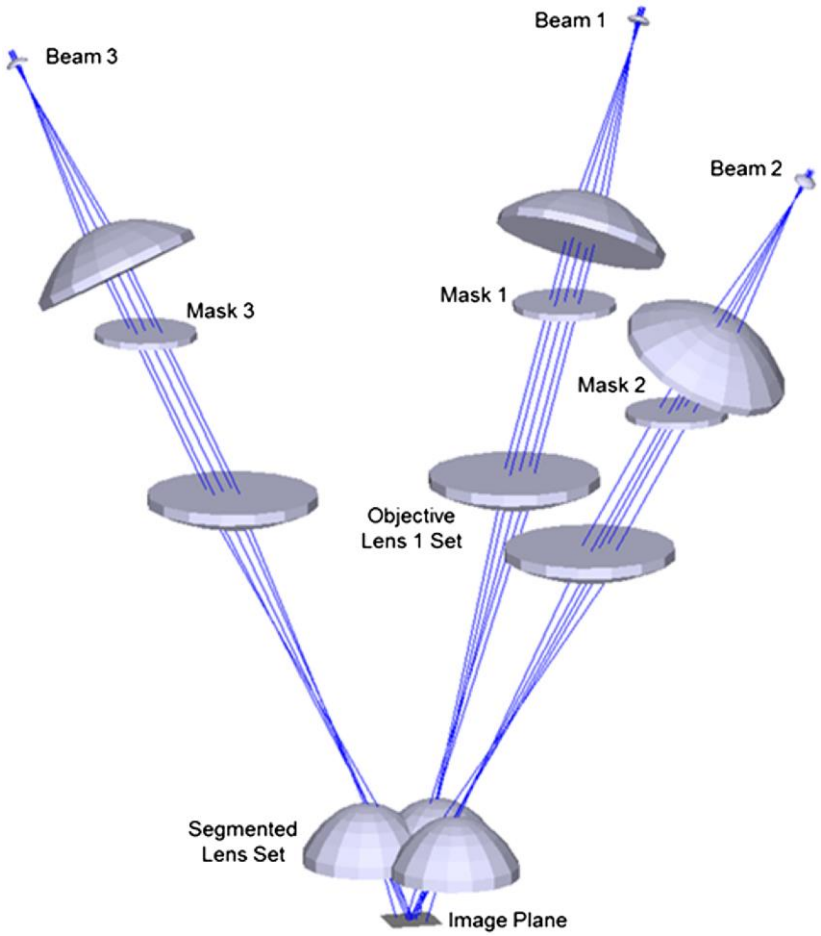

Figure 6.1 – Concept diagram of a MOA-PIIES configuration [160]

6.3 Concluding Remarks

The research in this thesis provides insight into the physical characteristics of typical periodic structures formed by MBIL as a function of the intensity threshold. The property of bicontinuity is quantified and investigated under various lithographic conditions. In addition, the novel technique of PIIL has been demonstrated experimentally for 3D lattice-based-periodic microstructures. Although significant research has been done in the field of PIIL, there are still numerous avenues that can be explored to increase the capabilities of this unique technique.

APPENDIX A. MATLAB SCRIPTS: MULTI-BEAM INTERFERENCE

This appendix contains the MATLAB script for generating the Multi-Beam Interference (MBI) structures in air and photoresist (SU-8) as a uniform medium. It also contains the MATLAB script for MBI structures in SU-8 as a stack of thin films, accounting for the refraction and reflection effects that can be seen within the photoresist.

A.1 Multi-Beam Interference Structures in Uniform Media

```
%% Initialization
clc
clear all
lambda = 363.8e-9;      % wavelength of the source
pitch =  668.4e-9       % Period of the interference pattern
NA_im = 1;              % Numerical Aperture on the image side
magn = 1;               % Magnification

%% Setting the resolution
N_pitch = 21;           % # of pixels for 1 period should be odd
N = 10*N_pitch+1;       % # of periods should be odd
pixel_resolution = pitch/N_pitch;
image_size = N*pixel_resolution;
image_axis = -image_size/2:image_size/(N-1):image_size/2;

%% Photoresist Characteristics
PR_depth    = 1e-6;
layer_number = 21;
range_depth = linspace(0,PR_depth,layer_number);
n_PR = 1.67             % Refractive index of photoresist
lambda = lambda/n_PR    % In case of photoresist

%% Beam conditioning

% Rhombohedral lattice
phi       = [0 180 -60 60 0];       % Azimuthal angles of the beams
theta_im  =   asind(2*lambda/(sqrt(3)*pitch));  % Beam angle at image
plane
theta_im = [0 theta_im]
theta_pol = [1/sqrt(2) 1*1i/sqrt(2) 0 1 sqrt(3)/2 +0.5  sqrt(3)/2 -0.5
0 0];                               % Polarization of the beams

% Woodpile lattice
phi = [0 -180 90 0 -90];            % Azimuthal angles of the beams
```

```
theta_im  =  asind(lambda/(pitch));       % Beam angle at image plane
theta_im = [0 theta_im]
theta_pol = [1 1i 1 0 0 -1 -1 0 0 1];     % Polarization of the beams

%% Interfernce Calculation
I = zeros(N,N,layer_number);              % 3D matrix of illumination
initialized to zero
Etotal=zeros(N,N,3);                      % Total electric field for
each layer
k1 = 2*pi/lambda * [sind(theta_im(1))*cosd(phi(1)) % Wavevectors of
sind(theta_im(1))*sind(phi(1)) cosd(theta_im(1))]; % each beam
k2 = 2*pi/lambda * [sind(theta_im(2))*cosd(phi(2))
sind(theta_im(2))*sind(phi(2)) cosd(theta_im(2))];
k3 = 2*pi/lambda * [sind(theta_im(2))*cosd(phi(3))
sind(theta_im(2))*sind(phi(3)) cosd(theta_im(2))];
k4 = 2*pi/lambda * [sind(theta_im(2))*cosd(phi(4))
sind(theta_im(2))*sind(phi(4)) cosd(theta_im(2))];
k5 = 2*pi/lambda * [sind(theta_im(2))*cosd(phi(5))
sind(theta_im(2))*sind(phi(5)) cosd(theta_im(2))];
r =[];                                                % Position vector
fx_vect = image_axis;
fy_vect = fx_vect;
z_vect = range_depth;

for i=1:layer_number          % Calculating intensity for each layer
    for m = 1:N
        for n = 1:N
            r = [fx_vect(m) fy_vect(n) z_vect(i)];
            E1_r = exp(-1i*(dot(k1,r)))*[theta_pol(1) theta_pol(2) 0];
            E2_r = exp(-1i*(dot(k2,r)))*[theta_pol(3) theta_pol(4)
sind(theta_im(2)+90)]; % In case of azimuthal polarization, z pol= 0
            E3_r = exp(-1i*(dot(k3,r)))*[theta_pol(5) theta_pol(6)
sind(theta_im(2)+90)]; % In case of azimuthal polarization, z pol= 0
            E4_r = exp(-1i*(dot(k4,r)))*[theta_pol(7) theta_pol(8)
sind(theta_im(2)+90)]; % In case of azimuthal polarization, z pol= 0
            E5_r = exp(-1i*(dot(k5,r)))*[theta_pol(9) theta_pol(10)
sind(theta_im(2)+90)]; % In case of azimuthal polarization, z pol= 0
            Etotal = E1_r + E2_r + E3_r + E4_r; + E5_r;
            I(m,n,i) = 0.5* real(Etotal(1).*conj(Etotal(1)))...
                + 0.5* real(Etotal(2).*conj(Etotal(2)))...
                + 0.5* real(Etotal(3).*conj(Etotal(3)));

        end
    end
end

%% Applying intensity threshold
I_final = [];
format long;
norm_thresh = 0.4;            % Normalized intensity threshold
thresh =
norm_thresh*max(max(max(I(1:2*N_pitch,1:2*N_pitch,1:layer_number))))
disp(strcat('Filling Factor = ',
num2str(sum(sum(sum(I>thresh)))/(N*N*size(range_depth,2))*100),'%'))
for i=1:size(I,3);            % Selecting points only above threshold
    I_final = cat(3, I_final, I(:,:,i)>thresh);
```

```
end

%%  Display Structure
figure
bound = 2;                      % Number of periods to display
range_image_row = (N+1)/2+1-
round((bound+0.5)*N_pitch*sqrt(3)/2):(N+1)/2+round((bound+0.5)*N_pitch*
sqrt(3)/2);
range_image_col = (N+1)/2+1-
round(bound*N_pitch):(N+1)/2+round(bound*N_pitch);
isosurface(image_axis(range_image_row)*1e6,image_axis(range_image_col)*
1e6,(range_depth)*1e6,I(range_image_col,range_image_row,:),thresh);
isocaps
(image_axis(range_image_row)*1e6,image_axis(range_image_col)*1e6,(range
_depth)*1e6,I(range_image_col,range_image_row,:),thresh,'above');
axis equal
colorbar
xlabel('x (\mum)');ylabel('y (\mum)');zlabel('z (\mum)')
set(gca,'ZDir','reverse')
viewAngEl = 17;
viewAngRot = 55;
view(viewAngRot, viewAngEl)
load blue_colormap a
colormap(a)
axis on;
set (gcf,'Color',[1 1 1])
end
```

A.2 Multi-Beam Interference Structures in Non-Uniform Medium

```
%% Initialization
clc
clear all
lambda = 363.8e-9;      % wavelength of the source
pitch =  668.4e-9       % Period of the interference pattern
NA_im = 1;              % Numerical Aperture on the image side
magn = 1;               % Magnification

%% Setting the resolution
N_pitch = 21;           % # of pixels for 1 period should be odd
N = 10*N_pitch+1;       % # of periods should be odd
pixel_resolution = pitch/N_pitch;
image_size = N*pixel_resolution;
image_axis = -image_size/2:image_size/(N-1):image_size/2;

%% Photoresist Characteristics
PR_depth    = 1e-6;
layer_number = 21;
range_depth = linspace(0,PR_depth,layer_number);
A = 1.07;  B = 0.31;  C = 0.015; n_PR = 1.67; k_PR=6e-5; n_sub = 1.47;
n_BARC = 1.47; BARC_depth = 0;

%% Beam conditioning
```

```
% Rhombohedral lattice
phi       = [0 180 -60 60 0];       % Azimuthal angles of the beams
theta_im  =   asind(2*lambda/(sqrt(3)*pitch));  % Beam angle at image
plane
theta_im = [0 theta_im]
theta_pol = [1/sqrt(2) 1*1i/sqrt(2) 0 1 sqrt(3)/2 +0.5  sqrt(3)/2 -0.5
0 0];                                % Polarization of the beams

% Woodpile lattice
phi = [0 -180 90 0 -90];             % Azimuthal angles of the beams
theta_im  =  asind(lambda/(pitch));       % Beam angle at image plane
theta_im = [0 theta_im]
theta_pol = [1 1i 1 0 0 -1 -1 0 0 1];     % Polarization of the beams

mask=ones(N);
source_shift=round(1.0001*sind(theta_im(2))*image_size/lambda*...
    [[cosd(phi(2)) sind(phi(2))];...
    [cosd(phi(3)) sind(phi(3))];...
    [cosd(phi(4)) sind(phi(4))];...
    [cosd(phi(5)) sind(phi(5))]]);

%% Off-axis propagation of beams
M_mask=fftshift(fft2((mask)));
M1=M_mask;
M2=circshift(M1,[source_shift(1,1) source_shift(1,2)]);
M3=circshift(M1,[source_shift(2,1) source_shift(2,2)]);
M4=circshift(M1,[source_shift(3,1) source_shift(3,2)]);
val = max(max(max(M_mask)))-1;
M1 =  M1(:,:)>val;
M2 = M2(:,:)>val;
M3 = M3(:,:)>val;
M4 =  M4(:,:)>val;

%% Interfernce Calculation
I = zeros(N,N,layer_number); % 3D matrix of illumination initialized to
zero
for i = 1:layer_number;
    z=range_depth(i);
    disp('---------------------------------')
    disp(strcat('Processing photoresist layer >',
num2str(round(z/PR_depth*100)),'%'))
    c=clock;
    I1=zeros(N);
    E0=zeros(N,N); E1=zeros(N,N,3); E2=zeros(N,N,3); E3=zeros(N,N,3);
E4=zeros(N,N,3); E5=zeros(N,N,3);
    Etotal=zeros(N,N,3);
    P1 = zeros(N,N,3); P2 = zeros(N,N,3); P3 = zeros(N,N,3); P4 =
zeros(N,N,3); P5 = zeros(N,N,3);

    N_air=1;
    N_PR = n_PR-1i*k_PR;
    N_barc = n_BARC;
    N_sub = n_sub;                   % Fuzed quartz

    d1 = PR_depth/lambda;
    d_barc = BARC_depth/lambda;
```

```
    depth = z/lambda;
    defocus = defocus/lambda;

    fx_vect = -N/(image_size*2):N/(image_size*(N-1)):N/(image_size*2);
    fy_vect = fx_vect;
    y_vect = fy_vect/(NA_im/lambda);
    x_vect = fx_vect/(NA_im/lambda);
    [Y_vect,X_vect] = meshgrid(y_vect,x_vect);
    Pupil = sqrt(Y_vect.^2+X_vect.^2)<=1;
    [row,col] = find(Pupil);

    flag_txt=0;
    for m=min(col):max(col)
        for n=min(col):max(col)

            % Define the coordinates in the Fourier plane
            fx = -N/(image_size*2)+(m-1)*N/(image_size*(N-1));
            fy = -N/(image_size*2)+(n-1)*N/(image_size*(N-1));

            % If the pixel is inside of the system pupil, defined by
the diameter CA, the obliquity function is computed. The obliquity is 0
otherwise.
            if sqrt(fx^2+fy^2)<=NA_im/lambda;
                x = fx/(NA_im/lambda);
                y = fy/(NA_im/lambda);

                A=atan2(y,x); % azimuthal angle relative to the x-axis
                theta_i=asin(sqrt(x^2+y^2)*NA_im);

                alpha = sin(theta_i)*cos(A);
                beta  = sin(theta_i)*sin(A);
                gamma = cos(theta_i);

                gamma_layer  = sqrt(1-sin(acos(gamma))^2/N_PR^2);
                gamma_sub    = sqrt(1-sin(acos(gamma))^2/N_sub^2);
                gamma_barc   = sqrt(1-sin(acos(gamma))^2/N_barc^2);

                phi_layer = 2*pi()*(d1-depth)*N_PR*gamma_layer;  %

                % Tilted optical admittances eta and phase delta
                eta_1_S = N_PR*gamma_layer;      eta_1_P =
N_PR/gamma_layer;
                eta_sub_S = N_sub*gamma_sub;     eta_sub_P =
N_sub/gamma_sub;
                eta_barc_S = N_barc*gamma_barc;  eta_barc_P =
N_barc/gamma_barc;
                eta_air_S = N_air*gamma;         eta_air_P =
N_air/gamma;

                delta_1 = 2*pi()*(N_PR*gamma_layer*d1);
                delta_barc = 2*pi()*(N_barc*gamma_barc*d_barc);

                % B and C parameters
```

```
                M_S = [cos(delta_1) 1i*sin(delta_1)/eta_1_S;
1i*eta_1_S*sin(delta_1) cos(delta_1)]; % Matrix defined for each film
and polarization
                M_P = [cos(delta_1) 1i*sin(delta_1)/eta_1_P;
1i*eta_1_P*sin(delta_1) cos(delta_1)];

                M_barc_S = [cos(delta_barc)
1i*sin(delta_barc)/eta_barc_S; 1i*eta_barc_S*sin(delta_barc)
cos(delta_barc)]; % Matrix defined for each film and polarization
                M_barc_P = [cos(delta_barc)
1i*sin(delta_barc)/eta_barc_P; 1i*eta_barc_P*sin(delta_barc)
cos(delta_barc)];

                M_sub_S=eye(2,2); M_sub_P=eye(2,2);

                temp = M_S * M_barc_S * [1;eta_sub_S]; B_S = temp(1);
C_S = temp(2);
                temp = M_P * M_barc_P * [1;eta_sub_P]; B_P = temp(1);
C_P = temp(2);

                temp = M_barc_S * [1;eta_sub_S]; B_sub_S = temp(1);
C_sub_S = temp(2);
                temp = M_barc_P * [1;eta_sub_P]; B_sub_P = temp(1);
C_sub_P = temp(2);

                % Transmission and reflection coefficients
                tau_S_fraction = (2*eta_air_S / (B_S*eta_air_S + C_S))
/ (2*eta_1_S / (B_sub_S*eta_1_S + C_sub_S));
                tau_P_fraction = (2*eta_air_P / (B_P*eta_air_P + C_P))
/ (2*eta_1_P / (B_sub_P*eta_1_P + C_sub_P));

                r_II_S = (B_sub_S*eta_1_S - C_sub_S) / (B_sub_S*eta_1_S
+ C_sub_S);
                r_II_P = (B_sub_P*eta_1_P - C_sub_P) / (B_sub_P*eta_1_P
+ C_sub_P);

                % Film function matrix M
                F_S  = tau_S_fraction * ( exp(1i*phi_layer) +
r_II_S*exp(-1i*phi_layer));
                F_P  = tau_P_fraction * ( exp(1i*phi_layer) +
r_II_P*exp(-1i*phi_layer));
                F_zP = N_air*gamma/(N_PR*gamma_layer) * tau_P_fraction
* ( exp(1i*phi_layer) -r_II_P * exp(-1i*phi_layer));

                M = [F_S*sin(A)^2       + F_P*cos(theta_i)*cos(A)^2
F_S*-cos(A)*sin(A) + F_P*cos(A)*sin(A)*cos(theta_i);...
                    F_S*-cos(A)*sin(A) + F_P*cos(A)*sin(A)*cos(theta_i)
F_S*cos(A)^2       + F_P*cos(theta_i)*sin(A)^2;...
                    F_zP*-alpha
F_zP*-beta];

                % Obliquity factor and defocus
                O=( (1-NA_im^2*magn^2*(x^2+y^2) )/ (1-
NA_im^2*(x^2+y^2)) )^(1/4) * exp(-1i*2*pi()*defocus*gamma);
```

```
                %Final matrix and derivation of the polarization
amplitudes

                E_1 = M * [(theta_pol(1));(theta_pol(2))] * O ;
                E_2 = M * [(theta_pol(3));(theta_pol(4))] * O ;
                E_3 = M * [(theta_pol(5));(theta_pol(6))] * O ;
                E_4 = M * [(theta_pol(7));(theta_pol(8))] * O ;
                E_5 = M * [(theta_pol(9));(theta_pol(10))]* O ;

                for k=1:3;
                    P1(m,n,k) = E_1(k);
                    P2(m,n,k) = E_2(k);
                    P3(m,n,k) = E_3(k);
                    P4(m,n,k) = E_4(k);
                    P5(m,n,k) = E_5(k);
                end

                P0(m,n) = O;
            end
        end
        if round(m/N*100)>=flag_txt+25;
disp(strcat(num2str(round(m/N*100)), '% /',datestr(now)));
flag_txt=round(m/N*100);end
    end

    for j=1:3;                  % For each polarizations
        E1(:,:,j) = ifft2(ifftshift(M1.*P1(:,:,j)));
        E2(:,:,j) = ifft2(ifftshift(M2.*P2(:,:,j)));
        E3(:,:,j) = ifft2(ifftshift(M3.*P3(:,:,j)));
        E4(:,:,j) = ifft2(ifftshift(M4.*P4(:,:,j)));
        Etotal(:,:,j) =
ifft2(ifftshift(M1.*P1(:,:,j)+M2.*P2(:,:,j)+M3.*P3(:,:,j)+M4.*P4(:,:,j)
));                          % Calculate the total field Etotal
        disp(strcat(num2str(round(i/3*100)), '% /',datestr(now))); %
Display updated status
    end

    disp('# Calculating I'); tic
    I1 = 0.5* real(Etotal(:,:,1).*conj(Etotal(:,:,1)))...
        + 0.5* real(Etotal(:,:,2).*conj(Etotal(:,:,2)))...
        + 0.5* real(Etotal(:,:,3).*conj(Etotal(:,:,3)));
    I1 = rot90(I1,2);

    toc

    I(:,:,i)=I1;
end

%% Applying intensity threshold
I_final = [];
format long;
norm_thresh = 0.4;          % Normalized intensity threshold
thresh =
norm_thresh*max(max(max(I(1:2*N_pitch,1:2*N_pitch,1:layer_number))))
```

```
disp(strcat('Filling Factor = ',
num2str(sum(sum(sum(I>thresh)))/(N*N*size(range_depth,2))*100),'%'))
for i=1:size(I,3);              % Selecting points only above threshold
    I_final = cat(3, I_final, I(:,:,i)>thresh);
end

%% Display Structure
figure
bound = 2;                      % Number of periods to display
range_image_row = (N+1)/2+1-
round((bound+0.5)*N_pitch*sqrt(3)/2):(N+1)/2+round((bound+0.5)*N_pitch*
sqrt(3)/2);
range_image_col = (N+1)/2+1-
round(bound*N_pitch):(N+1)/2+round(bound*N_pitch);
isosurface(image_axis(range_image_row)*1e6,image_axis(range_image_col)*
1e6,(range_depth)*1e6,I(range_image_col,range_image_row,:),thresh);
isocaps
(image_axis(range_image_row)*1e6,image_axis(range_image_col)*1e6,(range
_depth)*1e6,I(range_image_col,range_image_row,:),thresh,'above');
axis equal
colorbar
xlabel('x (\mum)');ylabel('y (\mum)');zlabel('z (\mum)')
set(gca,'ZDir','reverse')
viewAngEl = 17;
viewAngRot = 55;
view(viewAngRot, viewAngEl)
load blue_colormap a
colormap(a)
axis on;
set (gcf,'Color',[1 1 1])
end
```

APPENDIX B. MATLAB SCRIPTS: BICONTINUITY ANALYSIS

This appendix contains the MATLAB script for determining the bicontinuity range in MBI structures. This is done by checking if every point in a unit cell is adjacent to a point of the same material. The MATLAB scripts to calculate the surface areas and volumes for the MBI structures are provided as well, along with the script to estimate the correction factor for the surface areas. The unit cells of the sphere-at-each-lattice-site structures can be applied to the above mentioned scripts, and is also described below.

B.1 Bicontinuity Check

```
% Determines the upper and lower limits of bicontinuity
% check_biconti_rhomb.m
% Uses fast_bicont_mbil.m
low = .4;
high = .9;
while high - low >= .01
    mid = low + (high - low) / 2;
    bi = fast_bicont_mbil(mid, N_pitch, layer_number, I, range_depth,
N);
    if bi
        low = mid
    else
        high = mid
    end
end

low = .0001;
high = .5;
while high - low >= .01
    mid = low + (high - low) / 2;
    bi = fast_bicont_mbil(mid, N_pitch, layer_number, I, range_depth,
N);
    if bi
        high = mid
    else
        low = mid
    end
end

%% Function called by check_biconti_rhomb.m
function bicontinuous = fast_bicont_mbil(perc, N_pitch, layer_number,
I, range_depth, N)
```

```
I_final = [];

thresh = perc*max(max(max(I(1:2*N_pitch,1:2*N_pitch,1:layer_number))))
for i=1:size(I,3);
    I_final = cat(3, I_final, I(:,:,i)>thresh);
end

y_start = round(N/2);
y_end = round(N/2 + 2*N_pitch);
x_start = round(N/2);
x_end = round(N/2 - 2*N_pitch);     % For DC structures
                                    % *(sqrt(3)/2)) for rhombohedral
                                    structures;
I_rect = [];
rows_count = x_end:x_start;
hex_depth = (range_depth <= 1.2E-6); % Specify height of unit cell
rhomb_layer = nnz(hex_depth) +1

for zz = 1:rhomb_layer
  for ii = 1:size(rows_count,2)
        I_rect(ii,:,zz) = I_final(rows_count(ii), y_start:y_end,zz);
        I_final(rows_count(ii), y_start:y_end,zz) = -1;
  end
end

UC = I_rect;            % Initializing unit cell
UC_temp = I_rect;
DL1 = [0 0 0];          % Lists containing all bicontinuous pixels
DL2 = [0 0 0];          % Done lists initialized as empty
matA = 1;               % Initializing material A as 1
matB = not(matA);       % Initialing material B with complement of A
[r,c,v] = ind2sub(size(UC),find(UC == matB));
if r
    WL1 = [r(1), c(1), v(1)]; % Temporary waitlist to store pixels that
are being checked for bicontinuity
else
    WL1 = [];
    DL1 = [1,1,1];
end
UC_temp(WL1(1),WL1(2), WL1(3)) = -1 ;
while not(isempty(WL1)) % Run loop until WL is empty
    pixcoor = WL1(1,:);
    for i = 1:3
        for j = [-1 1]
            neighcoor = pixcoor;
            neighcoor(i) = neighcoor(i) + j;
            if neighcoor(1) >= 1 && neighcoor(1) <= size(UC,1) &&
neighcoor(2) >= 1 && neighcoor(2) <= size(UC,2) && neighcoor(3) >= 1 &&
neighcoor(3) <= size(UC,3)
                if UC(neighcoor(1),neighcoor(2),neighcoor(3)) >= matA
% Check if neighbor material is same   % if material is B, then == matB
                    if not(sum(ismember(neighcoor, WL1, 'rows'))) &&
not(sum(ismember(neighcoor, DL1, 'rows')))
                        neighcoor
                        WL1 = [WL1; neighcoor]; % Add neighbor to WL
```

```
                        UC_temp(neighcoor(1), neighcoor(2),
neighcoor(3)) = -1 ;
                    end
                end
            end
        end
    end

    DL1 = [DL1; WL1(1,:)]; % Store first coordinate of WL to done list
    WL1(1,:) = [];         % Remove first coordinate from WL
    size(DL1)
    size(WL1)
    disp('----------------------')
end

%%  Checking opposite faces for bicontinuity
sum_face_x = UC(1,:,:) + UC(size(UC,1), :, :);
sum_face_y = UC(:,1,:) + UC(:, size(UC,2), :);
sum_face_z = UC(:,:,1) + UC(:, :, size(UC,3));
testAx = find(sum_face_x >= 2*matA);
testBx = find(sum_face_x == 2*matB);
testAy = find(sum_face_y >= 2*matA);
testBy = find(sum_face_y == 2*matB);
testAz = find(sum_face_z >= 2*matA);
testBz = find(sum_face_z == 2*matB);
check_face = isempty(testAx) + isempty(testAy) + isempty(testAz) +
isempty(testBx) + isempty(testBy) + isempty(testBz);

DL1(1,:,:) = [];          % Remove first coordinate of done lists
DL2(1,:,:) = [];
no_of_ones = nnz(UC == 1);
no_of_zeros = numel(UC) - nnz(UC);
if no_of_ones == size(DL1,1) && check_face == 0
%   if no_of_zeros == size(DL1,1) ; when checking for material B
    disp('yes, structure is bicontinuous');
    bicontinuous = true;
else
    disp('no, structure is not bicontinuous');
    bicontinuous = false;
end

end
```

B.2 Surface Areas and Volume Fractions Calculation

```
%% bicont_mbil_driver.m
% Uses surf_bicont_mbil.m

% Volume fraction calculation
perc = 0:0.001:1;
for i = 1:size(perc,2);
    thresh(i) =
perc(i)*max(max(max(I(1:2*N_pitch,1:2*N_pitch,1:layer_number))));
```

```
    ffactor(i) =
(sum(sum(sum(I<thresh(i))))/(N*N*size(range_depth,2)));
end
line(perc, ffactor,'Color', 'b','LineWidth',4);

% Surface area calculation
normthresh = 0:.05:1;
num = size(normthresh);

surfareas = ones(num);

tic
for i=1:num(2)
    surfareas(i) = surf_bicont_mbil(normthresh(i), N_pitch,
layer_number, I, range_depth, N);
i
end
toc
plot(normthresh,surfareas_inpr_fc);


%% Function called by bicont_mbil_driver.m
function sa = surf_bicont_mbil(perc, N_pitch, layer_number, I,
range_depth, N)

I_final = [];

thresh = perc*max(max(max(I(1:2*N_pitch,1:2*N_pitch,1:layer_number))))
disp(strcat('Filling Factor =
',num2str(sum(sum(sum(I>thresh)))/(N*N*size(range_depth,2))*100),'%'))
for i=1:size(I,3);
    I_final = cat(3, I_final, I(:,:,i)>thresh);
end

y_start = round(N/2);
y_end = round((N/2) + N_pitch);
x_start = round(N/2);
x_end = round(N/2 - N_pitch*(sqrt(3)/2));

I_rect = [];
rows_count = x_end:x_start;
hex_depth = (range_depth<=1.67E-6);
rhomb_layer = nnz(hex_depth) +1;

for zz = 1:rhomb_layer
  for ii = 1:size(rows_count,2)
        I_rect(ii,:,zz) = I_final(rows_count(ii), y_start:y_end,zz);
%  I_final(rows_count(ii), y_start:y_end,zz) = -1;
  end
end

UC_bin = I_rect;
matA = 1;
matB = not(matA);
[r,c,v] = ind2sub(size(UC_bin),find(UC_bin == matB));
```

```
count = 0;
zerolist = [];
onelist = [];
for i = 1:size(r,1)
    zerolist = [zerolist ; [r(i),c(i),v(i)]];
    for j = [-1,1]
        temp1 = [r(i)+j,c(i),v(i)];
        temp2 = [r(i),c(i)+j,v(i)];
        temp3 = [r(i),c(i),v(i)+j];
        p = r(i)+j; q = c(i)+j;
        if r(i) == 1 || r(i) == size(UC_bin,1) %|| c(i) == 1 || c(i) ==
dim
            %                           continue; % For simple cases
            if p ~= 0 && p < size(UC_bin,1)
                if UC_bin(p,c(i),v(i)) == 1
                    count = count+1;
                    UC_bin(p,c(i),v(i)) = -1;
                    onelist = [onelist; [p,c(i),v(i)] ];
                    continue;
                else
                    continue;
                end
            elseif q ~= 0 && q < size(UC_bin,2)
                if UC_bin(r(i),q,v(i)) == 1
                    count = count+1;
                    UC_bin(r(i),q,v(i)) = -1;
                    onelist = [onelist; [r(i),q,v(i)] ];
                    continue;
                else
                    continue;
                end

            else
                continue;
            end
        end

    if c(i) == 1 || c(i) == size(UC_bin,2)
        if q ~= 0 && q < size(UC_bin,2)
            if UC_bin(r(i),q,v(i)) == 1
                count = count+1;
                UC_bin(r(i),q,v(i)) = -1;
                onelist = [onelist; [r(i),q,v(i)] ];
                continue;
            else
                continue;
            end
        elseif p ~= 0 && p < size(UC_bin,1)
            if UC_bin(p,c(i),v(i)) == 1
                count = count+1;
                UC_bin(p,c(i),v(i)) = -1;
                onelist = [onelist; [p,c(i),v(i)]

 ];
                continue;
            else
```

```
                continue;
            end
        else
            continue;
        end
    end
    if UC_bin(p,c(i),v(i)) == 1
        count = count+1;
        UC_bin(p,c(i),v(i)) = -1;
        onelist = [onelist; [p,c(i),v(i)] ];
    end
        if UC_bin(r(i),q,v(i)) == 1
            count = count+1;
            UC_bin(r(i),q,v(i)) = -1;
            onelist = [onelist; [r(i),q,v(i)] ];
        end
        if UC_bin(p,q,v(i)) == 1
            count = count+1;
            UC_bin(p,q,v(i)) = -1;
            onelist = [onelist; [p,q,v(i)] ];
        end
        if UC_bin(p,c(i)-j,v(i)) == 1
            count = count+1;
            UC_bin(p,c(i)-j,v(i)) = -1;
            onelist = [onelist; [p,c(i)-j,v(i)] ];
        end
    end
 % count
end

sa = count/((size(I_rect,1)*size(I_rect,2)*size(I_rect,3))^(2/3))

end
```

B.3 Surface Areas Correction Factor Calculation

```
%% correction_factor.m

N = 51;       % Number of cubes representing the radius of the sphere
edge = 0.2 ;  % Edge length of the cube
res = floor((N*2/edge)) +1;
[X,Y,Z] = meshgrid (linspace(-N,N,res),linspace(-N,N,res),linspace(-
N,N,res));
rad = (N-0.5)*edge   % Radius of the sphere
block1 = zeros(res,res,res);
block2 = zeros(res,res,res);
block1 = block1 + ((X).^2)+((Y).^2)+((Z).^2) <= (rad)^2; % Retain
points <= radius only (sphere)

onelist = [];
[r,c,v] = ind2sub(size(block1),find(block1 == 1));
for i = 1:size(r,1)
```

```
    uef = block1(r(i)+1, c(i), v(i)) + block1(r(i)-1, c(i), v(i)) +
block1(r(i), c(i)+1, v(i)) + block1(r(i), c(i)-1, v(i)) + block1(r(i),
c(i), v(i)+1) + block1(r(i), c(i), v(i)-1);
    if uef < 6
        block2(r(i),c(i),v(i)) = 1;    % Retain points only at the
surface
    end
end
block = block2;

dim = floor(res/2) +1;
octant = zeros(dim,dim,dim);
octant = block(1:dim,1:dim,1:dim);

count = 0;
ef_area = 0;
onelist = [];
[r,c,v] = ind2sub(size(octant),find(octant == 1));

for i = 1:size(r,1)
    onelist = [onelist ; [r(i),c(i),v(i)]];
    uef = 0;
    uef = block(r(i)+1, c(i), v(i)) + block(r(i)-1, c(i), v(i)) +
block(r(i), c(i)+1, v(i)) + block(r(i), c(i)-1, v(i)) + block(r(i),
c(i), v(i)+1) + block(r(i), c(i), v(i)-1);
    if uef == 6
        octant(r(i),c(i),v(i)) = -61;
        continue;
    elseif uef == 5
        if block(r(i), c(i), v(i)-1) == 1
            octant(r(i),c(i),v(i)) = -51;
            continue;
        else
            ef_area = ef_area + (edge^2);
            count = count + 1;
            octant(r(i),c(i),v(i)) = 51;
            continue;
        end
    elseif uef == 4
        if (block(r(i)-1, c(i), v(i)) == 0 && block(r(i), c(i)-1, v(i))
== 0) || (block(r(i)-1, c(i), v(i)) == 0 && block(r(i), c(i), v(i)-1)
== 0) || (block(r(i), c(i)-1, v(i)) == 0 && block(r(i), c(i), v(i)-1)
== 0)
            ef_area = ef_area + 2*(edge^2);
            count = count + 2;
            octant(r(i),c(i),v(i)) = 42;
            continue;
        elseif block(r(i), c(i), v(i)-1) == 0
            ef_area = ef_area + (edge^2);
            count = count + 1;
            octant(r(i),c(i),v(i)) = 41;
            continue;
        elseif block(r(i)-1, c(i), v(i)) == 1 && block(r(i), c(i)-1,
v(i)) == 1 && block(r(i), c(i), v(i)-1) == 1
            octant(r(i),c(i),v(i)) = -41;
            continue;
```

```
        else
            ef_area = ef_area + (edge^2);
            count = count + 1;
            octant(r(i),c(i),v(i)) = 441;
            continue;
        end
    elseif uef == 3
        if block(r(i)-1, c(i), v(i)) == 1 && block(r(i), c(i)-1, v(i))
== 1 && block(r(i), c(i), v(i)-1) == 1
            octant(r(i),c(i),v(i)) = -31;
            continue;
        elseif block(r(i)-1, c(i), v(i)) == 1 && block(r(i), c(i)-1,
v(i)) && block(r(i), c(i), v(i)-1) == 0
            ef_area = ef_area + (edge^2);
            count = count + 1;
            octant(r(i),c(i),v(i)) = 31;
            continue;
        elseif block(r(i)+1, c(i), v(i)) == 1 && block(r(i), c(i)+1,
v(i)) == 1 && block(r(i), c(i), v(i)+1) == 1
            ef_area = ef_area + 3*(edge^2);
            count = count + 3;
            octant(r(i),c(i),v(i)) = 33;
            continue;
        else
            ef_area = ef_area + 2*(edge^2);
            count = count + 2;
            octant(r(i),c(i),v(i)) = 32;
            continue;
        end
    elseif uef == 2
        if (block(r(i)+1, c(i), v(i)) == 1 && block(r(i), c(i)+1, v(i))
== 1) || (block(r(i)+1, c(i), v(i)) == 1 && block(r(i), c(i), v(i)+1)
== 1) || (block(r(i), c(i)+1, v(i)) == 1 && block(r(i), c(i), v(i)+1)
== 1)
            ef_area = ef_area + 3*(edge^2);
            count = count + 3;
            octant(r(i),c(i),v(i)) = 23;
            continue;
        elseif block(r(i)-1, c(i), v(i)) == 1 && block(r(i), c(i)-1,
v(i)) == 1
            octant(r(i),c(i),v(i)) = -21;
            continue;
        else
            ef_area = ef_area + 2*(edge^2);
            count = count + 2;
            octant(r(i),c(i),v(i)) = 22;
            continue;
        end
    elseif uef == 1
        if (block(r(i)-1,c(i),v(i)) == 1) || (block(r(i),c(i)-1,v(i))
== 1) || (block(r(i),c(i),v(i)-1) == 1)
            ef_area = ef_area + 2*(edge^2);
            count = count + 2;
            octant(r(i),c(i),v(i)) = 12;
            continue;
        elseif (block(r(i)+1,c(i),v(i)) == 1) ||
(block(r(i),c(i)+1,v(i)) == 1) || (block(r(i),c(i),v(i)+1) == 1)
```

```
            ef_area = ef_area + 3*(edge^2);
            count = count + 3;
            octant(r(i),c(i),v(i)) = 13;
            continue;
        end
    elseif uef == 0
        if (block(r(i)-1,c(i)+1,v(i)) == 1) && (block(r(i)+1,c(i)-
1,v(i)) == 1)
            ef_area = ef_area + 3*(edge^2);
            count = count + 3;
            octant(r(i),c(i),v(i)) = 03;
            continue;
        else
            ef_area = ef_area + 5*(edge^2);
            count = count + 5;
            octant(r(i),c(i),v(i)) = 05;
            continue;
        end

    end
end

area_of_cubes = ef_area
octant_area = 4*pi*rad*rad/8
correctionfactor = ef_area/octant_area
```

B.4 Generating Sphere-at-Each-Lattice-Site Structures

```
dim = 201;               % Setting the resolution
[X,Y,Z] = meshgrid
(linspace(0,1,dim),linspace(0,1,dim),linspace(0,1,dim)); % (x,y,z)
space, normalized from 0 to 1
R = 0.4                  % Radius of the spheres
UC = zeros(dim,dim,dim); % UC is the Unit Cell matrix, initialized with
0s

%% Position of the spheres in space for a given cubic lattice
s = importdata('data/ BCC-spheres');

%% Computation
for ii = 1:length(s) % For each sphere position
    % Note that ((X-s(ii,1)).^2+(Y-s(ii,2)).^2+(Z-s(ii,3)).^2 <= R^2)
gives logical values, but by summing it with integer (UC +), the
logical 0 and 1s become integers
    UC = UC + ((X-s(ii,1)).^2+(Y-s(ii,2)).^2+(Z-s(ii,3)).^2 <= R^2);
% Overlapping spheres will appear as integers > 1
end

% 3D visualization
figure;
isosurface(linspace(0,1,dim),linspace(0,1,dim),linspace(0,1,dim),UC,0.9
9);
```

```
isocaps(linspace(0,1,dim),linspace(0,1,dim),linspace(0,1,dim),UC,0.99,'
above');
axis equal
title(strcat('Sphere radius = ',num2str(R),'a_h'))
xlabel('x-axis')
ylabel('y-axis')
zlabel('z-axis')
axis on
set (gcf,'Color',[1 1 1])
```

REFERENCES

[1] M. Maldovan and E. L. Thomas, *Periodic Materials and Interference Lithography for Photonics, Phononics and Mechanics*. Weinheim, Germany: Wiley-VCH, 2009.

[2] C. O. Cho, J. Jeong, J. Lee, H. Jeon, I. Kim, J. D. H., Y. S. Park, and J. C. Woo, "Photonic crystal band edge laser array with a holographically generated square-lattice pattern," *Appl. Phys. Lett.,* vol. 87, pp. 161102-1-161102-3, Oct. 10, 2005.

[3] Q.-Y. Lu, W. Zhang, L.-J. Wang, J.-Q. Liu, L. Li, F.-Q. Liu, and Z.-G. Wang, "Holographic fabricated photonic-crystal distributed-feedback quantum cascade laser with near-diffraction-limited beam quality," *Opt. Express,* vol. 17, pp. 18900-18905, Oct. 12, 2009.

[4] G. Q. Liang, W. D. Mao, Y. Y. Pu, H. Zou, H. Z. Wang, and Z. H. Zeng, "Fabrication of two-dimensional coupled photonic crystal resonator arrays by holographic lithography," *Appl. Phys. Lett.,* vol. 89, pp. 173304-1-173304-3, Jul. 24, 2006.

[5] M. A. Mansouri-Birjandi, M. K. Moravvej-Farshi, and A. Rostami, "Ultrafast low-threshold all-optical switch implemented by arrays of ring resonators coupled to a Mach-Zehnder interferometer arm: based on 2D photonic crystals," *Appl. Opt.,* vol. 47, pp. 5041-5050, Sept. 19, 2008.

[6] X. Serey, S. Mandal, and D. Erickson, "Comparison of silicon photonic crystal resonator designs for optical trapping of nanomaterials," *Nanotechnology,* vol. 21, p. 305202 (8 pp.), 2010.

[7] A. Jafarpour, E. Chow, C. M. Reinke, J. Huang, A. Adibi, A. Grot, L. W. Mirkarimi, G. Girolami, R. K. Lee, and Y. Xu, "Large-bandwidth ultra-low-loss guiding in bi-periodic photonic crystal waveguides," *Appl. Phys. B,* vol. 79, pp. 409-414, 2004.

[8] M. C. R. Leibovici and T. K. Gaylord, "Photonic-crystal waveguide structure by pattern-integrated interference lithography," *Opt. Lett.,* vol. 40, pp. 2806-2809, Jun. 15, 2015.

[9] T. Zijlstra, E. Van Der Drift, M. J. A. De Dood, E. Snoeks, and A. Polman, "Fabrication of two-dimensional photonic crystal waveguides for 1.5 um in silicon by deep anisotropic dry etching," *J. Vac. Sci. Technol. B,* vol. 17, pp. 2734-2739, Nov./Dec., 1999.

[10] V. Lousse, S. Jonghwa, and F. Shanhui, "Conditions for designing single-mode air-core waveguides in three-dimensional photonic crystals," *Appl. Phys. Lett.,* vol. 89, pp. 161103-1-161103-3, 2006.

[11] M. Tokushima, J. Ushida, A. Gomyo, M. Shirane, and H. Yamada, "Efficient transmission mechanisms for waveguides with 90° bends in pillar photonic crystals," *J. Opt. Soc. Am. B,* vol. 22, pp. 2472-2479, Nov. 2005.

[12] R. S. Daveau, K. C. Balram, T. Pregnolato, J. Liu, E. H. Lee, J. D. Song, V. Verma, R. Mirin, S. W. Nam, L. Midolo, S. Stobbe, K. Srinivasan, and P. Lodahl, "Efficient fiber-coupled single-photon source based on quantum dots in a photonic-crystal waveguide," *Optica,* vol. 4, pp. 178-184, 2017.

[13] Q. Zhu and B. Li, "Photonic crystal waveguide-based Mach-Zehnder demultiplexer," *Appl. Opt.,* vol. 45, pp. 8870-8873, Dec. 10, 2006.

[14] X. H. Sun, X. M. Tao, T. Ye, X. P., and S. Y., "2D and 3D electrically switchable hexagonal photonic crystal in the ultraviolet range," *Appl. Phys. B,* vol. 87, pp. 267-271, 2007.

[15] X. H. Sun, X. M. Tao, and Y. Y. Wang, "Fabrication of electrically switchable photonic crystals with different structures by using a top-cut hexagon prism," *Proc. SPIE,* vol. 7267, pp. 72670V-1-72670V-10, Jan. 1, 2008.

[16] X. H. Sun and X. M. Tao, "Switchable photonic crystal for polymer dispersed liquid crystal," *Opt. Laser Technol.,* vol. 43, pp. 820-824, 2011.

[17] J. Lutkenhaus, D. George, D. Garrett, H. L. Zhang, and Y. K. Lin, "Holographic formation of compound photonic crystal and nano-antenna templates through laser interference," *J. Appl. Phys.,* vol. 113, p. 103103, Mar. 2013.

[18] S. Zheng, Y. Zhu, and S. Krishnaswamy, "Fiber humidity sensors with high sensitivity and selectivity based on interior nanofilm-coated photonic crystal fiber long-period gratings," *Sensor. Actuat. B-Chem.,* vol. 176, pp. 264-274, 2013.

[19] C. P. Tsangarides, A. K. Yetisen, F. da Cruz Vasconcellos, Y. Montelongo, M. M. Qasim, T. D. Wilkinson, C. R. Lowe, and H. Butt, "Computational modelling and characterisation of nanoparticle-based tuneable photonic crystal sensors," *RSC Advances,* vol. 4, pp. 10454-10461, 2014.

[20] F. Monifi, A. Ghaffari, M. Djavid, and M. S. Abrishamian, "Three output port channel-drop filter based on photonic crystals," *Appl. Opt.,* vol. 48, pp. 804-809, Jan. 26, 2009.

[21] T. P. White, L. C. Botten, R. C. McPhedran, and C. Martijn de Sterke, "Ultracompact resonant filters in photonic crystals," *Opt. Lett.,* vol. 28, pp. 2452-4-2452-6, 2003.

[22] B. Hu, M. Lu, W. Li, K. Zou, Z. Zhou, A. Lin, and N. Li, "High birefringent rhombic-hole photonic crystal fibers," *Appl. Opt.,* vol. 49, pp. 6098-6101, Nov. 1, 2010.

[23] J. N. Dash and R. Jha, "Graphene-based birefringent photonic crystal fiber sensor using surface plasmon resonance," *IEEE Photonics Technol. Lett.,* vol. 26, pp. 1092-1095, Jun. 1, 2014.

[24] M. A. Finger, T. S. Iskhakov, N. Y. Joly, M. V. Chekhova, and P. S. J. Russell, "Raman-free, noble-gas-filled photonic-crystal fiber source for ultrafast, very bright twin-beam squeezed vacuum," *Phys. Rev. Lett.,* vol. 115, p. 143602, Sep. 30, 2015.

[25] Y.-H. Lin, C.-Y. Yang, J.-H. Liou, C.-P. Yu, and G.-R. Lin, "Using graphene nano-particle embedded in photonic crystal fiber for evanescent wave mode-locking of fiber laser," *Opt. Express,* vol. 21, pp. 16763-16776, Jul. 15, 2013.

[26] C. A. Foell, A. M. Zagoskin, and J. F. Young, "Engineering silicon-based photonic crystal cavities for NV-center quantum information processing," *Opt. Spectrosc.*, vol. 108, pp. 225-229, 2010.

[27] A. Majumdar, A. Faraon, and J. Vuckovic, "Engineering anti-bunching via photon blockade in photonic crystal cavity-quantum dot systems," in *Conf. Lasers Electro-Opt./Conf. Quantum Electron. Laser Sci. (CLEO/QELS)*, Baltimore, MD, 2009, pp. 1-2.

[28] T. Fu, Z.-Q. Yang, and Z.-B. Ouyang, "Design and experimental demonstration of cherenkov radiation source based on metallic photonic crystal slow wave structure," *J. Infrared Millim. Te.,* vol. 37, pp. 1061-1068, Nov. 1, 2016.

[29] K. Fang, M. H. Matheny, X. Luan, and O. Painter, "Optical transduction and routing of microwave phonons in cavity-optomechanical circuits," *Nat. Photonics*, vol. 10, pp. 489-496, Jul. 2016.

[30] S. C. Buswell, V. A. Wright, J. M. Buriak, V. Van, and S. Evoy, "Specific detection of proteins using photonic crystal waveguides," *Opt. Express,* vol. 16, pp. 15949-15957, Sep. 29, 2008.

[31] J. Garcia-Ruperez, V. Toccafondo, M. J. Banuls, J. G. Castello, A. Griol, S. Peransi-Llopis, and A. Maquieira, "Label-free antibody detection using band edge fringes in SOI planar photonic crystal waveguides in the slow-light regime," *Opt. Express*, vol. 18, pp. 24276-24286, Nov. 8, 2010.

[32] C. Kang, C. T. Phare, Y. A. Vlasov, S. Assefa, and S. M. Weiss, "Photonic crystal slab sensor with enhanced surface area," *Opt. Express,* vol. 18, pp. 27930-27937, Dec. 20, 2010.

[33] P.-Y. Collart-Dutilleul, E. Secret, I. Panayotov, D. Deville de Périère, R. J. Martín-Palma, V. Torres-Costa, M. Martin, C. Gergely, J.-O. Durand, F. Cunin, and F. J. Cuisinier, "Adhesion and proliferation of human mesenchymal stem cells from dental pulp on porous silicon scaffolds," *ACS Appl. Mater. Inter.*, vol. 6, pp. 1719-1728, Feb. 12, 2014.

[34] W. Liu, L. Shang, F. Zheng, J. Lu, J. Qian, Y. Zhao, and Z. Gu, "Photonic crystal encoded microcarriers for biomaterial evaluation," *Small,* vol. 10, pp. 88-93, 2014.

[35] K. I. Hartmann, A. Nieto, E. C. Wu, W. R. Freeman, J. S. Kim, J. Chhablani, M. J. Sailor, and L. Cheng, "Hydrosilylated porous silicon particles function as an intravitreal drug delivery system for Daunorubicin," *J. Ocul. Pharmacol. Th.,* vol. 29, pp. 493-500, Jun. 1, 2013.

[36] M. Sharma, G. I. N. Waterhouse, S. W. C. Loader, S. Garg, and D. Svirskis, "High surface area polypyrrole scaffolds for tunable drug delivery," *Inter. J. Pharm.,* vol. 443, pp. 163-168, Feb. 25, 2013.

[37] W. Chen, K. D. Long, H. Yu, Y. Tan, J. S. Choi, B. A. Harley, and B. T. Cunningham, "Enhanced live cell imaging via photonic crystal enhanced fluorescence microscopy," *Analyst,* vol. 139, pp. 5954-5963, Nov. 2014.

[38] J.-r. Choi, H. Song, J. H. Sung, D. Kim, and K. Kim, "Microfluidic assay-based optical measurement techniques for cell analysis: A review of recent progress," *Biosens. Bioelectron.,* vol. 77, pp. 227-236, Mar. 15, 2016.

[39] Y. Tan, T. Tang, H. Xu, C. Zhu, and B. T. Cunningham, "High sensitivity automated multiplexed immunoassays using photonic crystal enhanced fluorescence microfluidic system," *Biosens. Bioelectron.,* vol. 73, pp. 32-40, Nov. 15, 2015.

[40] P. Tabeling, "Recent progress in the physics of microfluidics and related biotechnological applications," *Curr. Opin. Biotech.,* vol. 25, pp. 129-134, Feb. 2014.

[41] B. le Feber, N. Rotenberg, D. M. Beggs, and L. Kuipers, "Simultaneous measurement of nanoscale electric and magnetic optical fields," *Nat. Photonics,* vol. 8, pp. 43-46, Jan. 2014.

[42] C. K. Ullal, M. Maldovan, M. Wohlgemuth, E. L. Thomas, C. A. White, and S. Yang, "Triply periodic bicontinuous structures through interference lithography: a level-set approach," *J. Opt. Soc. Am. A,* vol. 20, pp. 948-954, May 1, 2003.

[43] S. Sattayasamitsathit, A. M. O'Mahony, X. Xiao, S. M. Brozik, C. M. Washburn, D. R. Wheeler, W. Gao, S. Minteer, J. Cha, D. B. Burckel, R. Polsky, and J. Wang, "Highly ordered tailored three-dimensional hierarchical nano/microporous gold-carbon architectures," *J. Mater. Chem.,* vol. 22, pp. 11950-11956, Apr. 18, 2012.

[44] H. Zhang and P. V. Braun, "Three-dimensional metal scaffold supported bicontinuous silicon battery anodes," *Nano Lett.,* vol. 12, pp. 2778-2783, Jun. 13, 2012.

[45] M. J. Lawrence and G. D. Rees, "Microemulsion-based media as novel drug delivery systems," *Adv. Drug Deliver. Rev.,* vol. 64, pp. 175-193, Dec. 2012.

[46] S. A. Chime, F. C. Kenechukwu, and A. A. Attama, *Nanoemulsions — Advances in Formulation, Characterization and Applications in Drug Delivery*. Rijeka: InTech, 2014.

[47] T. Gitli and M. S. Silverstein, "Emulsion templated bicontinuous hydrophobic-hydrophilic polymers: Loading and release," *Polymer*, vol. 52, pp. 107-115, Jan. 7, 2011.

[48] E. Jo, M.-C. Lim, H.-N. Kim, H.-J. Paik, Y.-R. Kim, and U. Jeong, "Microfluidic channels fabricated on mesoporous electrospun fiber mats: A facile route to microfluidic chips," *J. Polym. Sci. Pol. Phys.*, vol. 49, pp. 89-95, 2011.

[49] W. Lee, D.-Y. Kang, J. Song, J. H. Moon, and D. Kim, "Controlled unusual stiffness of mechanical metamaterials," *Scientific Reports*, vol. 6, p. 20312, Feb. 3, 2016.

[50] J.-H. Lee, L. Wang, M. C. Boyce, and E. L. Thomas, "Periodic bicontinuous composites for high specific energy absorption," *Nano Lett.*, vol. 12, pp. 4392-4396, Aug. 8, 2012.

[51] J.-H. Lee, J. P. Singer, and E. L. Thomas, "Micro-/nanostructured mechanical metamaterials," *Adv. Mater.*, vol. 24, pp. 4782-4810, Aug. 17, 2012.

[52] T. Bückmann, N. Stenger, M. Kadic, J. Kaschke, A. Frölich, T. Kennerknecht, C. Eberl, M. Thiel, and M. Wegener, "Tailored 3D mechanical metamaterials made by dip-in direct-laser-writing optical lithography," *Adv. Mater.*, vol. 24, pp. 2710-2714, Apr. 12, 2012.

[53] X.-Y. Zhang, G. Fang, and J. Zhou, "Additively manufactured scaffolds for bone tissue engineering and the prediction of their mechanical behavior: a review," *Materials*, vol. 10, p. 50, Jan. 10, 2017.

[54] T. Bera, C. Malcuit, R. J. Clements, and E. Hegmann, "Role of surfactant during microemulsion photopolymerization for the creation of three-dimensional liquid crystal elastomer microsphere spatial cell scaffolds," *Front. Mater.*, vol. 3, Jun. 30, 2016.

[55] M. Martina, G. Subramanyam, J. C. Weaver, D. W. Hutmacher, D. E. Morse, and S. Valiyaveettil, "Developing macroporous bicontinuous materials as scaffolds for tissue engineering," *Biomaterials*, vol. 26, pp. 5609-5616, Oct. 2005.

[56] J. H. Jang, C. K. Ullal, M. Maldovan, T. Gorishnyy, S. Kooi, C. Y. Koh, and E. L. Thomas, "3D micro- and nanostructures via interference lithography," *Adv. Funct. Mater.*, vol. 17, pp. 3027-3041, Nov. 5, 2007.

[57] A. M. Urbas, M. Maldovan, P. DeRege, and E. L. Thomas, "Bicontinuous cubic block copolymer photonic crystals," *Adv. Mater.*, vol. 14, pp. 1850-1853, Sep. 26, 2002.

[58] Y. Lin, Y. Tang, H. Ma, J. Yang, Y. Tian, W. Ma, and X. Wang, "Formation of a bicontinuous structure membrane of polyvinylidene fluoride in diphenyl carbonate diluent via thermally induced phase separation," *J. Appl. Ploym. Sci.,* vol. 114, pp. 1523-1528, Jun. 23, 2009.

[59] M. R. M. Abed, S. C. Kumbharkar, A. M. Groth, and K. Li, "Ultrafiltration PVDF hollow fibre membranes with interconnected bicontinuous structures produced via a single-step phase inversion technique," *J. Membrane Sci.,* vol. 407–408, pp. 145-154, Jul. 15, 2012.

[60] Y.-C. Chen, "Fabrication and Characterization of Three Dimensional Photonic Crystals Generated by Multibeam Interference Lithography," PhD thesis, University of Illinois at Urbana-Champaign, 2009.

[61] J. H. Pikul, H. Gang Zhang, J. Cho, P. V. Braun, and W. P. King, "High-power lithium ion microbatteries from interdigitated three-dimensional bicontinuous nanoporous electrodes," *Nat. Commun.,* vol. 4, p. 1732, Apr. 16, 2013.

[62] B. H. Jones and T. P. Lodge, "Nanocasting nanoporous inorganic and organic materials from polymeric bicontinuous microemulsion templates," *Polym. J.,* vol. 44, pp. 131-146, Feb. 2012.

[63] J. H. Moon, Y. Xu, Y. Dan, S. M. Yang, A. T. Johnson, and S. Yang, "Triply periodic bicontinuous structures as templates for photonic crystals: a pinch-off problem," *Adv. Mater.,* vol. 19, pp. 1510-1514, Apr. 30, 2007.

[64] M. Qi, E. Lidorikis, P. T. Rakich, S. G. Johnson, J. D. Joannopoulos, E. P. Ippen, and H. I. Smith, "A three-dimensional optical photonic crystal with designed point defects," *Nature,* vol. 429, pp. 538-542, Jun. 2004.

[65] W. D. Mao, Y. C. Zhong, J. W. Dong, and H. Z. Wang, "Crystallography of two-dimensional photonic lattices formed by holography of three noncoplanar beams," *J. Opt. Soc. Am. B,* vol. 22, pp. 1085-1091, May 2005.

[66] L. Z. Cai, X. L. Yang, and Y. R. Wang, "Formation of three-dimensional periodic microstructures by interference of four noncoplanar beams," *J. Opt. Soc. Am. A,* vol. 19, pp. 2238-2244, Nov. 2002.

[67] N. D. Lai, J. H. Lin, and C. C. Hsu, "Fabrication of highly rotational symmetric quasi-periodic structures by multiexposure of a three-beam interference technique," *Appl. Opt.,* vol. 46, pp. 5645-5648, Aug. 10, 2007.

[68] E. R. Dedman, D. N. Sharp, A. J. Turberfield, C. F. Blanford, and R. G. Denning, "Photonic crystals with a chiral basis by holographic lithography," *Phot. Nano. Fund. Appl.,* vol. 3, pp. 79-83, Dec. 2005.

[69] W. Y. Tam, "Icosahedral quasicrystals by optical interference holography," *Appl. Phys. Lett.,* vol. 89, p. 251111, Dec. 18, 2006.

[70] M. Kumar and J. Joseph, "Optical generation of a spatially variant two-dimensional lattice structure by using a phase only spatial light modulator," *Appl. Phys. Lett.*, vol. 105, p. 051102, Aug. 2014.

[71] M. Kumar and J. Joseph, "Digitally reconfigurable complex two-dimensional dual-lattice structure by optical phase engineering," *Appl. Opt.*, vol. 53, pp. 1333-1338, Mar. 1, 2014.

[72] M. C. R. Leibovici, "Pattern-Integrated Interference Lithography for Two-Dimensional and Three-Dimensional Periodic-Lattice-Based Microstructures," Ph.D. thesis, School of Electrical and Computer Engineering, Georgia Institute of Technology, Atlanta, Georgia, 2015.

[73] C. Moormann, J. Bolten, and H. Kurz, "Spatial phase-locked combination lithography for photonic crystal devices," *Microelectron. Eng.*, vol. 73-74, pp. 417-422, Sep. 2004.

[74] C. J. M. van Rijn, "Laser interference as a lithographic nanopatterning tool," *J. Microlithogr., Microfabr., Microsyst.*, vol. 5, p. 11012, Jan. 2006.

[75] T. Liu, M. Fallahi, J. V. Moloney, and M. Mansuripur, "Fabrication of two-dimensional photonic crystals with embedded defects using blue-laser-writer and optical holography," *IEEE Photon. Technol. Lett.*, vol. 18, pp. 1100-1102, May 1, 2006.

[76] M. Fritze, T. M. Noomstein, B. Tyrrell, and M. Rothschild, "Extending 193nm immersion with hybrid optical maskless lithography," *Solid State Technol.*, vol. 49, pp. 41-3, 2006.

[77] J. Scrimgeour, D. N. Sharp, C. F. Blanford, O. M. Roche, R. G. Denning, and A. J. Turberfield, "Three-dimensional optical lithography for photonic microstructures," *Adv. Mater.*, vol. 18, pp. 1557-1560, Jun. 2006.

[78] Y. K. Lin, A. Harb, K. Lozano, D. Xu, and K. P. Chen, "Five beam holographic lithography for simultaneous fabrication of three dimensional photonic crystal templates and line defects using phase tunable diffractive optical element," *Opt. Express*, vol. 17, pp. 16625-16631, Sep. 14, 2009.

[79] K. O. Hill, B. Malo, F. Bilodeau, D. C. Johnson, and J. Albert, "Bragg gratings fabricated in monomode photosensitive optical fiber by UV exposure through a phase mask," *Appl. Phys. Lett.*, vol. 62, pp. 1035-1037, Mar. 8, 1993.

[80] J. Lutkenhaus, D. George, D. Lowell, H. Zhang, and Y. Lin, "Design and fabrication of local fill fraction in photonic crystal templates using a spatial light modulator," *Proc. SPIE*, vol. 9759, pp. 97591M-1-97591M-11, 2016.

[81] J. Lutkenhaus, D. George, U. Philipose, H. Zhang, and Y. Lin, "Spatial light modulator based holographic fabrication of 3D spatially varying photonic crystal templates," *Proc. SPIE,* vol. 9374, pp. 93740V-1-93740V-11, Mar. 13, 2015.

[82] G. M. Burrow, M. C. R. Leibovici, and T. K. Gaylord, "Pattern-integrated interference lithography: single-exposure fabrication of photonic-crystal structures," *Appl. Opt.,* vol. 51, pp. 4028-4041, Jun. 20, 2012.

[83] M. C. R. Leibovici and T. K. Gaylord, "Custom-modified three-dimensional periodic microstructures by pattern-integrated interference lithography," *J. Opt. Soc. Am. A,* vol. 31, pp. 1515-1519, Jul. 2014.

[84] M. C. R. Leibovici and T. K. Gaylord, "Photomask design method for pattern-integrated interference lithography," *J. Micro/Nanolithogr., MEMS, MOEMS,* vol. 15, pp. 014502-1-014502-7, Mar. 2016.

[85] N. Gutman. (2014). *Spotlight on 'Custom-modified three-dimensional periodic microstructures by pattern-integrated interference lithography'*. Available: http://www.opticsinfobase.org/spotlight/summary.cfm?uri=josaa-31-7-1515

[86] H. Jinnai, Y. Nishikawa, S.-H. Chen, S. Koizumi, and T. Hashimoto, "Morphological characterization of bicontinuous structures in polymer blends and microemulsions by the inverse-clipping method in the context of the clipped-random-wave model," *Phys. Rev. E,* vol. 61, pp. 6773-6780, Jun. 2000.

[87] S. Burauer, L. Belkoura, C. Stubenrauch, and R. Strey, "Bicontinuous microemulsions revisited: a new approach to freeze fracture electron microscopy (FFEM)," *Colloid. Surface A,* vol. 228, pp. 159-170, Nov. 1, 2003.

[88] S. H. Chen, S. L. Chang, and R. Strey, "Simulation of bicontinuous microemulsions: comparison of simulated real-space microstructures with scattering experiments," *J. Appl. Crystallogr.,* vol. 24, pp. 721-731, 1991.

[89] H. Jinnai, T. Hashimoto, D. Lee, and S.-H. Chen, "Morphological characterization of bicontinuous phase-separated polymer blends and one-phase microemulsions," *Macromolecules,* vol. 30, pp. 130-136, Jan. 1, 1997.

[90] L. Wu, Y. Zhong, C. T. Chan, K. S. Wong, and G. P. Wang, "Fabrication of large area two- and three-dimensional polymer photonic crystals using single refracting prism holographic lithography," *Appl. Phys. Lett.,* vol. 86, pp. 241102-1-241102-3, Jun. 2005.

[91] L. L. Yuan and P. R. Herman, "Laser scanning holographic lithography for flexible 3D fabrication of multi-scale integrated nano-structures and optical biosensors," *Scientific Reports,* vol. 6, p. 22294, Feb. 29, 2016.

[92] D.-Y. Kang, W. Lee, D. Kim, and J. H. Moon, "Three-dimensional polymeric mechanical metamaterials fabricated by multibeam interference lithography with

the assistance of plasma etching," *Langmuir*, vol. 32, pp. 8436-8441, Aug. 23, 2016.

[93] J. Wang, Y. Wen, H. Ge, Z. Sun, Y. Zheng, Y. Song, and L. Jiang, "Simple fabrication of full color colloidal crystal films with tough mechanical strength," *Macromol. Chem. Phys.*, vol. 207, pp. 596-604, 2006.

[94] Y. Guan and A. J. Pedraza, "Synthesis and characterization of self-organized nanostructure arrays generated by laser irradiation," *Mat. Res. Soc. Symp. Proc.*, vol. 818, pp. 335-340, Apr. 2004.

[95] Y. V. Miklyaev, D. C. Meisel, A. Blanco, G. von Freymann, K. Busch, W. Koch, C. Enkrich, M. Deubel, and M. Wegener, "Three-dimensional face-centered-cubic photonic crystal templates by laser holography: fabrication, optical characterization, and band-structure calculations," *Appl. Phys. Lett.*, vol. 82, pp. 1284-1286, Feb. 24, 2003.

[96] D. Chanda, L. Abolghasemi, and P. R. Herman, "One-dimensional diffractive optical element based fabrication and spectral characterization of three-dimensional photonic crystal templates," *Opt. Express*, vol. 14, pp. 8568-8577, Sept. 18, 2006.

[97] H. K. Kang, K. H. Lee, C. C. Wong, and F. Romanato, "1D to 2D transitional structure of plasmonic crystals: fabrication and characterization," *Appl. Phys. B*, vol. 97, pp. 671-677, Oct. 6, 2009.

[98] *International Tables for Crystallography*, 5 ed. vol. A. Dordrecht Kluwer, 2002.

[99] X. L. Yang, L. Z. Cai, and Q. Liu, "Polarization optimization in the interference of four umbrellalike symmetric beams for making three-dimensional periodic microstructures," *Appl. Opt.*, vol. 41, pp. 6894-6900, Nov. 10, 2002.

[100] X. Zhu, Y. Xu, S.-C. Cheng, and S. Yang, "Fidelity of holographic lithography for fabrication of 3D SU-8 photonic structures and how to minimize distortion by optical design," *Materials Research Society Symposium Proc., Materials for Nanophotonics - Plasmonics, Metamaterials and Light Localization*, Jan. 1, 2009.

[101] O. Akhavan, M. Abdolahad, and R. Asadi, "Storage of Ag nanoparticles in pore-arrays of SU-8 matrix for antibacterial applications," *J. Phys. D*, vol. 42, pp. 135416-1-135416-7, Jun. 19, 2009.

[102] L. E. Gutierrez-Rivera and L. Cescato, "SU-8 submicrometric sieves recorded by UV interference lithography," *J. Micromech. Microeng.*, vol. 18, pp. 115003-1-115003-7, Sep. 19, 2008.

[103] A. F. Lasagni, Y. Dajun, and S. Das, "Layer-by-layer interference lithography of three-dimensional microstructures in SU-8," *Adv. Eng. Mater.*, vol. 11, pp. 408-11, May 2009.

[104] T. Kondo, S. Juodkazis, V. Mizeikis, S. Matsuo, and H. Misawa, "Fabrication of three-dimensional periodic microstructures in photoresist SU-8 by phase-controlled holographic lithography," *New J. Phys.,* vol. 8, Oct. 24, 2006.

[105] Y. K. Pang, J. C. W. Lee, C. T. Ho, and W. Y. Tam, "Realization of woodpile structure using optical interference holography," *Opt. Express*, vol. 14, pp. 9113-9119, Oct. 2, 2006.

[106] D. G. Flagello, T. Milster, and A. E. Rosenbluth, "Theory of high-NA imaging in homogeneous thin films," *J. Opt. Soc. Am. A,* vol. 13, pp. 53-64, Jan. 1996.

[107] D. C. Meisel, M. Wegener, and K. Busch, "Three-dimensional photonic crystals by holographic lithography using the umbrella configuration: symmetries and complete photonic band gaps," *Phys. Rev. B,* vol. 70, pp. 165104-1-165104-10, Oct. 2004.

[108] J. L. Stay, "Multi-Beam-Interference-Based Methodology for the Fabrication of Photonic Crystal Structures," Ph.D. thesis, Electrical and Computer Engineering, Georgia Institute of Technology, Atlanta, GA, 2009.

[109] J. H. Moon and S. Yang, "Creating three-dimensional polymeric microstructures by multi-beam interference lithography," *J. Macromol. Sci., Polym. Rev.,* vol. C45, pp. 351-373, Oct.-Dec. 2005.

[110] H. Wolfgang, H. Wolfgang, Q. Hans-Jochen, S.-F. Peter, and W. Bernhard, "Simulation and process design of gray-tone lithography for the fabrication of arbitrarily shaped surfaces," *Jpn. J. Appl. Phys.,* vol. 33, p. 6809, 1994.

[111] P. Mouroulis, F. T. Hartley, D. W. Wilson, V. E. White, A. Shori, S. Nguyen, M. Zhang, and M. Feldman, "Blazed grating fabrication through gray-scale X-ray lithography," *Opt. Express*, vol. 11, pp. 270-281, Feb. 10, 2003.

[112] H. J. Choi, J. G. Kim, and G. Barbastathis, "Fabrication of aperiodic subwavelength nanostructures by Grayscale Interference Lithography (GIL)," in *13th IEEE Int. Conf. on Nanotechnol. (IEEE-NANO)*, Beijing, China, 2013, pp. 1042-1045.

[113] K. Totsu, K. Fujishiro, S. Tanaka, and M. Esashi, "Fabrication of three-dimensional microstructure using maskless gray-scale lithography," *Sensor. Actuat. A-Phys.,* vol. 130–131, pp. 387-392, Aug. 14, 2006.

[114] R. Heming, L. C. Wittig, P. Dannberg, J. Jahns, E. B. Kley, and M. Gruber, "Efficient planar-integrated free-space optical interconnects fabricated by a combination of binary and analog lithography," *J. Lightwave Technol.,* vol. 26, pp. 2136-2141, Jul. 15, 2008.

[115] M. P. Aldred, A. E. A. Contoret, S. R. Farrar, S. M. Kelly, D. Mathieson, M. O'Neill, W. C. Tsoi, and P. Vlachos, "A full-color electroluminescent device and

patterned photoalignment using light-emitting liquid crystals," *Adv. Mater.*, vol. 17, pp. 1368-1372, May 24, 2005.

[116] R. Penterman, S. I. Klink, H. de Koning, G. Nisato, and D. J. Broer, "Single-substrate liquid-crystal displays by photo-enforced stratification," *Nature*, vol. 417, pp. 55-58, May 2, 2002.

[117] Y. Jung, H. Lee, T.-J. Park, S. Kim, and S. Kwon, "Programmable gradational micropatterning of functional materials using maskless lithography controlling absorption," *Scientific Reports*, vol. 5, p. 15629, Oct. 22, 2015.

[118] N. Brimhall, T. L. Andrew, R. V. Manthena, and R. Menon, "Breaking the far-field diffraction limit in optical nanopatterning via repeated photochemical and electrochemical transitions in photochromic molecules," *Phys. Rev. Lett.*, vol. 107, pp. 205501-1-205501-5, 2011.

[119] R. Menon and H. I. Smith, "Absorbance-modulation optical lithography," *J. Opt. Soc. Am. A*, vol. 23, pp. 2290-2294, Sep. 1, 2006.

[120] S. Tay, P. A. Blanche, R. Voorakaranam, A. V. Tunc, W. Lin, S. Rokutanda, T. Gu, D. Flores, P. Wang, G. Li, P. St Hilaire, J. Thomas, R. A. Norwood, M. Yamamoto, and N. Peyghambarian, "An updatable holographic three-dimensional display," *Nature*, vol. 451, pp. 694-698, Feb. 7, 2008.

[121] W. Jin and Y. L. Xue, "Optical fabrication of wavy lattices and photonic lattices with defects in photorefractive crystal by single step projection method," *Superlattice Microst.*, vol. 82, pp. 136-142, Jun. 1, 2015.

[122] S. Zamiri, B. Reitinger, M.-A. Rodriguez-Rivera, G. Ramos-Ortiz, P. Burgholzer, S. Bauer, and J.-L. Maldonado, "Employing 532 nm wavelength in a laser ultrasound interferometer based on photorefractive polymer composites," *Open Access Lib. J.*, vol. 2, p. 8, 2015.

[123] Y. Y. Li, W. Pang, Y. Z. Chen, Z. Q. Yu, J. Y. Zhou, and H. R. Zhang, "Defect-mediated discrete solitons in optically induced photorefractive lattices," *Phys. Rev. A*, vol. 80, pp. 043824-1-043824-6, Oct. 2009.

[124] X.-s. Wang, W.-l. She, and W.-k. Lee, "Optical spatial soliton supported by photoisomerization nonlinearity in a polymer with a background beam," *J. Opt. Soc. Am. B*, vol. 23, pp. 2127-2133, Oct. 1, 2006.

[125] D. N. Sharp, A. J. Turberfield, and R. G. Denning, "Holographic photonic crystals with diamond symmetry," *Phys. Rev. B*, vol. 68, p. 205102, Nov. 3, 2003.

[126] C. P. Mark, H. Philip, D. M. Bloom, and A. F. Harvey, "Building thick photoresist structures from the bottom up," *J. Micromech. Microeng.*, vol. 13, p. 380, Feb. 28, 2003.

[127] E. N. Leith and J. Upatnieks, "Reconstructed wavefronts and communication theory," *J. Opt. Soc. Am.,* vol. 52, pp. 1123-1130, Oct. 1962.

[128] E. N. Leith and J. Upatnieks, "Wavefront reconstruction with diffused illumination and three-dimensional objects," *J. Opt. Soc. Am.,* vol. 54, pp. 1295-1301, Nov. 1964.

[129] T. J. Suleski, B. Baggett, W. F. Delaney, C. Koehler, and E. G. Johnson, "Fabrication of high-spatial-frequency gratings through computer-generated near-field holography," *Opt. Lett.,* vol. 24, pp. 602-604, May 1, 1999.

[130] M. Nalin, J. W. Menezes, L. Cescato, E. S. Braga, H. Hernandez-Figueroa, S. J. L. Ribeiro, Y. Messaddeq, and M. S. Li, "Two-dimensional photonic crystals in antimony-based films fabricated by holography," *J. Appl. Phys.,* vol. 103, May 2008.

[131] S. S. Sarkar, H. H. Solak, J. Raabe, C. David, and J. F. van der Veen, "Fabrication of Fresnel zone plates with 25nm zone width using extreme ultraviolet holography," *Micro. Engn.,* vol. 87, pp. 854-8, 2010.

[132] T. K. Gaylord, M. C. R. Leibovici, and G. M. Burrow, "Pattern-integrated interference [Invited]," *Appl. Opt.,* vol. 52, pp. 61-72, Jan. 1, 2013.

[133] G. M. Burrow, M. C. R. Leibovici, and T. K. Gaylord, "Pattern-integrated interference lithography demonstration," in *Frontiers in Optics,* Rochester, NY, 2012, p. FW1F.4.

[134] M. C. R. Leibovici, G. M. Burrow, and T. K. Gaylord, "Pattern-integrated interference lithography: prospects for nano- and microelectronics," *Opt. Express,* vol. 20, pp. 23643-23652, Oct. 8, 2012.

[135] M. Switkes and M. Rothschild, "Resolution enhancement of 157-nm lithography by liquid immersion," *Proc. SPIE,* vol. 4691, pp. 459-465, Jul. 15, 2002.

[136] B. W. Smith, A. Bourov, H. Y. Kang, F. Cropanese, Y. F. Fan, N. Lafferty, and L. Zavyalova, "Water immersion optical lithography at 193 nm," *J. Microlithogr., Microfabr., Microsyst.,* vol. 3, pp. 44-51, Jan. 2004.

[137] D. G. Flagello, T. Milster, and A. E. Rosenbluth, "Theory of high-NA imaging in homogeneous thin films," *J. Opt. Soc. Am. A,* vol. 13, pp. 53-64, Jan. 1996.

[138] N. B. Cobb, A. Zakhor, and E. A. Miloslavsky, "Mathematical and CAD framework for proximity correction," *Proc. SPIE,* vol. 2726, pp. 208-222, Jun. 7, 1996.

[139] M. C. R. Leibovici and T. K. Gaylord, "Performance simulation of 2D photonic-crystal devices fabricated by pattern-integrated interference lithography," *Opt. Lett.,* vol. 39, pp. 3798-3801, Jul. 1, 2014.

[140] G. M. Burrow, M. C. R. Leibovici, J. W. Kummer, and T. K. Gaylord, "Pattern-integrated interference lithography instrumentation," *Rev. Sci. Instrum.,* vol. 83, p. 063707, Jul. 2, 2012.

[141] S. K. Vadivel, M. C. R. Leibovici, and T. K. Gaylord, "Alignment of multiple-off-axis-beam imaging/interference systems," *Appl. Opt.,* vol. 55, pp. 3199-3202, Apr. 20, 2016.

[142] X. L. Zhu, Y. G. Xu, and S. Yang, "Distortion of 3D SU8 photonic structures fabricated by four-beam holographic lithography with umbrella configuration," *Opt. Express,* vol. 15, pp. 16546-16560, Dec. 10, 2007.

[143] R. C. Rumpf and E. G. Johnson, "Fully three-dimensional modeling of the fabrication and behavior of photonic crystals formed by holographic lithography," *J. Opt. Soc. Am. A,* vol. 21, pp. 1703-1713, Sep. 2004.

[144] M. Miyake, Y. C. Chen, P. V. Braun, and P. Wiltzius, "Fabrication of three-dimensional photonic crystals using multibeam interference lithography and electrodeposition," *Adv. Mater.,* vol. 21, pp. 3012-3015, Aug. 7, 2009.

[145] Y. Ono, "Transmittance analysis of three-dimensional photonic crystals by the effective medium theory," *Appl. Opt.,* vol. 45, pp. 131-136, Jan. 1, 2006.

[146] H. Ito, "Chemical amplification resists for microlithography," in *Microlithography · Molecular Imprinting.* Berlin, Heidelberg: Springer, 2005, pp. 37-245.

[147] Z. Poole, D. Xu, K. P. Chen, I. Olvera, K. Ohlinger, and Y. Lin, "Holographic fabrication of three-dimensional orthorhombic and tetragonal photonic crystal templates using a diffractive optical element," *Appl. Phys. Lett.,* vol. 91, pp. 251101-1--251101-3, Dec. 17, 2007.

[148] S. Yang, M. Megens, J. Aizenberg, P. Wiltzius, P. M. Chaikin, and W. B. Russel, "Creating periodic three-dimensional structures by multibeam interference of visible laser," *Chem. Mater.,* vol. 14, pp. 2831-2833, Jul. 2002.

[149] J. H. Moon, J. Ford, and S. Yang, "Fabricating three-dimensional polymeric photonic structures by multi-beam interference lithography," *Polym. Advan. Technol.,* vol. 17, pp. 83-93, Feb. 2006.

[150] D. George, J. Lutkenhaus, D. Lowell, U. Philipose, H. Zhang, Z. Poole, K. Chen, and Y. Lin, "Fabrication of 4, 5, or 6-fold symmetric 3D photonic structures using single beam and single reflective optical element based holographic lithography," *Proc. SPIE,* vol. 9350, pp. 93501K-93501K-9, Jan. 1, 2015.

[151] J. H. Moon, A. Small, G.-R. Yi, S.-K. Lee, W.-S. Chang, D. J. Pine, and S.-M. Yang, "Patterned polymer photonic crystals using soft lithography and holographic lithography," *Synthetic Metals,* vol. 148, pp. 99-102, Jan. 3, 2005.

[152] P. M. Leufke, S. Riedel, M.-S. Lee, J. Li, H. Rohrmann, T. Eimuller, P. Leiderer, J. Boneberg, G. Schatz, and M. Albrecht, "Two different coercivity lattices in Co/Pd multilayers generated by single-pulse direct laser interference lithography," *J. Appl. Phys.*, vol. 105, pp. 113915-1-113915-6, Jun. 5, 2009.

[153] B.-Y. Choi, Y. Pak, K. S. Kim, K.-H. Lee, and G.-Y. Jung, "Simultaneous fabrication of line defects-embedded periodic lattice by topographically assisted holographic lithography," *Nanoscale Res. Lett.*, vol. 6, p. 449, Jul. 12, 2011.

[154] I. Byun and J. Kim, "Cost-effective laser interference lithography using a 405 nm AlInGaN semiconductor laser," *J. Micromech. Microeng.*, vol. 20, p. 055024 (6 pp.), 2010.

[155] T. B. Oreilly and H. I. Smith, "Photoresist characterization using double exposures with interference lithography," *J. Vac. Sci. Technol. B*, vol. 26, pp. 128-131, Jan. 4, 2008.

[156] S. Jeon, J. Park, R. Cirelli, S. Yang, C. Heitzman, P. Braun, P. Kenis, and J. Rogers, "Fabricating complex three-dimensional nanostructures with high-resolution conformable phase masks," *Proc. Nat. Acad. Sci.*, vol. 101, pp. 12428-12433, Aug. 24, 2004.

[157] Y. C. Chen, J. B. Geddes, J. T. Lee, P. V. Braun, and P. Wiltzius, "Holographically fabricated photonic crystals with large reflectance," *Appl. Phys. Lett.*, vol. 91, pp. 241103-1, 2007.

[158] P. Sung-Gyu, L. Seung-Kon, M. Jun Hyuk, and Y. Seung-Man, "Holographic fabrication of three-dimensional nanostructures for microfluidic passive mixing," *Lab on a Chip*, vol. 9, pp. 3144-50, 2009.

[159] T. Kondo, S. Juodkazis, V. Mizeikis, H. Misawa, and S. Matsuo, "Holographic lithography of periodic two- and three-dimensional microstructures in photoresist SU-8," *Opt. Express*, vol. 14, pp. 7943-7953, Aug. 21, 2006.

[160] D. E. Sedivy and T. K. Gaylord, "Modeling of multiple-optical-axis pattern-integrated interference lithography systems," *Appl. Opt.*, vol. 53, pp. D12-D18, Jun. 1, 2014.

[161] D. E. Sedivy and T. K. Gaylord, "Characterization of multiple-optical-axis implementation of pattern-integrated interference lithography," in *Frontiers in Optics*, Orlando, FL, 2013, p. FTh3F.2.